METHACRYLATED COLLAGEN AND HNT COMPOSITE HYDROGELS FOR APPLICATION IN BONE TISSUE REGENERATION

by

Yue Li, M.S.

A Dissertation Presented in Partial
Fulfillment of the Requirements of the
Degree Doctor of Philosophy

COLLEGE OF ENGINEERING AND SCIENCE
LOUISIANA TECH UNIVERSITY

November 2021

LOUISIANA TECH UNIVERSITY

GRADUATE SCHOOL

September 30, 2021
Date of dissertation defense

We hereby recommend that the dissertation prepared by

Yue Li, MS

entitled **Methacrylated Collagen and HNT Composite Hydrogels for Application in Bone Tissue Regeneration**

be accepted in partial fulfillment of the requirements for the degree of

Doctor of Philosophy in Biomedical Engineering

David K Mills

Supervisor of Dissertation Research

Steve Jones

Head of Biomedical Engineering

Doctoral Committee Members:
Steven Jones
Teresa Murray
Gergana Nestorova
Bryant Hollins

Approved:

Hisham Hegab
Dean of Engineering & Science

Approved:

Ramu Ramachandran
Dean of the Graduate School

GS Form 13a
(01/20)

ABSTRACT

Fractures and segmental bone defects are the primary cause of patient morbidity and brings a substantial economic burden to the healthcare system. Bone grafts used for bone injuries, tumors, and other pathologies related to poor fracture healing in the United States cost considerable money each year. The total cost of treating bone defects is about 5 billion US dollars. Autologous bone transplantation is the ideal method for the treatment of bone defects. However, their clinical results are variable and increase postoperative morbidity (especially at the donor site) and surgical costs. To circumvent these limitations, tissue engineering and cell-based therapies have been proposed as alternative methods to induce and promote bone repair.

In this study, we have developed a composite photo-crosslinked hydrogel with favorable mechanical properties and tunable bioactive properties. Furthermore, this composite hydrogel system, when combined with 3D printed scaffolds, can be modified to meet various applications for bone tissue regeneration applications. In this study, we identified the optimal combination between different concentrations of halloysite nanotubes (HNTs), strontium coated HNTs (SrHNTs), bone morphogenetic protein 2 (BMP-2), collagen methacrylated (COMA), and cross-linking time to develop a suitable scaffold. The scaffold is biocompatible and biodegradable, but also antibacterial and should promote faster healing.

The results suggest that gentamicin+SrHNTs+BMP-2 COMA hydrogel combined with a polycaprolactone (PCL) scaffold provides an optimal scaffold that can match the mechanical properties of bone. The next stage is to explore the scaffolds' application in biomedical engineering. To do this, animal testing will need to be performed. If the scaffold works in the animal model it will provide a meaningful treatment plan for bone tissue repair and regeneration.

APPROVAL FOR SCHOLARLY DISSEMINATION

The author grants to the Prescott Memorial Library of Louisiana Tech University the right to reproduce, by appropriate methods, upon request, any or all portions of this Thesis. It is understood that "proper request" consists of the agreement, on the part of the requesting party, that said reproduction is for his personal use and that subsequent reproduction will not occur without written approval of the author of this Thesis. Further, any portions of the Thesis used in books, papers, and other works must be appropriately referenced to this Thesis.

Finally, the author of this Thesis reserves the right to publish freely, in the literature, at any time, any or all portions of this Thesis.

Author _____

Date _____

TABLE OF CONTENTS

LIST OF FIGURES

ACKNOWLEDGMENTS

First, I would like to express my deepest thanks to my super advisor, Dr. David Mills. He gave me many suggestions on my research and many opportunities to learn instruments and techniques. These have played a key role in promoting my thesis research. Dr. Mills gave me enough support to try my ideas. He is always patient to help me solve my difficulties and improve my ability to solve problems. Without his support and guidance, it would be impossible for me to complete this work.

Secondly, I would like to to express my deepest appreciation to my committee, Dr. Steven Jones, Dr. Teresa Murray, Dr. Gergana Nestorova, and Dr. Bryant Hollins for serving on my comittee. Succsesful completion of my thesis would have been impossible with out their valuable advice.

Thirdly, I would like to express my heartfelt thanks to all the great laboratory partners, colleagues, and professors. I am especially grateful to Dr. Liu Xuan, Liu Meichen, Dr. Anusha Elumalai, Dr. Antwine McFarland, and Dr. Liu Mengcheng. I have received valuable help from all of you.

Finally, I would like to express my deep gratitude to my parents and my husband. They always encourage me to archive my goals, and they always support every decision I make. They always try their best to help me. They are my strongest supporters.

CHAPTER 1

INTRODUCTION

1.1 Bone Defect Repair

Successful treatment of many bone diseases and disorders remains limited due to a lack of safe and effective means of drug delivery that enhance bone tissue regeneration. Furthermore, despite significant advances, engineering a scaffold or drug delivery construct that delivers growth factors in a controlled manner has seldom been attained. The need for enhanced bone repair therapy, therefore, is a critical clinical concern.

The challenge remains to attain the controlled release of growth factors, such as BMP-2, in the range of nanograms or picograms per milliliter and over an extended period of seven to fourteen days, the typical time frame that progenitor cells differentiate into osteoblasts. In addition, for the hydrogels to be implantable or extruded as a bioink, they need mechanical properties that enable them to withstand the body's internal environment.

Tissue defects are repaired in a series of steps, including infiltration of host reparative cells (e.g., osteoblast and fibroblast) into the defect site, the proliferation and activation of the cells, and the deposition of extracellular matrices (ECMs) in the defects [1-3]. Osteoprogenitor and stem cells are attractive because of their unique ability to self-renew (multiply as undifferentiated (or pre-committed) cells), to be stored in biobanks, and to differentiate into various cell types in response to appropriate signals [3].

Cytokines and growth factors are critical signaling agents that control and coordinate progenitor and stem cell behavior in native bone tissue regeneration [4].

The rapid recruitment of osteoblasts and bone marrow-derived stem cells to skeletal defect sites and their proliferation and differentiation is essential for effective bone repair [1,2]. An alternative approach for skeletal repair is the directed selection, expansion, and modulation of osteoblasts, osteoprogenitor, and stem cells [1,2]. The bone repair and healing process in damaged or diseased bones could be accelerated if an increased number of native osteoblasts and progenitor cells were actively recruited to the site of injury. Upon arrival, these cells would replace diseased, damaged, or senescent cells and assist in repairing or renewing diseased or damaged tissues.

Several previous studies have used exogenous growth factors to recruit osteoblasts to the damaged site for a better therapeutic outcome [5,6]. The delivery of growth factors to the damaged site has become a widely used methodology that facilitates tissue repair by enhancing host cell recruitment, proliferation, and activation [7,8]. This approach has shown that faster recruitment of repair cells to the defect site can significantly reduce the time required for bone tissue repair and remodeling and can thus enhance bone reconstruction.

In bioengineered materials for bone repair, BMP-7 [9] platelet-derived growth factor (PDGF) [10], transforming growth factor-b (TGF-b) [11], insulin-like growth factors, vascular endothelial growth factor [12], and bone morphogenetic protein-2 (BMP-2) [11,12] have been used to manipulate cell behavior. Chemotactic cue-induced bone repair methods can prevent the migration of other types of cells, such as epithelial cells [13,14]. However, the application of chemical cues still poses several limitations,

such as the high cost of growth factors, the short half-life of growth factor proteins in vivo, and the potential adverse effects of overdose events or pathological conditions [13,14].

The development of orthopedic implant materials that promote osseointegration and reduce bacterial infection has gained considerable attention in recent years [15]. Previous studies in our lab have shown that halloysite nanotubes (HNTs) have an osteoinductive effect and can induce pre-osteoblasts and stem cells to differentiate into osteoblasts and produce a mineralized bone matrix [14,16]. Furthermore, numerous studies have shown that halloysite can serve as an excellent nanocontainer for the delivery of antibiotics [17,18]. As a bulk filler added to a polymer, HNTs provide material enhancements such as increased adhesiveness, fracture resistance, increased tension and compressive properties, and enhanced thermal capabilities.

The focus of this dissertation is to develop a system for enhancing the bone repair process. My dissertation research consists of three related projects that exploited the critical properties of HNTs for use in bioengineered materials for bone tissue regeneration. As first demonstrated in our lab, HNTs possess osteoconductive and osteogenic properties and can induce mesenchymal stem cells (MSCs) and pre-osteoblasts to differentiate into osteoblasts. We also hypothesize that HNTs are also chemotactic. Project #1 will directly address the chemotactic potential of halloysite nanotubes (HNTs) using a transmembrane migration culture system. This knowledge will then be used to develop a hydrogel system composed of methacrylate collagen and SRHNTs (Project #2) and to determine its effectiveness in inhibiting bacterial growth as

well as its tissue regenerative properties. The objective of Project #3 is to apply the hydrogel composite as a coating for 3D printed bone implants.

CHAPTER 2

BACKGROUND

2.1 Bone Biology

2.1.1 Basic Bone Biology – Matrix Composition

Bones comprise the internal support structure of vertebrates. Their functions are to move, support and protect the body, and to store minerals. Adults have 212 bones, while newborns have more than 270 bones [19,20] Human bones are categorized by shape as long bones, short bones, flat bones, irregular bones, and sesamoid bones (**Figure 2-1**) [21]. Long bones typically have lengths substantially larger than their width and are divided into a diaphysis and two epiphyses, which articulate with other bones to form joints. Inside the epiphyses is a complex honeycomb-like three-dimensional (3D) structure called spongy bone. Most diaphysis is composed of compact bone tissue, and in the middle is a bone marrow cavity containing cancellous bone and bone marrow. Most of the limb bones are classified as long bones (including the phalanges and toes) [21]. The classification of long bones depends on shape rather than size.

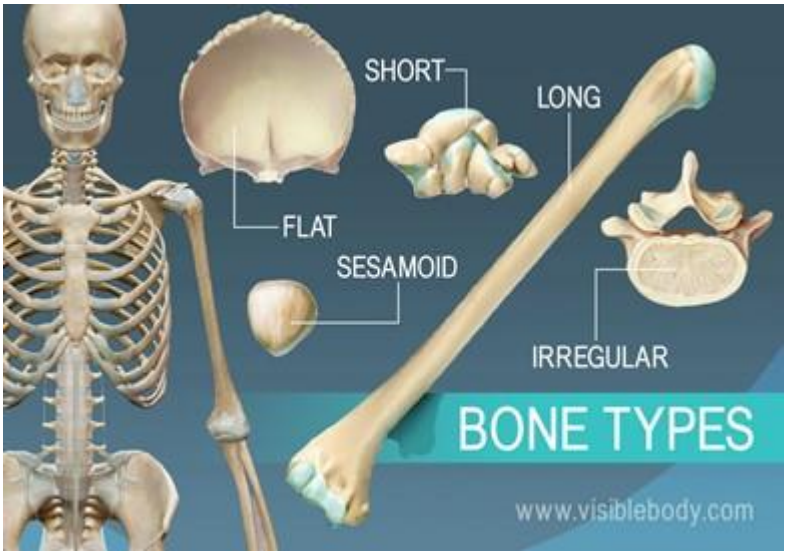

Figure 2-1: Bone cell types [22].

Short bones are cuboidal in morphology and the outer part is composed of dense compact bone and thin laminar bone. The interior is mostly composed of cancellous bone. The short and sesamoid bones make up the wrist and ankle joints, with some exceptions including the kneecap (patella), wrist, tarsus, and bones that make up the wrist and ankle joints. A flat bone is thin and curved, with two layers of dense bone sandwiching the middle layer of spongy bone. The skull and sternum are examples of flat bones [23]. An irregular bone, as the name suggests, is a complex-shaped bone, which does not easily fit in the classifications described above. In flat bones, a thin layer of dense bone surrounds cancellous bone. The bones of the spine and pelvis are irregular. A sesamoid bone is wrapped within a connective tissue such as a tendon. Its function is to keep the tendon away from the joint and increase the angle of tendon bending to increase muscle contraction, such as the patella and pisiform. Bone is composed of organic matter and inorganic matter. The organic matter is mainly type I collagen and minor bone proteins. Type I collagen provides a resilient component and toughness. The inorganic

matter, primarily calcium and phosphates salts that form hydroxyapatite, gives bone its hardness. Other tissues associated with bone include bone marrow, periosteum, nerves, blood vessels, and cartilage.

2.1.2 Bone Cell Types

The cellular components of bone tissue include osteocytes, osteogenic cells, osteoblasts, and osteoclasts [24]. Only the osteocyte exists within bone tissue, the other cells are located at the periphery of bone tissue.

Osteoblasts and Osteocytes

Osteoblasts are differentiated from osteogenic cells and are larger than osteogenic cells. They are short columnar or cuboidal-shaped cells. The nucleus is large and round, and the nucleoli are prominent (**Figure 2-2**). When bone grows and regenerates, osteoblasts are distributed into a regular layer on the surface of bone tissue. They secrete bone proteins in layers on the surrounding tissue and become embedded themselves to form osteoid. Mature osteoblasts found within bone are called osteocytes.

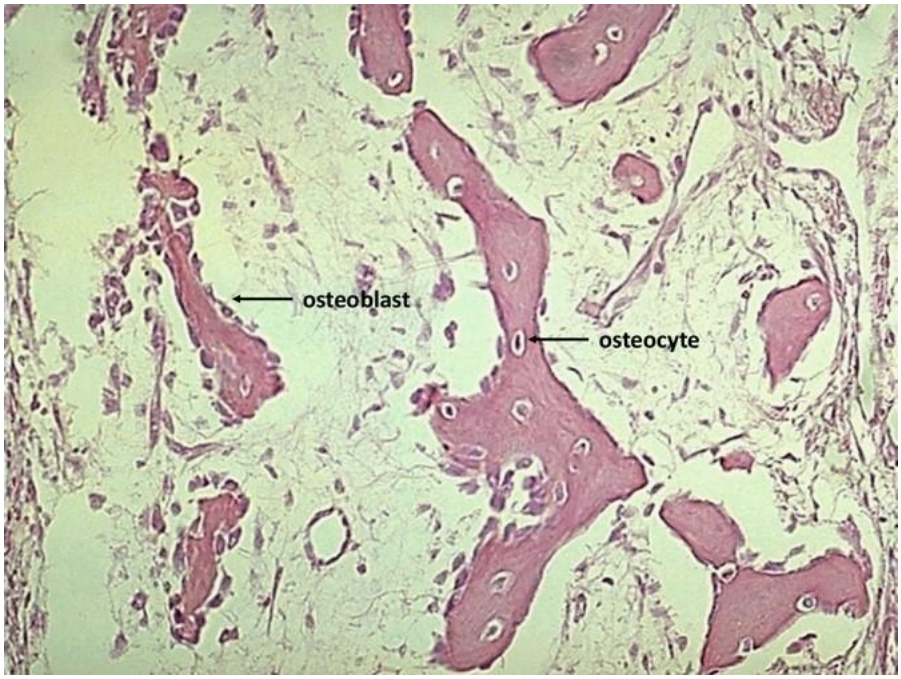

Figure 2-2: Bone cell types (H&E, courtesy of Dr. Mills)

Osteocytes are oblate star-shaped cells with oblate nuclei and deep staining. The cytoplasm is weakly basophilic. The human body of adults has about 42 billion osteocytes [25,26]. Osteocytes do not divide, with an average lifespan of 25 years. Osteocytes are sandwiched between two adjacent bone plates or distributed within the bone plates. Gap junctions are present between adjacent bone cells. In the bone matrix, the oval-shaped cavity surrounded by the cell body of the osteocytes is called a lacuna, and the surrounding osteocyte filopodia are call canaliculi. Adjacent bone pits are connected to each other by bone tubules which contain interstitial fluid from which bone cells get nutrients.

Osteoprogenitor Cells

Osteogenic cells are stem cells present in bone tissue. The cells are spindle-shaped, the cell body is small, the nucleus is oval, and the cytoplasm is weakly basophilic. Osteoblasts exist during the period of bone growth and development, or

during bone remodeling or bone tissue repair in adulthood. They can divide, proliferate, and differentiate into osteoblasts.

Osteoclasts

Osteoclasts are large, multi-nucleated cells with a diameter of up to 100 μm and 2 to 50 nuclei. Osteoclasts are derived from the monocyte-macrophage cell line. They have a strong eosinophilic cytoplasm. It is multinucleated. The cytoplasm at the base is rich in lysosomes and vesicles.

2.1.3 Bone Repair and Regeneration

Bone healing occurs in three distinct but overlapping stages: the early inflammatory stage, the repair stage, and the late remodeling stage [27,28]. In the inflammatory stage, inflammatory cells (macrophages, monocytes, lymphocytes, and polymorphonuclear cells) and fibroblasts infiltrate the bone under prostaglandin stimulation and results in the formation of granulation tissue, ingrowth of vascular tissue, and migration of mesenchymal cells [29].

In this process, the exposed cancellous bone and muscle provide the primary nutrient and oxygen supply [29]. Interleukin 6 (IL-6) promotes differentiation of osteoblasts and osteoclasts [30]. Fibroblasts lay down a stroma that supports vascular ingrowth during the repair stage [29]. Osteoid is secreted and subsequently mineralized while the collagen matrix is laid down, which leads to the formation of a soft callus around the repair site [31]. After the collagen matrix of hyaline cartilage or woven bone becomes mineralized, the lamellar bone begins forming. Then numerous osteoblasts are recruited and form new lamellar bone upon the recently exposed surface of the mineralized matrix. During the remodeling stage, bone healing is completed [29]. The

healing bone is restored to its original shape, structure, and mechanical strength [29]. Remodeling of the bone occurs slowly over months to years and is generally laid down where it is needed under the influence of mechanical loads [29].

2.2 Overview of Bone Tissue Engineering

Fractures and segmental bone defects are a large economic burden to the healthcare system due to their high rate of occurrence [32]. Bone grafts, tumors, and other pathologies are extremely costly furthering the economic burden, for example, treatment for bone defects is estimated to cost $5 Billion annually in the United States alone [32].

Bone tissue can naturally heal small bone defects, such as cracks and some types of fractures. However, bone defects that exceed 2 cm, depending on the anatomical site, will not heal by themselves [33-35]. Currently, the gold-standard treatment for large bone defects uses biologically inert metallic devices, bone autografts, and allografts [36,37]. However, metal bone-fixation devices are invasive and will require a second surgery to remove, bone allografts on the other hand run the risk of disease transmission from contaminated donor material as well as additional morbidity associated with healing of the donor site [38]. Bone tissue engineering provides another option for bone regeneration at the defect site without incurring these risks [39]. Bone tissue engineering is an interdisciplinary field that uses cells, biocompatible materials, and suitable biochemical factors toward the development of biological substitutes that restore, maintain, or improve bone tissue function [38]. Advances in materials science and understanding of bone biology and structure have allowed for the design of more sophisticated materials for use in bone-tissue engineering [38]. The goal of bone tissue

engineering is to introduce specialized materials to a bone defect and then allow the patient's cells to heal the defect [38]. These materials are seeded into a scaffold, which is used as a support structure for cellular adhesion and deposition of the mineralized matrix [38]. The scaffold is meant to temporarily replace the ECM in redeveloping the tissue [38].

2.3 Bone Tissue Engineering – State of The Art

A large variety of material types and combinations are promising for bone tissue engineering [38]. Since the composition of natural bone tissue is both organic and inorganic, polymers, bioceramics, and composite materials become the most common biomaterials used for bone-tissue-engineering [38]. Polymers are organic materials. They are formed from long chains of covalently bonded atoms [40]. Both natural—e.g., collagen, gelatin, alginate, alginate and gelatin copolymers—and synthetic—e.g., poly(ε-caprolactone), poly(l-lactic acid), poly(lactic-co-glycolic acid)—polymers are used widely in bone tissue engineering. Compared to the natural polymer commonly used in bone tissue engineering, some of the new polymers, such as silk, are gaining increased attention due to their ease of processing, outstanding mechanical properties, and ability to guide hydroxyapatite formation [41-44]. Examples of such materials are: Poly(propylene fumarate), a synthetic polymer with similar mechanical properties to the bone, biocompatible degradation, and ability to photo crosslinking, and poly(N-isopropylacrylamide), a thermoresponsive polymer capable of being copolymerized or combined with different polymers to produce thermogelling hydrogels [45-47].

Bioceramics are inorganic biomaterials that have been important in bone-tissue engineering [38]. These materials are generally (crystalline) ceramics, (amorphous)

glasses, or (partly crystalline) glass ceramics [38]. The most common bioactive ceramic used for bone-tissue engineering are calcium phosphates because they can mimic the inorganic phase of bone, carbonated hydroxyapatite [38]. These materials are currently used in clinical settings as injectable bone cements or coatings for implants [48]. Hydroxyapatite and β-tricalcium phosphate ceramics are two calcium phosphate-based biomaterials used in bone tissue engineering [38]. Hydroxyapatite is favorable due to its slow degradation rate, while β-tricalcium phosphate is a resorbable bioceramic [38]. In large animal models bioceramic granules composed of both calcium phosphates have been shown to form a mineralized tissue comparable to bone autografts [49]. Bioactive glasses, another class of bioceramics, are mainly composed of calcium-containing silicates, however, phosphate and borate derivatives are also in development [38]. Moreover, mesoporous bioactive glasses are attractive multifunctional materials able to be loaded with various drugs or biomolecules, enabled by their nanoporosity (2–50 nm diameter) [50,51].

Metals are valued for their high mechanical performance.37 Titanium, magnesium, and their alloys are the most used metals because they are highly biocompatible [36,52,53]. Carbon nanotubes [54,55], graphene, and graphene oxide nanoparticles [56-63] are attractive biomaterials in bone-tissue-engineering due to their exceptional mechanical properties and large surface areas which facilitate non-covalent interactions with physiological ions and biomolecules.

Composite biomaterials are promising biomimetic solutions to overcome substantial challenges in the field of bone-tissue-engineering regardless of the composite nature of bone and the complexity of the material specifications [38]. The most common

types of filler composites in bone-tissue engineering are bioactive ceramic and glass particles [64-69]. Nanoparticulate fillers can be exploited to add greater functionality to the composites [38]. For example, magnetic iron oxide nanoparticles incorporated in a PCL matrix and exposed to an external static magnetic field may facilitate enhanced osteoblastic differentiation and bone formation in the resulting composite [70]. Composites made entirely of particles have been used to develop modular material systems [38]. These systems are composed of various particle types that act as building blocks and enable unique properties, such as self-healing [66-71]. Another class of composite systems is ceramic–matrix or glass–matrix composites [38]. Bioceramic β-tricalcium phosphate scaffolds can be coated with graphene oxide nanosheets, which endow the scaffold with improved osteogenic capacity and photothermal properties that enables the deactivation of residual bone tumor cells via light therapy [62].

In addition, fabrication technology influences a wide range of biomaterial properties, from morphological (for example, pore architecture) to physicochemical (such as degradation), mechanical (such as compressive modulus), and biological (such as cell infiltration) [38]. Materials can be fabricated into microparticles, nanoparticles [52,74-80], fibres [81-88], coatings [68,78,89-91], films [65,68,92,93], and 3D constructs [34,47,61,69,84,94-111] to fit a specific need or design requirements. Two major technologies are used for fabrication, 3D printing, and electric-field-assisted techniques. The forms of 3D printing used for bone-tissue-engineering materials are generally extrusion, stereolithography, selective laser sintering, and inkjet printing [38]. Several biomaterial fabrication techniques use an electric field to form particles, fibers, coatings, films, and 3D constructs, the most common of which is electrospinning [38].

Electrospinning uses an electric field applied between a syringe and a collector to form microfibers and nanofibers [112]. New techniques are in development that combine an electrical area with other fabrication principles [38]. For example, an electrical field can be applied in an inkjet printing set-up to enable 3D printing via deposition of hydrogel microdroplets [113]. Another example of this approach is the use of a computer-controlled moving collector and syringe to ensure precise layer-by-layer deposition of predesigned fiber patterns to produce a 3D construct [114].

Another electric-field-assisted method that has been explored is electrospraying, which is harnessed to manufacture particles [115] or coatings [116]. Electrophoretic deposition (EPD) is used to fabricate coatings or films derived from particulate biomaterials [38].

2.3.1 Hydrogels

Hydrogels are hydrophilic materials that can be of either natural or synthetic composition [117]. Normally, hydrogels swell when exposed to a large amount of water, but they do not dissolve [118]. In this way, they resemble loose connective tissue. Hydrogels have been classified in various ways, typically based on their bonds, and can be grouped as either physical hydrogels or chemical hydrogels [119,120]. Physical hydrogels form through the application of physical forces, such as electrostatic interactions, hydrogen bonding, and chain twining [121]. Physical hydrogels do not have permanent junctions and heating the hydrogel can cause it to transform into a liquid. Chemical hydrogels are three-dimensional network polymers that are cross-linked through the formation of covalent bonds. Compared to physical hydrogels, chemical

hydrogels form permanent constructs, which means they will not transform into a liquid [121].

Hydrogels can also be classified into two groups based on their source: natural polymer hydrogels and synthetic polymer hydrogels [118]. Natural polymer hydrogels, obtained from natural sources, include gelatin, collagen, chitosan, alginate, agarose fibrin, and hyaluronic acid [122]. Natural polymer hydrogels are either composed of the native extracellular matrix (ECM) or have macromolecular properties similar to a natural ECM [122]. Although the natural polymer material is less stable and biodegrades readily, it has better biocompatibility, greater environmental sensitivity, lower cost, and better availability. These benefits have led to increased research on natural hydrogels.

Synthetic polymer hydrogels include such examples as poly(ethylene oxide) (PEO), poly(vinyl alcohol) (PVA), poly(acrylic acid) (PAA), poly(propylene fumarate-co-ethylene glycol) (P(PF-co-EG)), and polypeptides [122]. Synthetic polymers can be modified to have specific molecular weights, block structures, degradable linkages, and cross-linking properties [122]. The manipulation of these properties makes synthetic polymers' chemical properties and mechanical properties controllable, and reproducible [122]. Synthetic polymers are hydrophobic by nature. Compared to natural polymers, synthetic polymers are chemically and mechanically more durable [118]. However, the mechanical strength leads many synthetic hydrogels to have poor biodegradation properties. Also, during the synthetic hydrogels' preparation process, toxic residues are potentially left in the gels. These will be released into the body as the scaffold biodegrades, which may cause significant tissue rejection.

Hydrogels, according to their biological responsiveness to external stimuli, can be divided into two categories - conventional hydrogels and environmentally sensitive hydrogels. Conventional hydrogels are not sensitive to environmental changes such as changes in temperature and pH. Environmentally sensitive hydrogels are designed with controllable responses such as the ability to shrink or expand with changes in external environmental conditions [118]. Environmentally sensitive hydrogels respond to changes in the external environment (such as temperature, pH, light, electricity, and pressure) or minor stimulation. They can produce a corresponding change in the volume transition [118]. The salient features of such a gel are a significant change in response to the environment during the swelling process [118]. The use of this stimulus-response may be applied to such devices as sensors, switches, and other switch-release devices.

Hydrogels can be used in a diverse array of applications including in hygienic products [123], agriculture [124], drug delivery systems [123,125], sealing [123], coal dewatering [126], artificial snow [123], food additives [127], pharmaceuticals [128], biomedical applications [129-130] tissue engineering and regenerative medicines [131,132], diagnostics [133], wound dressing [134], separation of biomolecules or cells [135], barrier materials to regulate biological adhesions [136], and biosensors.

2.3.2 Coatings and Films

Coatings are divided into organic, inorganic, and composite and their usage are determined based on the material they are applied to [137]. Surface coatings on implants are formed using various technologies, such as electrophoretic deposition, sol-gel technique, enameling, physical vapor deposition (pulsed lased deposition and pulsed electron deposition), and magnetron sputtering [138]. The most frequently developed

inorganic coating for biomaterials (mainly metallic implants) is calcium phosphate (CaP) (e.g., hydroxyapatite (HA; Ca10(PO4)6(OH)2), TCP, or CaP glass-ceramics) [139]. CaP-based bioactive layers on an implant surface improve osseointegration between the biomaterial and host tissue [139]. Importantly, the chemical similarities of CaP-based coatings to natural bone HA enhance the ability of coated biomaterials to provoke an appropriate host response [140,141]. Moreover, metallic implants benefit extensively from CaP-based coatings as they can boost corrosion resistance and reduced metal ion release to the implantation site [142]. Multiple studies have demonstrated that CaP-based coatings can promote osteoblast attachment, proliferation, and differentiation [139]. Mumith et al. [143] used an in vivo sheep model to demonstrate that SiHA and strontium-substituted HA (SrHA) electrochemical coatings improved osseointegration of a Ti–6Al–4V implant when compared to and uncoated control. Mokkaber et al. [144] developed CaP coating containing silver (Ag/CaP) through electrochemical deposition on Ti substrates. The objective of these coatings was to enhance the biocompatibility and antibacterial properties of the biomaterials implemented in bone regeneration. They observed that Ag/CaP coating, where silver as deposited as metallic nanoparticles on the CaP coating, showed no cytotoxicity towards osteosarcoma-derived osteoblast-like cells (Saos-2 cell line), but also antibacterial activity. Moreover, the biocompatibility of the coating was confirmed by the well distributed and adhered Saos-2 cells cultured on the surface of the samples. Other ceramic coatings, such as oxides, piezoelectric and ferroelectric ceramics, carbides, and zeolites coatings, may also possess great potential to accelerate bone tissue regeneration [139].

In a study performed by Huang et al. [145], evaluation of the osteoconductive and osteoinductive properties of the magnetic iron/polydopamine (Fe_3O_4/PDA) coating were conducted using in vitro (human bone marrow-derived mesenchymal stem cells (BMDSCs)) and an in vivo (rabbit femoral bone defects) model. The coating was fabricated through co-deposition of Fe_3O_4 nanoparticles and PDA on the surface of 3D-printed porous Ti scaffolds. The Fe_3O_4/PDA coating supported cell adhesion, proliferation, and osteogenic differentiation of BMDSCs and enhanced new bone formation in vivo. Moreover, researchers observed that an applied static magnetic field resulted in the enhancement of the osteogenic ability of the coating.

Piezoelectric ceramics, such as barium titanate ($BaTiO_3$) [146-148], lead-free zirconate titanate derivatives—e.g., $(Ba,Ca)(Zr,Ti)O_3$) [149], and lithium tantalate ($LiTaO_3$) [150], are often chosen as materials to promote bone growth, remodeling, and regeneration because they are biocompatible and enhance osseointegration. Moreover, piezoelectric biomaterials may generate a bioelectrical signal that mimics the stress-generated potentials of natural bone, when exposed to mechanical stress [139]. These types of biomaterials may also be able to promote bone healing when subjected to electrical stimulation or ultrasound [151].

Zeolites are crystalline materials with precisely defined pore structure and high stability [139]. Zeolites have good biocompatibility, antioxidant, antimicrobial, anti-apoptotic, and anti-inflammatory activity [139]. These features make zeolites an ideal coating material for metallic implants [152]. Chen et al. [153] modified a Ti substrate surface with zeolitic imidazolate framework-8 (ZIF-8). ZIF-8 is a Zn-based metal-organic framework belonging to nanoporous solid crystals. Hydrothermal and solvothermal

methods were used to deposit ZIF-8 films with nanoscale and microscale sizes onto Ti substrates. The nanoporous ZIF-8 film inhibited Staphylococcus growth, demonstrated good biocompatibility, enhanced ECM mineralization, and increased the expression of bALP and Runx2 genes in MG63 cells. However, the microporous ZIF-8 film exhibited cytotoxicity to MG63 cells.

Carbon coatings (in the form of nanocrystalline or polycrystalline diamond, diamond-like carbon, amorphous carbon, carbon nanotubes, or graphene) have non-cytotoxic characteristics and are used as coatings for metallic biomaterials which provides them with increased biocompatibility [140,154-157]. Rifai et al. [155] showed that coating a Ti scaffold with polycrystalline diamond promoted attachment and proliferation of Chinese Hamster Ovarian (CHO) cells and enhanced apatite deposition. Another promising material used as an inorganic coating on bone implants is boron nitride (BN) [121]. BN nanotubes are biocompatible and enhance attachment, growth, and osteogenic differentiation of rat BMDSCs in vitro [158].

Natural and synthetic polymers that are beneficial as coatings for metal and ceramic biomaterials in bone tissue applications are proteins such as laminin [159,160] whey protein isolate [161], collagen [162], and BMP-2 [163], all of which are organic materials. Organic coatings have high cytocompatibility, biodegradability, and may also prevent metallic implants and ceramic materials from corroding and degrading [164]. Most polymers are highly biocompatible, which makes them ideal for use with incompatible biomaterials [139]. Moreover, the inherent structure of some polymers can mimic the microstructural properties of the bone ECM [147]. Zhao et al. [162] studied the response of murine embryonic fibroblasts (C3H10T1/2 cell line) to polyelectrolyte

multilayer coatings composed of hyaluronic acid/collagen or chondroitin sulfate/collagen. Cells cultured on the chondroitin sulfate-based samples had a more elongated morphology when compared to cells cultured on the hyaluronic acid-based samples. Thus, demonstrating that the cells adhered better to the chondroitin sulfate/collagen coating. Also, cells grown on the chondroitin sulfate-based samples exhibited noticeably higher ALP activity.

Recently the application of composite coating has garnered much interest due to the potential for it to mimic the natural bone environment and accelerate bone regeneration [139]. Furthermore, composite coatings may produce a synergetic effect between two or more coating components [139]. Yu et al. [166] used a biomimetic coating process to develop Ti–6Al–4V substrates coated with HA and collagen-HA (Col/HA) composite. They demonstrated that osteoblasts cultured on the surface of the biomaterial with Col/HA coating displayed a slightly higher cell proliferation rate when compared to the HA coating. They also showed enhanced cell adhesion and spreading on the surface of Ti–6Al–4V coated by both HA and Col/HA composite.

2.3.3 Scaffolds

Traditionally, bone grafts have been used to restore damaged bone [149]. However, bone grafts are restricted by size. Currently, more and more synthetic biomaterials are now being used as bone graft replacements [167]. These biomaterials were initially selected based on their biomechanical properties [167]. Later scaffolds were engineered to be biocompatible or biodegradable to reduce harmful effects. Now scaffolds are designed to induce bone formation, vascularization and reduce infection

[167]. These scaffolds are often seeded or coated with growth factors (TGFb, BMP, IGF, FGF, and VEGF), drugs, and cells (e.g., stem cells, pre-osteoblasts).

An ideal scaffold requires the materials to be biocompatible and bioresorbable, to have a reasonable pore size, and to have similar mechanical properties to the host tissue. The ideal pore size of a scaffold is at least 100 μm in diameter, which allows successful diffusion of essential nutrients and oxygen for cell survivability [168]. Previous research found that the optimum pore size for bone tissue in-growth is 200-350 μm Scaffolds [169]. Also, scaffolds involving both micro and macro porosities perform better than only microporous scaffolds [170]. However, porosity reduces the mechanical properties of the scaffolds and makes consistent reproduction difficult [167]. Currently, polymers, ceramics, composites, and metals are the primary materials for fabricating scaffolds [167]. Mechanical properties of bone differ between types from cancellous to cortical bone [167]. Young's modulus of cortical bone is between 15 and 20 GPa, and the Young's modulus of cancellous bone is between 0.1and 2 GPa [167]. The compressive strength of cortical bone varies between 100 and 200 MPa, and for cancellous bone between 2 and 20 MPa [167]. The large variation in mechanical properties and geometry makes it difficult to design an 'ideal bone scaffold' [171].

Another important factor for scaffold design is bioresorbability [172]. An ideal scaffold degrades with a resorption rate such that the new bone tissue occupies the newly opened space [167]. The degradation time of a scaffold should be tunable to the specific need of the individual patient. For example, scaffolds used to repair spinal fusion require 9 months or more to complete the process, while scaffolds for craniomaxillofacial applications require 3–6 months [167].

2.4 Halloysite Structure and Applications

Halloysite nanotubes (HNTs) are naturally occurring aluminosilicate nanoparticles that have a structure and chemical composition like kaolinite, dickite, or nacrite [173-175]. HNTs are mined from various mineral deposits making it an easily accessible nanomaterial. Unlike kaolinite, dickite, or nacrite, the unit layers in halloysite are separated by a monolayer of water molecules [173-175]. As a result, a hydrated halloysite has a basal (d_{001}) spacing of 10 Å which is approximately 3 Å larger than that of kaolinite. Halloysite-(10 Å) can readily and irreversibly dehydrate to give the corresponding halloysite-(7 Å) form [176] when halloysite-(10 Å) is heated to 90-150 °C. HNTs can be wildly found in China, France, Belgium, New Zealand, America, and Brazil [177-181]. The chemical composition for halloysite-(7 Å) and halloysite-(10 Å) is $Al_2Si_2O_5(OH)_4 \cdot nH_2O$ where n = 0 and 2, respectively [177,182,183]. If n is 2, the HNTs are hydrated, and if n is 0, the HNTs are dehydrated [182,183]. AIPEA Nomenclature Committee recommended terms halloysite-(10 Å) for the hydrated mineral and halloysite-(7 Å) for the dehydrated form.

The particles of halloysite can adopt a variety of morphologies, the most common of which is the elongated tubule (**Figure 2-3**). However, short tubular, spheroidal and plate particle shapes have all been widely reported [185-192]. Spheroidal halloysite occurs widely. The diameter ranges of spheroidal halloysite are from 0.05 to ~0.50 mm [190,193,194]. It is common to find pseudo-spherical or spheroidal particles in weathered volcanic ashes and pumices [190,191,193-201].

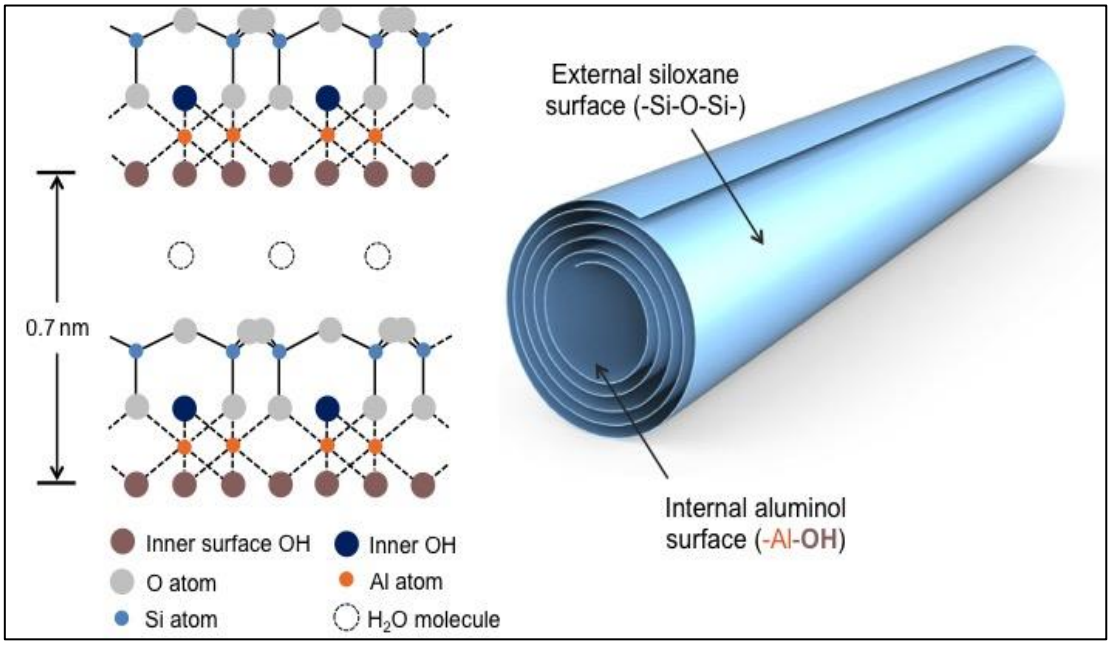

Figure 2-3: The structure of HNTs and their potential for surface modification [184].

The predominant form of HNTs is a hollow tubular structure in the submicrometer range. The tubules may be extended and thin, short, and stubby, or emerging from other tubes [186,190,195,198,202-208]. The halloysite tubules' size varies from 500-1000 nm in length with an outer diameter of 10-50 nm and an inner diameter measuring 5-20 nm depending on the deposit [182,183]. The neighboring alumina and silica layers, and their hydration layers, create a packing disorder causing them to curve and roll up, forming multilayer tubes. The HNT external surface is comprised of O-Si-O bonds with terminal hydroxyl groups [177,182,183]. The inner lumen consists of O-Al-O bonds, terminating in hydroxyl groups [177,182,183]. At pH 8.5 and below, these inner hydroxyl groups are mostly protonated, resulting in a positive charge on the inner lumen [177,182,183].

A wide range of active agents, including antibiotics, cancer drugs, marine biocides, and biological molecules, can be entrapped within the inner lumen and void

spaces within the aluminosilicate shells [209]. HNTs nanotubes are non-cytotoxic on several cell types (up to concentrations of 0.1 mg/mL), including chondrocytes, dermal fibroblasts, osteoblasts, and stem cells on halloysite nanofilms or within HNT-hydrogel composites [210,211]. Examination of halloysite with in-vitro assays showed cells proliferated and maintained their cellular phenotype. Several recent biocompatibility studies have shown that HNTs do not provoke a cytotoxic response or a host immune response [212,213]. As halloysite nanotubes exhibit high biocompatibility levels and exceptionally low cytotoxicity, they represent an ideal candidate for new drug delivery and polymer systems.

2.4.1 Halloysite–Drug Delivery

HNTs have been used as a drug delivery carrier for many clinically meaningful drugs [17]. HNT can be loaded with different drugs, including anticancer drugs, antibiotics, analgesics, antihypertension, anti-inflammatory drugs, and therapeutic nucleic acids [18]. HNTs have been used for the controlled release of antibiotics, including tetracycline, ofloxacin, norfloxacin, amoxicillin, and ciprofloxacin [18]. Amoxicillin (AMX) loaded HNT is incorporated into a polylactic acid-glycolic acid copolymer (PLGA) solution, which is electrospun with water-soluble chitosan nanofibers in two different syringes simultaneously, thereby making a composite material [214]. Compared to loading the drug directly into the polymer matrix, HNT extends the release time of AMX and reduces the initial burst release [214].

Analgesic drugs and anti-inflammatories such as ibuprofen (IBU), diclofenac sodium, and aspirin have low water solubility and low bioavailability, which are universal problems [18]. Therefore, the development of an efficient drug delivery system

by encapsulating drugs in a nanoparticle system for enhancing their bioavailability is an urgent necessity [18]. 3-aminopropyltriethoxysilane (APTES) functionalized surface HNT as a carrier for IBU could promote the loading of IBU [215]. By restriction of the APTES oligomerization in the lumen, free lumen space was preserved and resulted in a 25.4% greater loading rate than that in unmodified halloysite [215]. To sustain greater release of IBU, an ideal hydrophobic sustained-release drug delivery system was designed [216]. The preparation combined the techniques of enlarging the HNT lumen (EHNT) and hydrophobic modification of the external surface by Organosilane (OS) [216]. The OS composite EHNT demonstrated a sustained-release performance for IBU (100 h) [216]. Other drug delivery systems such as halloysite–based anti-hypertension drug- delivery system, and halloysite-based gene therapeutic agent delivery system. Polydopamine was used to cap HNT for controlled release [217]. After dispersion in a sodium alginate matrix, and crosslinking via Fe^{3+}, the nanocarrier is used for the delivery of Diltiazem hydrochloride, which is heavily used in high blood pressure therapy [217]. In gene therapeutic agent-delivery systems, HNTs were surface-modified with γ-aminopropyltriethoxysilane and assembled with antisense oligodeoxynucleotides (ASODNs) [218]. These functional HNT complexes improved intracellular delivery efficiency and inhibited the tumor growth activity of ASODNs [218].

2.4.2 Halloysite–Tissue Engineering

HNTs have a variety of applications in the field of tissue engineering. They are used in bone implants, dental fillings, and tissue scaffolds [218]. HNT mixed with bone cement and used as a drug carrier and release system is one of the most common applications. HNTs loaded with the antibiotic gentamicin sulfate with a concentration of

5 to 8 wt% in the cement (PMMA) provided sustained release up to 400 h [220]. This PMMA/halloysite/gentamicin composite tensile strength does not deteriorate as compared with pure cement and its adhesion to bone is significantly increased [220]. HNTs resin-dentin bond is similar to halloysite-PMMA bone cement [221]. HNT and functionalized HNT both improved mechanical properties significantly [221-223]. Silver nanoparticle immobilized HNT (HNT/Ag) fillers significantly improved mechanical properties [224]. This filler also showed significant antibacterial activity on S. mutans [224].

Currently, hydrogel scaffolds are being applied to transplant cells and engineer nearly every tissue in the body, including cartilage, bone, and smooth muscle [225]. Alginate/halloysite nanotube (HNTs) composite scaffolds compared to pure alginate scaffolds significantly enhance compressive strength and compressive modulus in dry and wet states [226]. HNTs increased the scaffold density, decreased the swelling ratio in water, and improved alginate's thermal stability [225]. The alginate/HNT composite scaffolds have better cytocompatibility [226]. Chitosan–halloysite nanotubes (HNTs) nanocomposite (NC) scaffolds have similar results as alginate HNTs composite scaffolds [227]. Compared to the pure chitosan scaffold, the NC scaffolds exhibited significant enhancement in compressive strength, compressive modulus, and thermal stability [227]. The chitosan–HNTs nanocomposites were cytocompatible even when the HNTs load was 80% [227].

2.5 Strontium Structure and Applications

The element strontium (**Figure 2-4**) was discovered around 1790 in a mine near the Scottish village Strontian and was isolated 1808 [229]. Sr is an alkaline earth metal. It

never occurs on its own in nature, because metallic Sr oxidizes easily forming yellowish-colored strontium oxide [229]. Sr is a soft, silver-white, shiny, and highly conductive metal. When Sr is burned it produces a red flame. There are four stable isotopes of ^{84}Sr (0.56%), ^{86}Sr (9.86%), ^{87}Sr (7.02%), and ^{88}Sr (82.56%) [229]. Strontium is the second least abundant alkaline earth metal. The main ores in which strontium exists are celestite ($SrSO_4$) and strontium carbonate ($SrCO_3$) [229]. Celestite is mainly used to make $SrCO_3$. Because strontium carbonate can produce other Sr compounds, it is used to purify Zn (removing Pb and Cd) for making permanent ceramic magnets, and it is the most important Sr compound for making TV screens. $Sr(NO_3)_2$ is used in pyrotechnic devices, SrO is used in aluminum smelting, Sr and $SrCl_2$ are used to repair teeth, and $Sr(OH)_2$ has long been used in the purification of molasses.

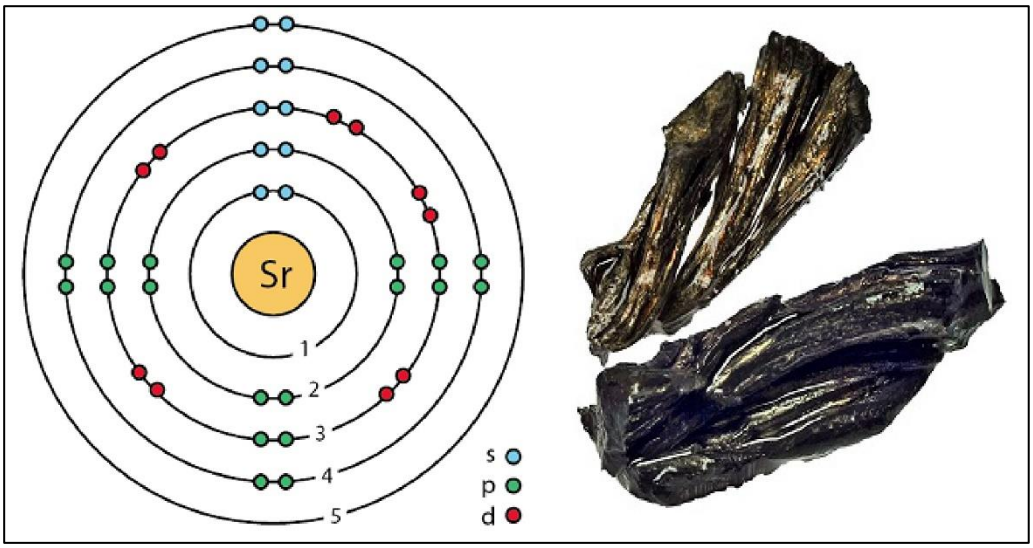

Figure 2-4: Structure of Sr and Sr metal [228].

The human body mainly acquires strontium via food and water and is absorbed in the digestive tract and excreted in the urine. The small intestine has two absorption mechanisms for strontium: active transport and passive diffusion. The bones hold 99.1%

of the strontium in the body and only 0.7% in the extracellular fluid [230]. Strontium regulates the differentiation of MSCs (mesenchymal stem cells) into osteoblasts and promotes synthesis and precipitation of bone matrix proteins [231]. Therefore, strontium is a strong promoter of osteoblast differentiation and bone formation. The coordinated interaction between osteoblasts and osteoclasts is key to the regulation of bone regrowth and maintaining the stability and integrity of bones [232]. Strontium has at least two mechanisms for increasing the proliferation of pre-osteoblasts and pluripotent stem cells [233,234]. In addition strontium improved bone metabolism, prevented bone loss, and improved bone quality in osteoporotic animals [235]. In bones, strontium can replace a small amount of calcium in calcified tissue and tooth hydroxyapatite crystals [236]. An appropriate amount of strontium can improve the mechanical properties of bone and lead to an obvious increase in hardness [237].

2.5.1 Strontium and Bone Tissue Engineering

Strontium–hardystonite–gahnite (Sr–HT-gahnite; Sr–$Ca_2ZnSi_2O_7$–$ZnAl_2O_4$) bioceramics have been regarded as important for bone reconstruction because their elemental composition and mechanical strength are similar to cancellous bone [238]. Wang et al. prepared porous Sr–HT–gahnite bioceramics and investigated them as carriers for adipose-derived stem cells (ASCs) [239]. They selected these materials to take advantage of osteogenic activity and angiogenic stimulation of the calcium silicate-based bioceramics. In a critical-sized calvarial bone defect model in rats, the synergistic effect of the Sr–HT–gahnite/ASCs composite facilitated osteogenesis, angiogenesis, and vascularized bone formation in vivo.

Extended release of silicon (Si) ions from calcium silicate-based ceramics into the microenvironment augments osteogenic activity [240]. Xu et al. synthesize 3D porous strontium zinc silicate (SZnS, $Sr_2ZnSi_2O_7$) scaffolds and assessed their in situ mineralized layer (carbonated calcium phosphate) formation potential using the sponge impregnation technique [241]. In vitro cell behavior and in vivo bone formation on radial bone defects were used to establish that scaffolds with a mineralized layer arrested the initial burst of ions and considerably improved the cell adhesion over a mineralized layer-free scaffold.

Calcium phosphate-based ceramic biomaterials are structurally like natural bone; however, their low bioactivity limits their clinical use [238]. Ehret et al. doped the material with Sr ions and optimized the content of hydroxyapatite (HA) in a natural polysaccharide–hydroxyapatite matrix to promote bioactivity [242]. Implantation of 30% HA to polysaccharides ratio (w/w) showed considerable improvement on ectopic bone tissue mineralization in the ectopic site of mice. Both in vitro and in vivo results revealed partial replacement of calcium in HA by Sr-enriched tissue mineralization, osteoid, and new blood vessel formation.

Although a variety of natural and synthetic polymers have been used to develop synthetic implant scaffolds, only a few have had success when implemented for bone tissue engineering [243]. They are disadvantaged by inadequate biomechanical properties and biodegradation rate [243]. Ceramics and/or growth factors are applied to polymer scaffolds to overcome these issues [238]. Recently, a novel nanobiocomposite was developed by reinforcing a collagen (Col) scaffold with strontium-graphene oxide (Sr-GO) for large bone defect reconstruction [244]. Incorporation of Sr-GO improved cell adhesion, osteogenic differentiation, and in vitro tube formation of endothelial cells in the

scaffold. The resultant bone repair and defect bridging after 12 weeks of transplantation indicated the potential of the Sr-GO-Col scaffolds for repairing critical-size calvarial defects in rats. These results were due to the synergistic contribution of GO and Sr in the MAPK signaling mechanism. It was concluded that Sr-GO-Col scaffolds facilitate favorable environmental conditions for promoting bone regeneration. PCL is a biocompatible polymer scaffold with good mechanical properties [238]. An $SrCl_2$ and PCL coating was used to improve the performance of porous calcined porcine bone (CPB) [245]. The positive impact of incorporated Sr and PCL on cell responses and bone reconstruction was demonstrated when a considerable increase was found in the in vivo bone formation outcome of CPB/PCL/Sr scaffold when compared to CPB and CPB/PCL.

In conclusion, Sr is a safe and effective doping material for stimulating bone formation and regrowth. Its effectiveness may be more pronounced and variable over time depending on the concentration applied. It is important to develop adequate models and form consistent guidelines for research in future studies to better define the therapeutic application of this element.

2.5.2 Strontium-Coated HNTs and Bone Tissue Engineering

The development of orthopedic implant materials which promote osseointegration and reduce bacterial infection has gained considerable attention recently [15]. These implants are being developed to avoid long-term complications. A study reports the electrodeposition of strontium-halloysite nanotubes (Sr-Hal)/lanthanum, cerium substituted hydroxyapatite (La,Ce-HAP) composite coatings on titanium surface with varying Sr-Hal concentrations at 1, 2, and 3 wt%.15 The results of the said study showed that the mechanical properties of the composite coatings were improved by the

incorporation of Sr-Hal. The anti-corrosion properties of the Sr-Hal/La,Ce-HAP composite-coated Ti with 3 wt% Sr-Hal were found to be excellent compared to the other wt%s. The antibacterial, anti-cancer, and cell viability study of Sr-Hal/La,Ce-HAP composite coatings revealed antibacterial effects, osteosarcoma cell growth impediment, and a higher number of viable cells.

Among strontium-based drugs, Strontium ranelate (SrR) is a divalent strontium salt of ranelic acid which improves the bone microarchitecture [246]. However, some findings reveal that the SrR negatively affects cell proliferation and osteoblastic differentiation, depending on its concentration [246]. The incorporation of halloysite nanotubes (HNT) as nanocarriers of SrR, into gelatin (GN) coatings, tailors the release of this anabolic bone-forming and anti-catabolic agent [246]. The results showed that 100% SrR was slow-released in phosphate-buffered saline (PBS) within 21 days. The nanocomposite coatings confirmed the ability of these composite coatings to enhanced bone regeneration. Boraei et al. introduced a gelatin- HNT nanocomposite scaffold into SrR via oral and systemic administration [247]. The mean pore size, porosity, and water absorption, and mechanical properties of gelatin scaffolds can be increased by adding HNTs, especially after SrR incorporation. The presence of SrR effectively improved the proliferation of the MSCs and accelerated osteogenic differentiation. In vivo studies demonstrated that the SrR released from the Gel/HNTs scaffolds enhanced bone formation and vascularization.

CHAPTER 3

HNTS AND BMP-2 AS CHEMOATTRACTANTS

3.1 Introduction

Tissue defects are repaired in a series of steps, which include infiltration of host reparative cells (e.g., osteoblast and fibroblast) into the defect site, the proliferation and activation of the cells, and the deposition of extracellular matrices (ECMs) in the defects [248-250]. The rapid recruitment of osteoblasts and bone marrow-derived stem cells to skeletal defect sites and their proliferation and differentiation is an essential prerequisite for effective bone repair [248,249]. Several previous studies have used exogenous growth factors for the recruitment of osteoblasts to the damaged site for a better therapeutic outcome [250,251]. The delivery of growth factors to the damaged site has become a widely used methodology that facilitates tissue repair by enhancing host cell recruitment, proliferation, and activation [7,252]. This approach has shown that faster recruitment of repair cells to the defect site can significantly reduce the time required for bone tissue repair and remodeling and can thus enhance bone reconstruction.

For bone repair, BMP-79 platelet-derived growth factor (PDGF) [253], transforming growth factor-b (TGF-b) [254], insulin-like growth factors, vascular endothelial growth factor [255], and bone morphogenetic protein-2 (BMP-2) [254,255] have been used to manipulate cell behavior. Chemotactic cue-induced bone repair methods can prevent the migration of other types of cells, such as epithelial cells

[13,256]. However, the utilization of chemical cues still poses several limitations, such as the high cost of growth factors, the short half-life of growth factor proteins in vivo, and the potential adverse effects of overdose events or pathological conditions [13,256].

Previous studies in our lab have shown that halloysite nanotubes (HNTs) have an osteoinductive effect and can induce pre-osteoblasts and stem cells to differentiate into osteoblasts and produce a mineralized bone matrix [256,257]. The chemotactic potential of HNTs was the objective of this study.

3.2 Material and Methods

3.2.1 Pre-osteoblast Culture

MC-3T3 E1-subclone4 preosteoblasts (ATCC) were cultured in alpha modification of Eagle's medium (α-MEM, Hyclone), which contains 10% FBS and 1% Pen/ Strep antibiotic (Life Technologies). Cells were cultured in a humidified incubator at 37 °C and 5% CO_2 level.

3.2.2 HNT Chemotactic Potential

To assess the chemotactic response of pre-osteoblasts to HNTs, the cells were prepared as in **Figure 3-1**. 24-well migration plates containing a transmembrane insert were used, with the membrane parallel to the bottom of the well. Control cultures contained pre-osteoblasts and were not exposed to either HNTs or BMP-2. The experimental groups received different concentrations of HNTs alone, BMP-2 (without HNTs) and HNTs doped with BMP-2. A 300 µl cell suspension (serum free) containing 0.5-1x106 cell/ml was placed on the top side of the transmembrane. Then, 500 µl medium with different concentrations of (1) BMP-2 (1, 5, and 10 ng/ml), (2) unloaded HNTs (50, 100, 250, and 500 µg/ml) and (3) HNTs loaded with BMP-2 (100 µg/ml HNTs with 1, 5,

and 10 ng/ml BMP-2; 250 µg/ml HNTs with 1, 5, and 10 ng/ml BMP-2) were added to the lower well of the migration plate. The plates were then incubated for 24 h at 37 °C, in 5% CO_2.

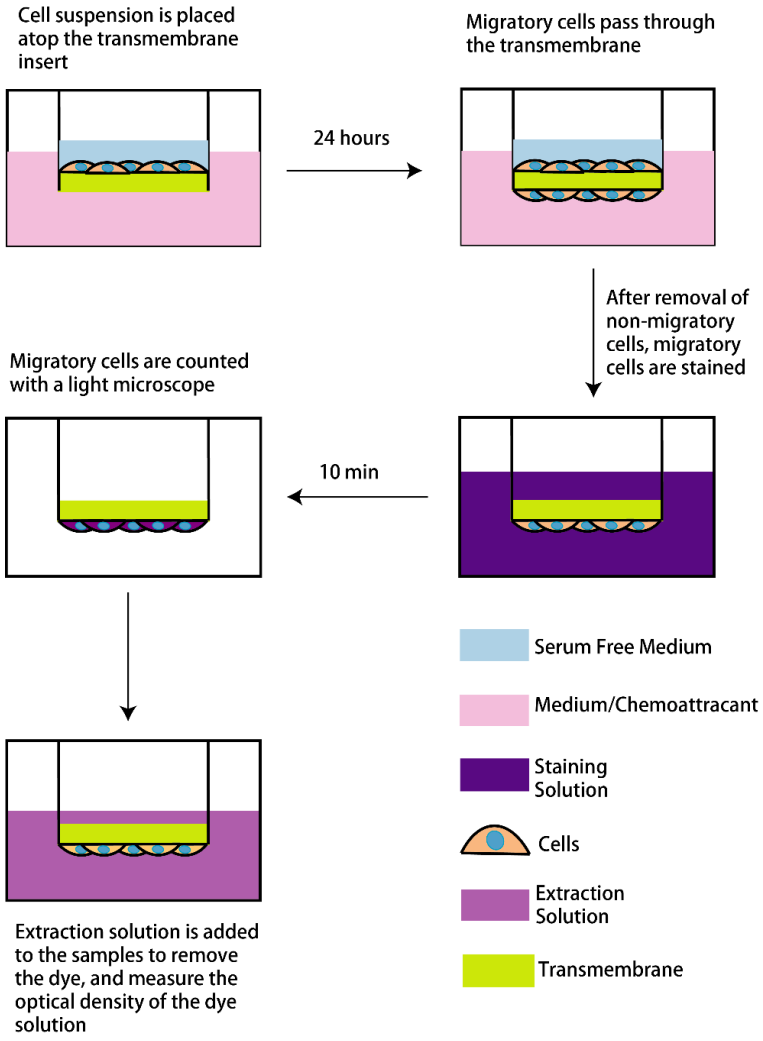

Figure 3-1: Osteoblasts MC 3T3 cell-line (ATCC) were cultured in a 25 cm^2 flask as part of a test of HNTs' chemotactic potential.

After 24 hours, cotton swabs were used to remove the cells on the top side of the transmembrane (non-migratory cells). Then, a cell staining solution was used to treat the cells that had migrated to the bottom side of the membrane (migratory cells) for 10 min at

room temperature. Next, migratory cells were imaged with a light microscope and counted with Image J. Afterwards, 200 μl of extraction solution was added to the samples to remove the dye, and the optical density of the dye solution was measured at a wavelength of 560 nm in a plate reader.

To further confirm the experimental results, the osteoblasts were stained with CSFE, the number of migrated cells observed under a fluorescent microscope, and migrated cells counted (Image J).

3.2.3 Statistical Analysis

One-way ANOVA was used to determine if the number of migratory cells was significant. Standard error was calculated and indicated as error bars in the figures.

3.3 Results

3.3.1 Histochemical Cell Staining and Cell Counts

The migration cells were stained with cell stain. **Figure 3-2** shows cells that migrated through the membrane under different concentrations (1 ng/ml, 5 ng/ml, and 10 ng/ml) of BMP-2, and different concentrations (50 μg/ml, 100 μg/ml, 250 μg/ml, 500 μg/ml) of HNTs. The 5 ng/ml BMP-2 group had the highest migration rate out of all the BMP-2 groups. In the HNTs groups, the 100 μg/ml and 250 μg/ml groups had similarly large migration rates.

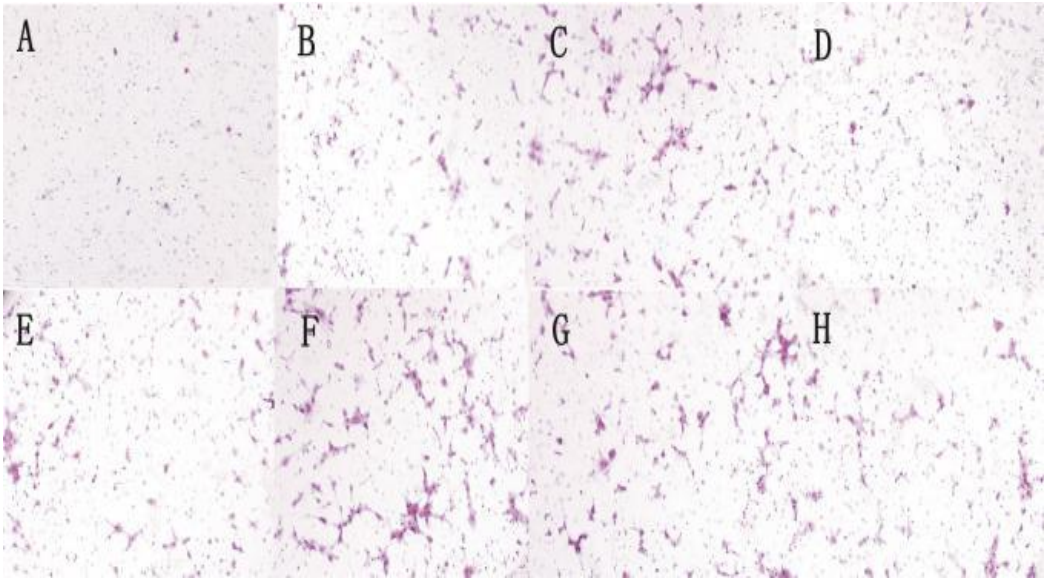

Figure 3-2: Stained cells that migrated through the transmembrane as imaged under light microscopy. (A) serum free (control), (B) 1 ng BMP-2, (C) 5 ng BMP-2, (D) 10 ng BMP-2, (E) 50 μg/ml HNTs, F. 100 μg/ml HNTs, (G) 250 μg/ml HNTs, (H) 500 μg/ml HNTs.

Then, the BMP-2 was combined with the highest migration rate group of HNTs and imaged (**Figure 3-3**). The greatest migration occurred when 100 μg/ml HNTs were combined with 10 ng/ml BMP-2 and when 250 μg/ml HNTs were combined with 10 ng/ml BMP-2. Bar graphs of the UV absorbance confirmed the results **Figure 3-4** shows the results for different concentrations of HNTs and for different concentrations of BMP-2. **Figure 3-5** shows the combined effects of HNTs mixed with BMP-2. However, in **Figure 3-2** and **Figure 3-3**, some cells were stained a darker color than the others, which means these cells had a higher UV absorbance value that may not be dependent only on the number of migrated cells, but also on the degree of staining for each cell.

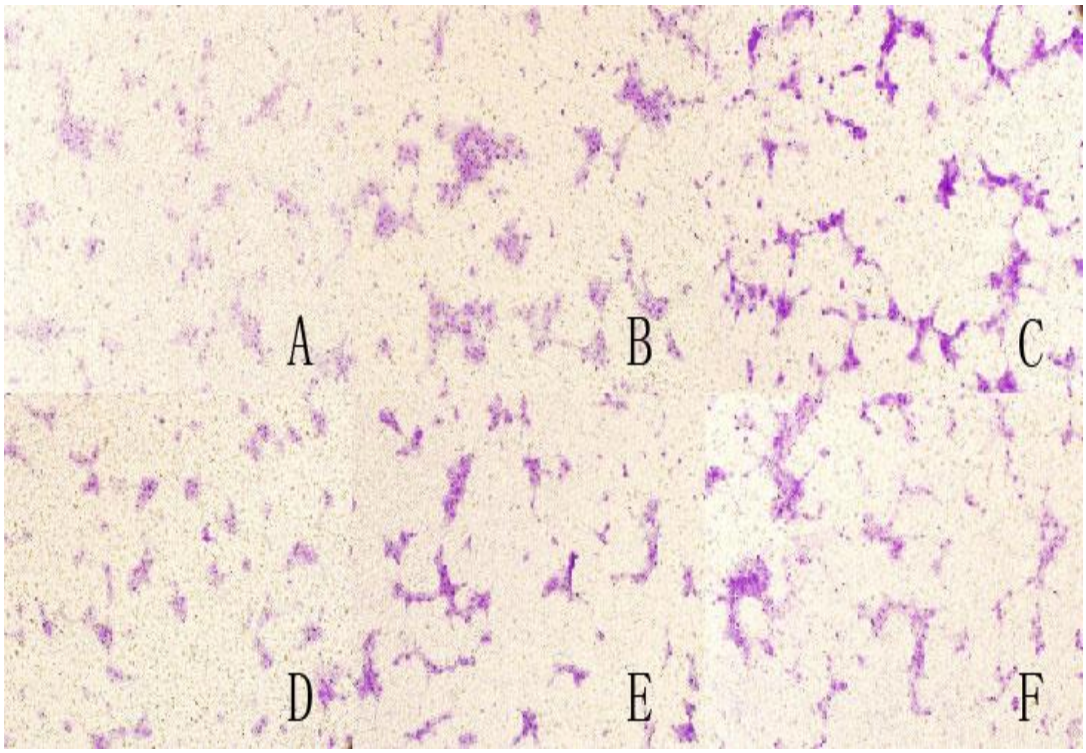

Figure 3-3: Stained migrated cells under light microscope. 1 ng BMP-2, (A, D (100 µg/ml, 250 µg/ml HNTs)), 5 ng BMP-2, (B, E (100 µg/ml, 250 µg/ml HNTs)), 10 ng BMP-2. (C, F (100 µg/ml, 250 µg/ml HNTs)).

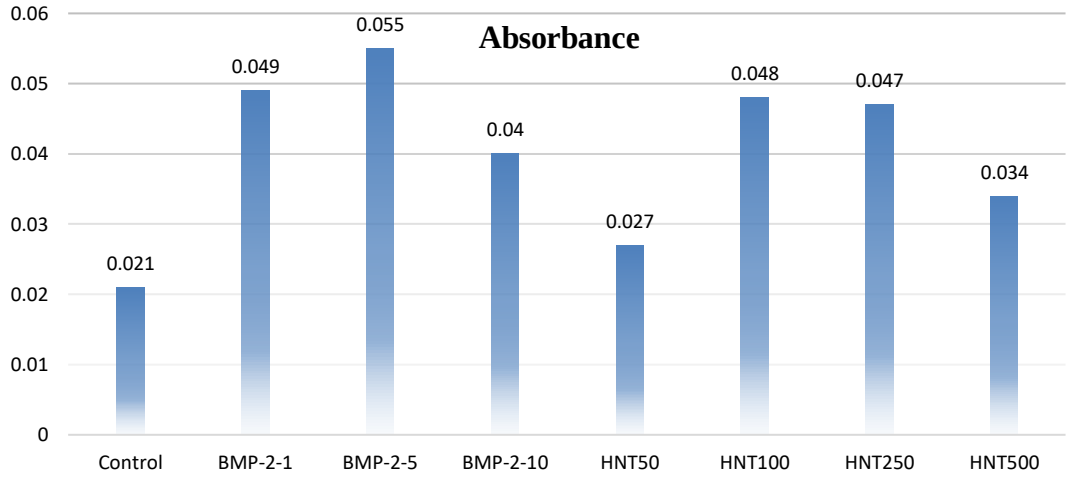

Figure 3-4: UV absorbance results among control, 1 ng BMP-2, 5 ng BMP-2, 10 ng BMP-2, 50 µg/ml HNTs, 100 µg/ml HNTs, 250 µg/ml HNTs, 500 µg/ml HNTs.

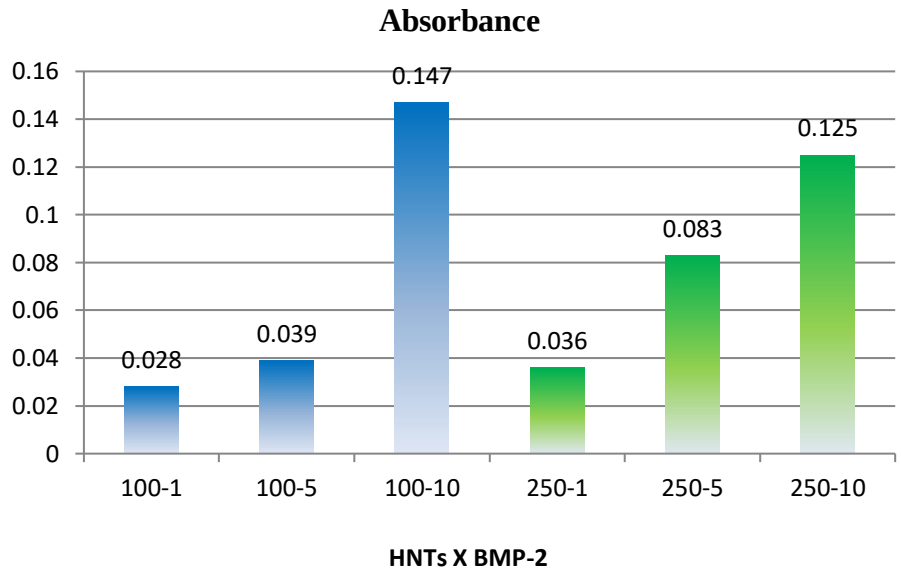

Figure 3-5: UV absorbance results between 100 µg/ml HNTs (blue) and 250 µg/ml (green) with 1 ng BMP-2, 5 ng BMP-2, and 10 ng BMP-2 separately.

To further confirm which group has a higher migration rate. The number of migrated cells in each sample was calculated. **Figure 3-6** shows the cell counting results for BMP-2 alone. The 5 ng/ml BMP-2 group shows the highest number of migrated cells out of all the BMP-2 groups. **Figure 3-7** shows the cell counting results for HNTs alone. The 250 µg/ml HNTs group shows the highest number of migrated cells.

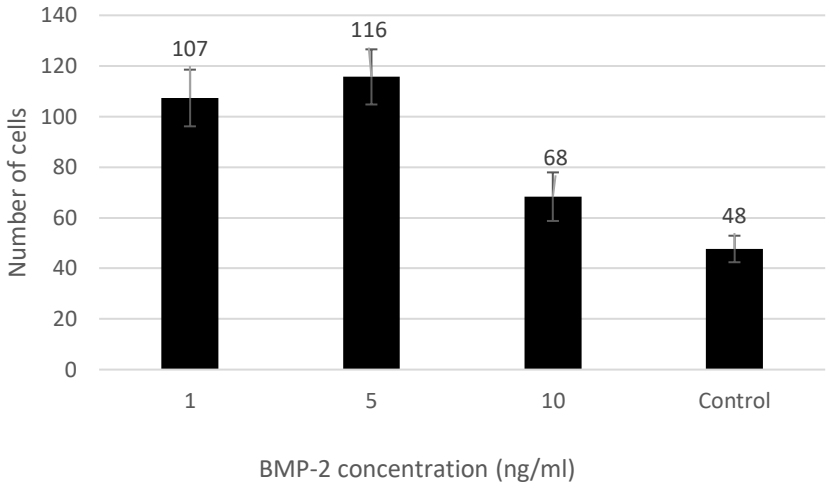

Figure 3-6: The number of migrated cells when the BMP-2 concentration are 1 ng/ml, 5 ng/ml, 10 ng/ml and 0 ng/ml (control).

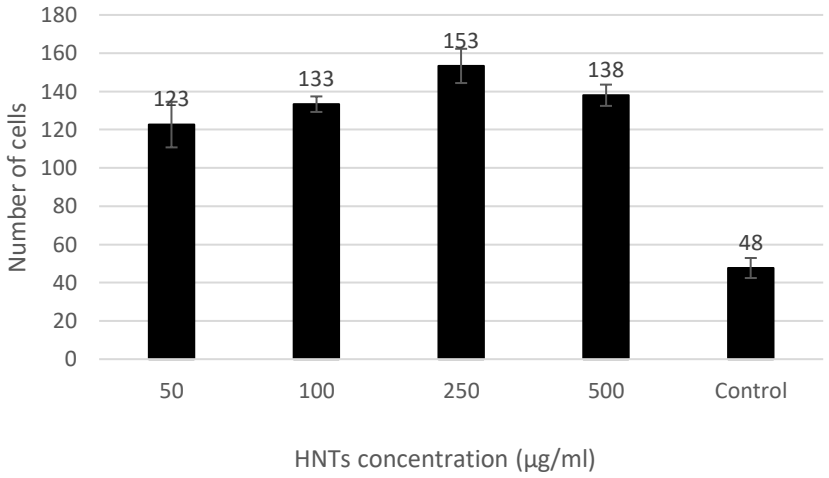

Figure 3-7: The number of migrated cells when the HNTs concentration are 50 μg/ml, 100 μg/ml, 250 μg/ml, 500 μg/ml and 0 μg/ml (control).

Among the BMP-2 with HNTs groups (**Figure 3-8**), 5 ng/ml BMP-2 with 100 μg/ml HNTs has the highest number of migrated cells, while 5 ng/ml BMP-2 with 250 μg/ml HNTs group and 10 ng/ml BMP-2 with 250 μg/ml HNTs group have the second-highest number of migrated cells. A one-way ANOVA analysis indicated a significant

contribution to the variability in migrating cell count for both BMP-2 concentration (p=0.0029) and HNT concentration (P=0.000018).

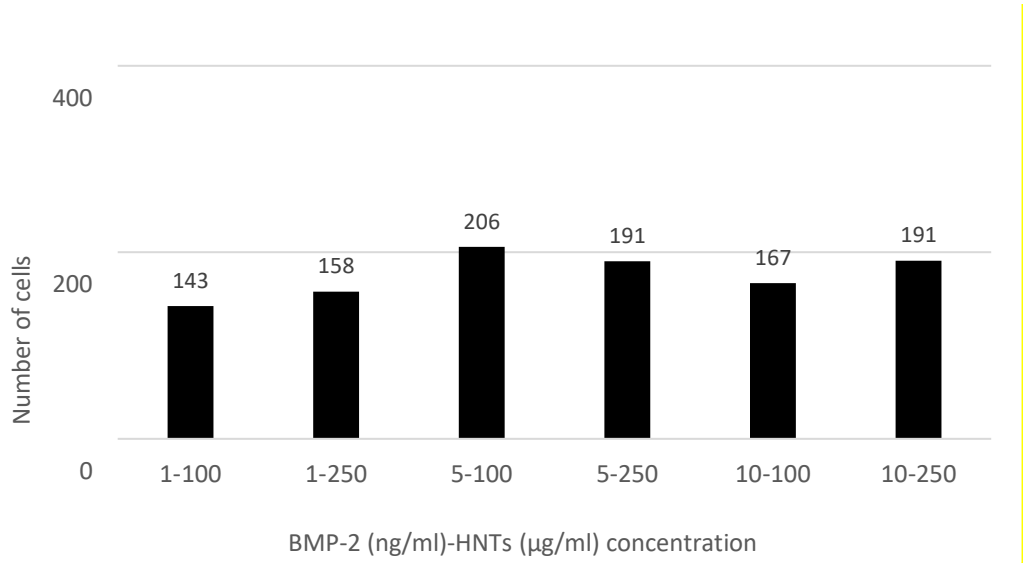

Figure 3-8: The number of migrated cells when the BMP-2 (1 ng/ml, 5 ng/ml, and 10 ng/ml) doped HNTs (100 µg/ml and 250 µg/ml).

3.3.2 Histochemical Cell Staining and Cell Counts

The osteoblasts were stained with CSFE, and the number of migrated cells was observed under a fluorescent microscope (**Figure 3-9**) and migrated cells counted **(Figure 3-10**). The 5 ng/ml BMP-2 groups had the highest number of migrated cells, and a combination of 5 ng/ml BMP-2 with 50 µg/ml HNTs had the highest number of migrated cells overall. Through one-way ANOVA analysis, a significant difference in the number of migrated cells can be observed among the different concentrations of BMP-2 doped with different concentrations of HNTs (P=0.000052). This confirmed that the combination of different concentrations of BMP-2 and HNTs is a crucial factor affecting cell migration.

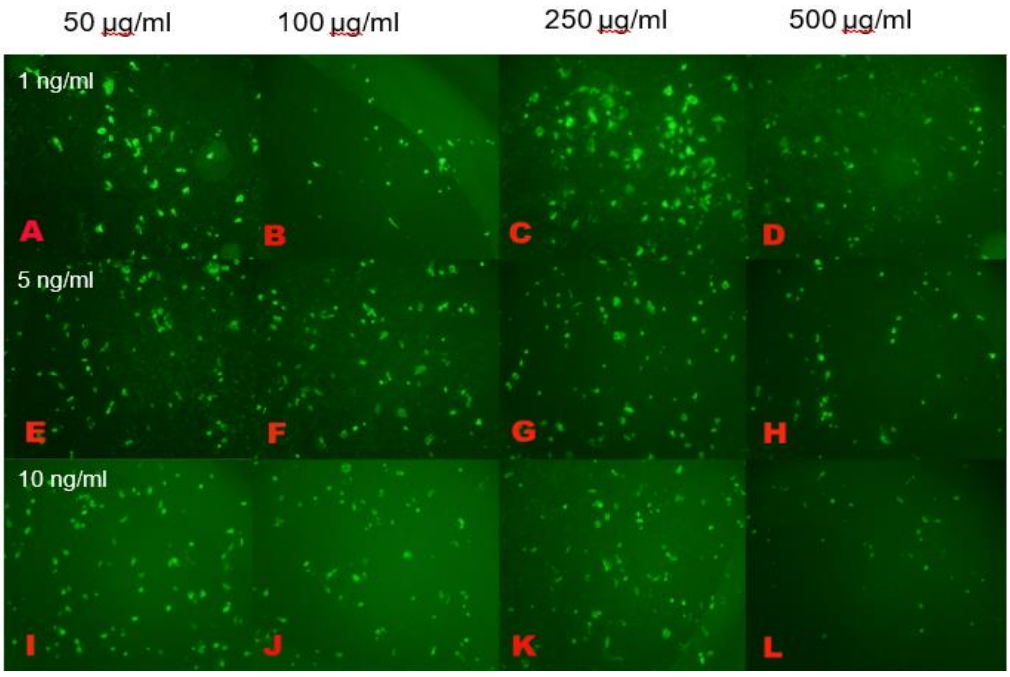

Figure 3-9: Stained migrated cells observed under epi-fluorescent microscopy.

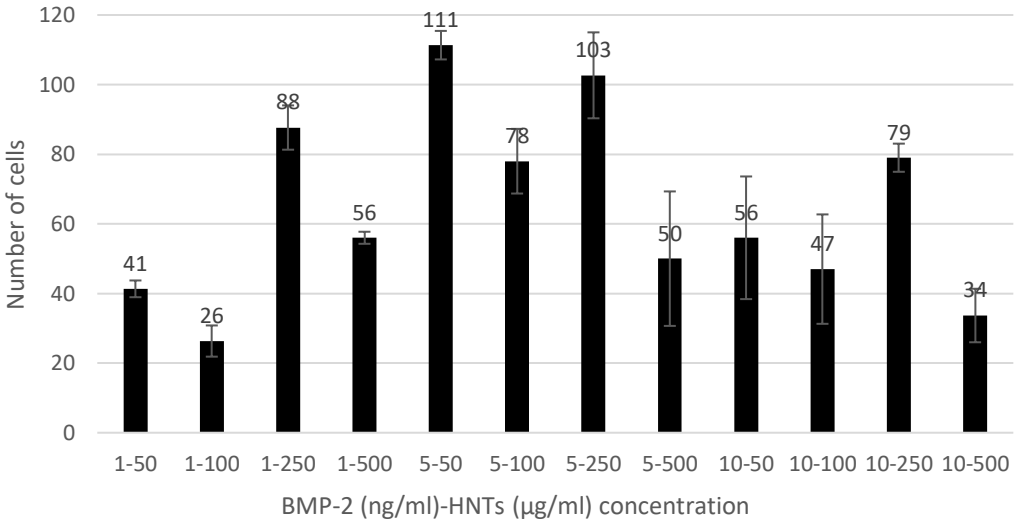

Figure 3-10: Cell counts for BMP-2 and HNTs. This figure shows the number of migrated cells when the HNTs concentration are 50 µg/ml, 100 µg/ml, 250 µg/ml, and 500 µg/ml combine with 1 ng/ml, 5 ng/ml, and 10 ng/ml BMP-2. (Error bars are standard deviations, n=3, $p<0.05$).

3.4 Conclusions

We found that HNT groups have the highest migration rate when they have a 250 μg/ml concentration. Of the BMP-2 groups, 5 ng/ml BMP-2 showed the most migrated cells. When HNTs are present in the medium, 5 ng/ml BMP-2 had the highest migration rate. Especially the group which has 5 ng/ml BMP-2 and 50 μg/ml HNTs. All these results indicate that the HNTs and HNTs doped with BMP-2 can become a new agent for use in bone regeneration.

3.5 Discussion

This study aimed to identify the optimal concentration of bioactive agents and derived composites that provide a better cell-supportive environment. Critical in our design was to determine if HNTs had a potential chemotactic effect. The preosteoblast's migration rate in response to different concentrations of HNTs, BMP-2, and HNTs combined with BMP-2. The medium we used in the transmembrane insert is a serum-free medium because the traditional medium contains growth factors and proteins that could affect cell migration. In the lower well, the only difference is the chemicals we added and their concentrations. In this way, we only need to compare the number of migratory cells; we can quickly figure out the best chemo attractive agent and the optimal concentration. However, because the method counts the migrated cells, it is essential to choose the right cell stain. The first stain that came with the migration assay kit caused uneven staining of the cells, which affected the UV absorbance and cell counting results. The second staining agent CSFE solves the problem of uneven staining, which makes our results more reliable.

The data shows that pre-osteoblasts migrated in the presence of HNTs. HNTs doped with BMP-2 showed a greater migration rate in comparison with native HNTs. The 5 ng/ml BMP-2 group showed the highest number of migrated cells out of all the BMP-2-doped HNT groups. When HNTs were present in the medium, 5 ng BMP-2 had the highest overall migration rate, particularly in the 5 ng/ml BMP-2 doped 50 μg/ml HNTs. These results indicate that HNTs and HNTs dopped with BMP-2 have potential as new scaffolding osteogenic agents for bone regeneration.

CHAPTER 4

DEVELOPMENT OF A COLLAGEN METHACRYLATE/HNT HYDROGEL COMPOSITE (COMA-HNT) SYSTEM

4.1 Introduction

Project #1 has established that HNTs and BMP-2-doped HNTs have a chemoattractive effect on pre-osteoblasts, in the case of BMP-2 doped HNTs the migration rate was even more pronounced. Osteoblasts regenerate and repair damaged bone by producing an osteoid matrix and, subsequently, mineralizing it [232]. The bone repair process was initiated by mobilizing osteoblasts to the site of the damaged bone [30]. In certain bone disorders, elderly individuals, and some osteogenic disease states, bone repair, and healing, are prolonged, and frequently completely lacking [232]. The healing process may be accelerated and enhanced through the rapid recruitment of osteoprogenitor cells and osteoblasts to the injury site. We hypothesized that HNTs and BMP-2 doped HNTs would act as a signaling mechanism and recruit osteoblasts (pre-osteoblasts, stem cells) towards doped HNTs. The recruited cells would proliferate and differentiate into osteoblasts with enhanced osteogenic gene expression. Local areas of the mineralized matrix should form following this cascade of events.

Accordingly, the principal goal of Project #2 is to develop a novel nanocomposite, composed of HNTs, strontium metalized HNTs, doped with osteogenic chemoattractants and antibiotics, all incorporated into a biocompatible hydrogel (methacrylated collagen).

Furthermore, our target was to remediate a bone disease (osteomyelitis) while simultaneously initiating bone tissue regeneration. Our focus was on creating an antimicrobial and osteogenic nanocomposite. The composite was based on a methacrylated collagen hydrogel. We used in vitro culture systems to test the following compositions added to methacrylated collagen (COMA).

1). Strontium coated HNTs (SrHNTs),

2) HNTs,

3). BMP-2-doped SrHNTs (SrB/SrHNTs+BMP-2), and

4). BMP-2-doped HNTs (HB/HNTs+BMP-2).

Osteoprogenitor cells should differentiate in-situ into osteoblasts, and with the recruited osteoblasts, actively regenerate new bone. Recent studies have indicated a critical role for various growth factors as chemoattractants (CTs) during the process of endochondral ossification and fracture repair [9-12]. In many cases, these same CTs also have a proliferative and differentiative influence on human osteoblasts.

The project produced a composite photo-crosslinked hydrogel with favorable mechanical properties and tunable bioactive properties. Furthermore, this hybrid hydrogel system can be regulated to meet specific bone and tissue regeneration applications. In this study, we determined the optimal combination between different concentrations of methacrylated collagen and cross-linking time to develop a strength-enhanced biomaterial that is both biocompatible and biodegradable. This study will help further the clinical applications of methacrylated collagen scaffolds for bone regrowth and substitution.

Methacrylated collagen was prepared in different concentrations (4 mg/ml (4%), and 8 mg/ml (8%)) and with different cross-linking time (14 min, and 18 min). The mechanical and cell properties were studied and characterized. We also tested the material properties and the tissue-forming capabilities by culturing osteoblast/pre-osteoblasts. The mechanical properties of the methacrylated collagen hydrogel should provide an idea for future research and application.

4.2 Materials and Methods

4.2.1 Prepare Sr Coated HNTs

We ordered HNTs from Sigma Aldrich and coated them with Sr by adding the HNTs and Strontium carbonate ($SrCO_3$) from Sigma Aldrich in the same quantities to distilled water as illustrated in **Figure 4-1**. A sonicator was used to evenly distribute the particles and eliminate clumps. The reaction mixture (Rm) was sonicated at regular intervals for 30 minutes for 3 days. The Rm was kept in an incubator (60 ℃). The precipitate obtained was washed in citric acid (pH=4) to remove excess CO_3^{2-} ions and water-washed 3 times. The precipitate was collected and dried.

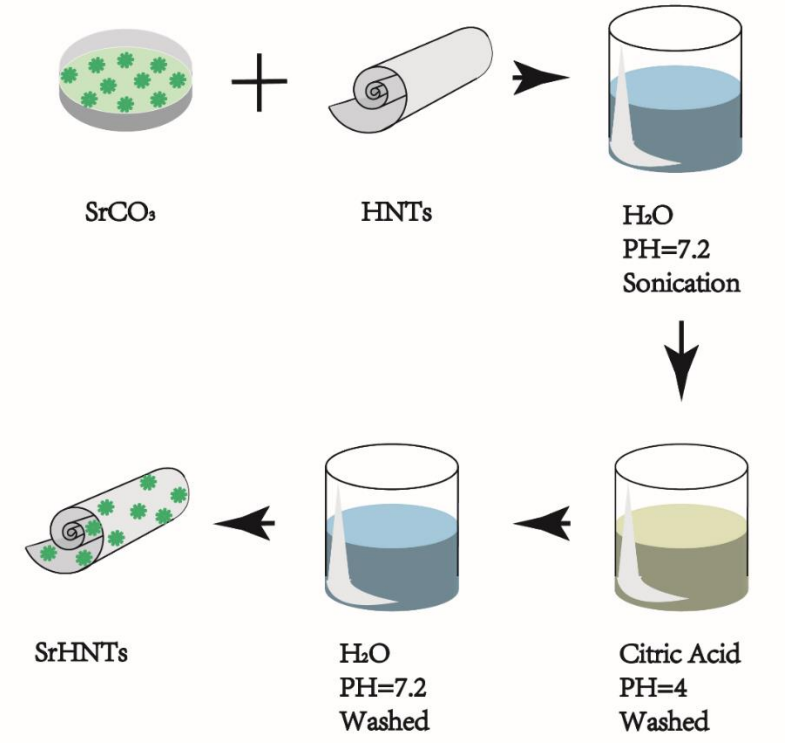

Figure 4-1: Schematic representation of the process to make Green SrHNT.

4.2.2 In Vitro Degradation Assay

An in vitro degradation assay was used to study the weight loss after dehydration of the samples (n = 3, **Figure 4-2**). All samples were prepared in a 1.5 ml tube. Then the solution was transferred to a silicon mold, the length, width, and depth of which was 15×5×3.5 mm. The set volume for each sample was 250 µl. All samples were set in the mold for 14, and 18 minutes under UV light. The samples were pre-incubated in DPBS at 37 ℃ for 1 day. Then the samples were collected after 1, 7, and 14 days. DPBS was changed every 3 days. After each specific time point, the samples were rinsed in DPBS, weighed, and lyophilized using a freeze-dryer for 24 hours. The weight of the dried samples was determined after lyophilization. The percent degradation for each sample was calculated as the weight loss from the sample's initial dry weight.

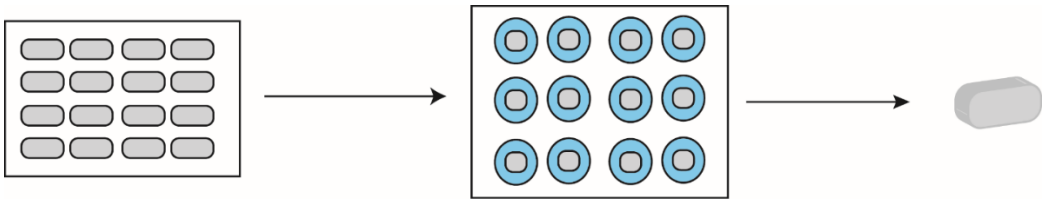

Figure 4-2: Degradation procedure.

4.2.3 Scanning Electron Microscopy (SEM)

The surface topographies of all samples were examined in a dry condition after the cross-linking process. A cross-linked group of samples was prepared in a 1.5 ml tube. Then, the solution was transferred to a small pipe sealed on one side, the diameter of which is 6.25 mm. 100 µl total volume was removed from all samples. All samples were set in a pipe for 14, and 18 minutes under UV light. Dry samples were pre-frozen at −20 ℃ for 24 hours and lyophilized using a freeze-dryer for 1 day. All samples were coated with gold. The surface topography of all samples was imaged by SEM (Hitachi S4800).

4.2.4 Contact Angle

Samples were prepared in a 1.5 ml tube. Then, the hot solution was poured onto a piece of glass. The samples were set on the glass for 24 hours at 21 ℃. Hydrophilic properties of the developed methacrylated collagen sample were determined by water contact angle measurement using the static Sessile Drop technique. Contact angles were measured at 20 seconds and after 80 seconds to observe any changes in the droplets' shape. The contact angle of the sample was measured using a contact angle system OCA by Data Physics (San Jose, CA). The average of all measured samples was reported with its standard error bar.

4.2.5 Cell Proliferation

Cells were seeded on pretreated scaffolds at a concentration of 1×10^5 cells/ml. The culture media was changed every 3 days. Cell proliferation was assessed through a cell proliferation assay. The proliferation data were collected on days 1, 7, 14, and 21 days after the initial cell seeding.

4.2.6 Cell Differentiation

An Osteocalcin Quantikine ELISA kit (R&D system) was employed to measure osteocalcin (OC) as a marker for osteogenic differentiation. All samples were assessed for each condition. After cell culture, samples were rinsed with PBS, incubated with 0.2 mL of acetic acid (10% by volume) for 1 h at 37 ℃, and lyophilized overnight. The manufacturer's sample buffer was used to resuspend the lyophilized protein before transfer to the ELISA plate. ELISA plates were processed according to the manufacturer's protocols. A standard curve was generated to determine osteocalcin concentration. Sample measurements with background subtracted were used as controls. Controls were COMA gel samples incubated with cells in cell culture medium for 21 days (with medium changes) and then assayed by ELISA.

4.2.7 Statistical Analysis

One-way ANOVA was used to determine if the level of degradation, proliferation, and differentiation was significant. Standard error was calculated and indicated as error bars in the figures.

4.3 Results

4.3.1 In Vitro Degradation Assay

In the regeneration of bone, the degradation rate of the scaffold needs to match the regeneration rate of the bone. The degradation of HNTs/COMA hydrogels was performed in PBS to mimic conditions in vivo (**Figure 4-3**). The rate of hydrogel mass loss showed a significant increase on day 7. The remaining mass of the HNTs/COMA hydrogels was significantly reduced after being immersed in PBS for 14 days.

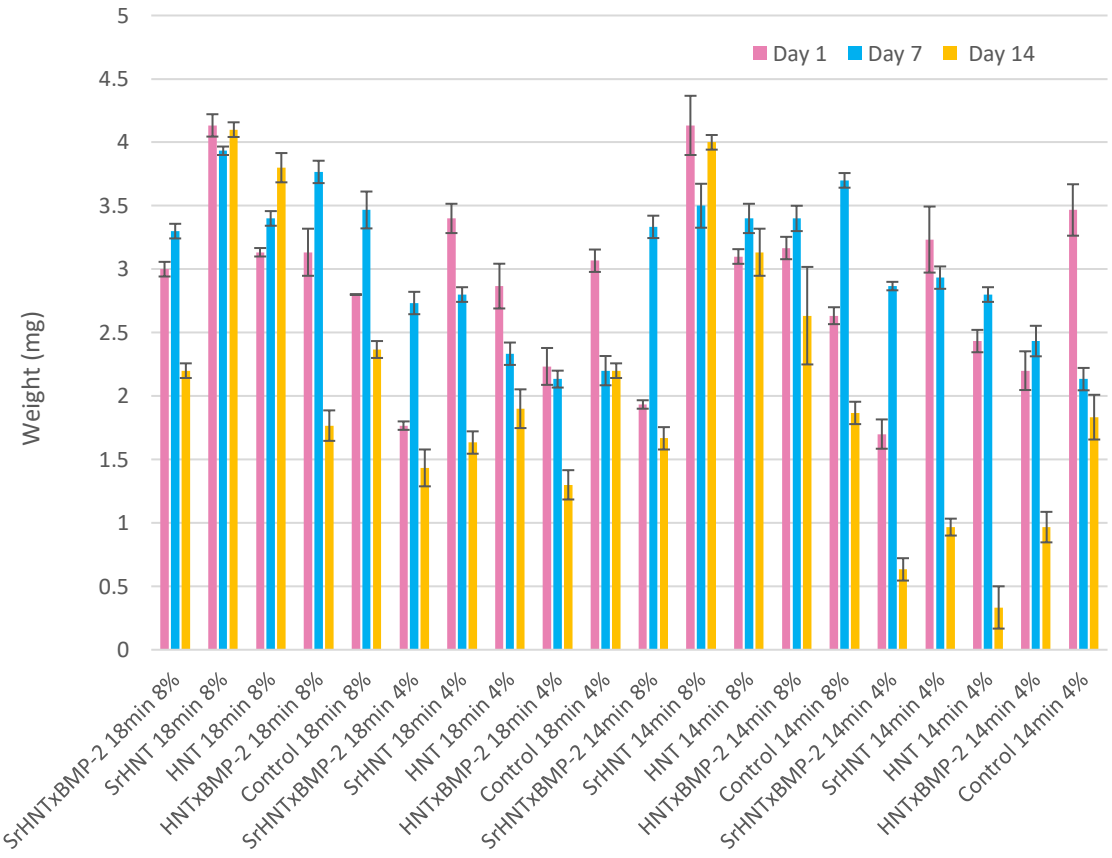

Figure 4-3: In vitro degradation results. (n=3, $p<0.05$).

In this study, the 4% COMA group degraded faster than the 8% group. In the 4% COMA group, samples crosslinked for 14 min degraded faster than samples crosslinked for 18 min. The 8% CoMA group exhibited minimal weight loss. The addition of HNTs

in 8% COMA groups showed a slight increase in the degradation ratios while the 4% COMA groups did not show a similar increase in the degradation ratios. As the amount of HNTs was increased the degradation ratios tended to decrease, though with no significant differences. A possible reason could be that the incorporation of HNTs may affect the network of COMA, though the impact on the degradation was limited. The groups incorporating HNTs, and BMP-2 have a slightly higher degradation ratio than other samples in their groups.

4.3.2 SEM

The COMA gel was imaged at two concentrations and two crosslinking times (four combinations). The SEM images were acquired to study the surface features of each condition. Samples were pretreated by lyophilization and coated with 6 nm gold.

Figure 4-4 shows SEM images for 8% COMA gel crosslinked for 18 min. The 8% 18 min COMA gel group, gel with additional SrHNTs and BMP-2, and HNTs and BMP-2 showed clear collagen fiber on the surface. The thickness of the collagen fibers on SrHNTs and BMP-2, and HNTs and BMP-2 are approximately the same. Instead, the SrHNTs, HNTs, and control (COMA) hydrogel have a smooth exterior. The HNTs sample has the smoothest surface and some noticeable cracks.

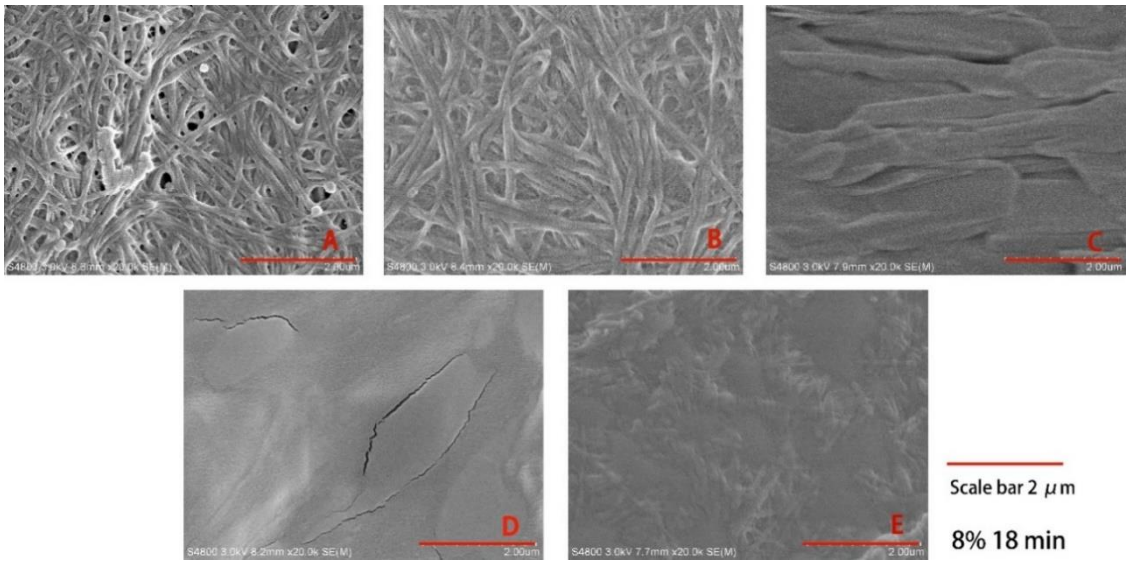

Figure 4-4: SEM results for 8% COMA gel that was crosslinked for 18 min. (A) SrHNTS+BMP-2, (B) HNTs+BMP-2, (C) SrHNTs, (D) HNTs, (E) COMA.

In the 8% 14 min COMA gel group (**Figure 4-5**), gel with additional SrHNTs and BMP-2, SrHNTs, and HNTs showed truly clear collagen fiber on the surface. Compared to SrHNTs and BMP-2, and SrHNTs, gel with HNTs has less fiber and a smoother surface. The thickness of the collagen fibers on SrHNTs and BMP-2 is thicker than the fiber on SrHNTs. Instead, the HNTs and BMP-2, and control hydrogel have a smooth exterior. The HNTs and BMP-2 sample has barely any fibers.

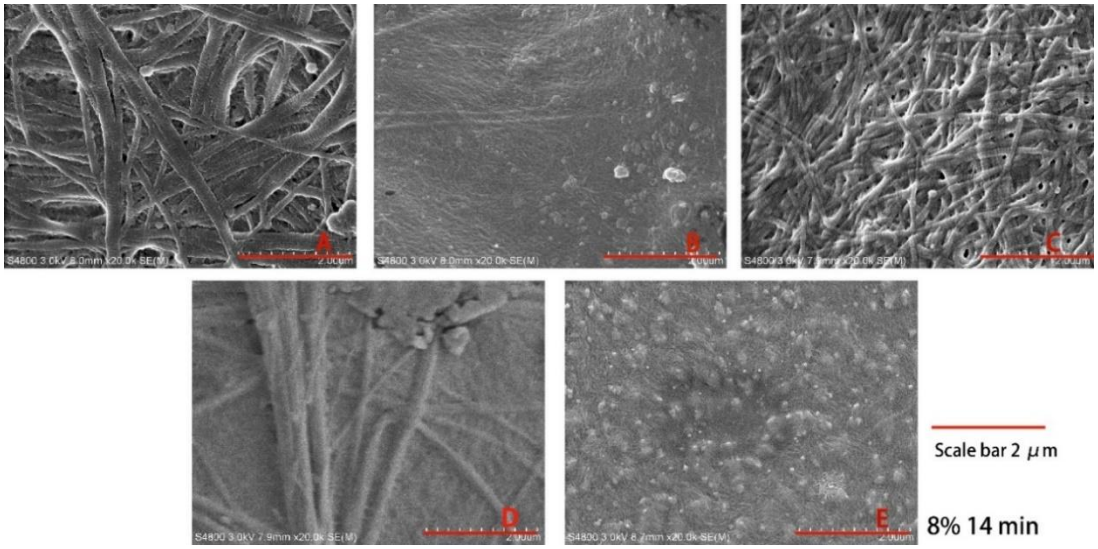

Figure 4-5: SEM results for 8% COMA gel that crosslinked for 14 min. (A) SrHNTS+BMP-2, (B) HNTs+BMP-2, (C) SrHNTs, (D) HNTs, (E) COMA.

In the 4% 18 min COMA gel group (**Figure 4-6**), all gels have a smooth exterior. Gels with additional SrHNTs showed obvious collagen fibers on the surface. Compared to SrHNTs, gel with SrHNTs and BMP-2, HNTs, and control has less fiber and a smoother surface. The thicknesses of the collagen fibers on all the samples are approximately the same.

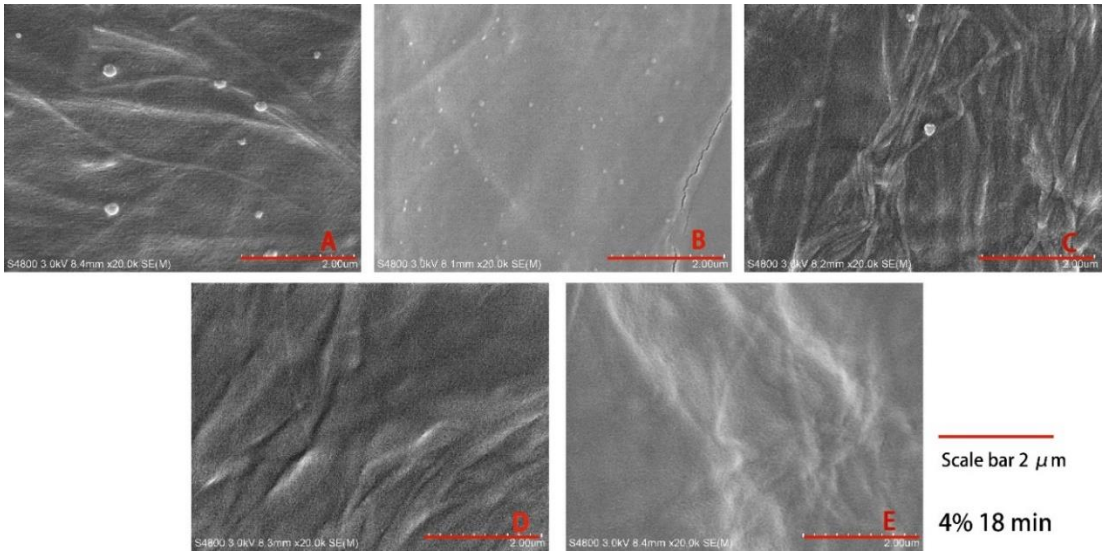

Figure 4-6: SEM results for 4% COMA gel that are crosslinked for 18 min. (A) SrHNTS+BMP-2, (B) HNTs+BMP-2, (C) SrHNTs, (D) HNTs, (E) COMA.

In the 4% 14 min COMA gel group (**Figure 4-7**), all gels have clear collagen fiber on the surface. COMA gel has less fiber and a smoother surface. The thicknesses of the collagen fibers on all the samples are approximately the same. The SrHNTs and BMP-2, and SrHNTs hydrogel have more collagen fiber than the other samples.

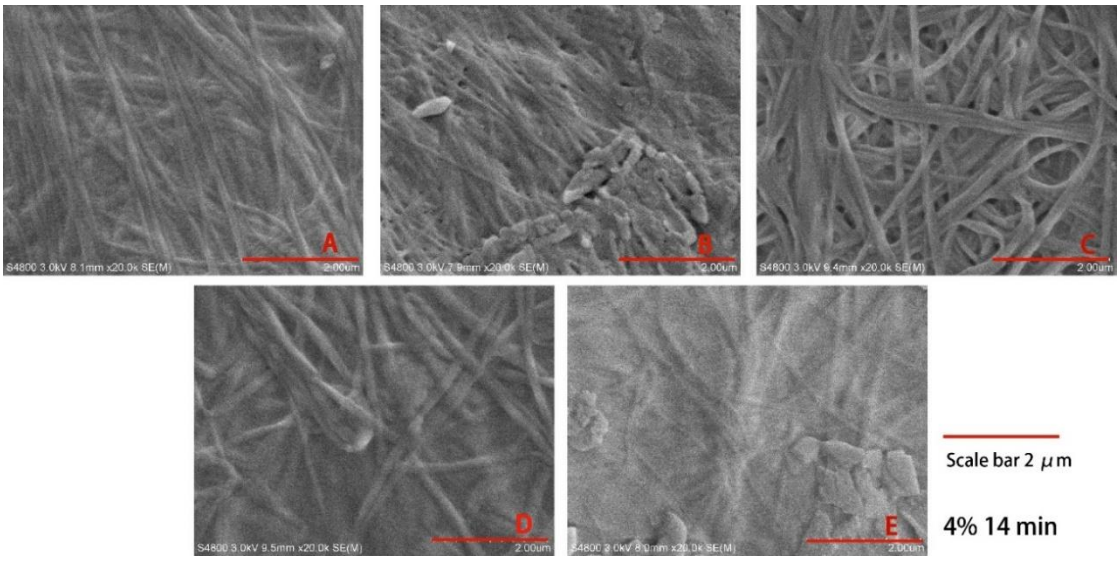

Figure 4-7: SEM results for 4% COMA gel that was crosslinked for 14 min. (A) SrHNTS+BMP-2, (B) HNTs+BMP-2, (C) SrHNTs, (D) HNTs, (E) COMA.

When all the combinations are compared, 4% 14 min COMA gels generally have a rougher exterior, while 4% 18 min COMA gels have a smoother exterior. Samples containing SrHNTs and HNTs are rougher than the control.

4.3.3 Contact Angle

Biomaterials for implanting the bone should evoke favorable cellular responses in cell attachment, adhesion, proliferation, and differentiation. In particular, the initial phase of cell/material interactions and the quality will influence the cell's capacity to proliferate and differentiate. Generally, when the contact angle decreased, the cell adhesion increased. In this study, type I collagen was used because it facilitates cell attachment and enhances surface bioactivity. In this study, the contact angle was measured at 20 seconds and 80 seconds to determine if there was a change in the droplets' shape.

In the SrHNTs and BMP-2 groups (**Figure 4-8**), 8% COMA hydrogels had a larger contact angle than 4% COMA hydrogels, which indicated 8% COMA hydrogels were more hydrophobic than 4% COMA hydrogels. When compared to the 8% and 4%

groups, COMA hydrogels crosslinked for 14 min had smaller contact angel than COMA hydrogels crosslinked for 18 min, which indicated COMA hydrogels crosslinked for 14 min were more hydrophilic than the 18 min samples. All samples' contact angles reduced as time went up.

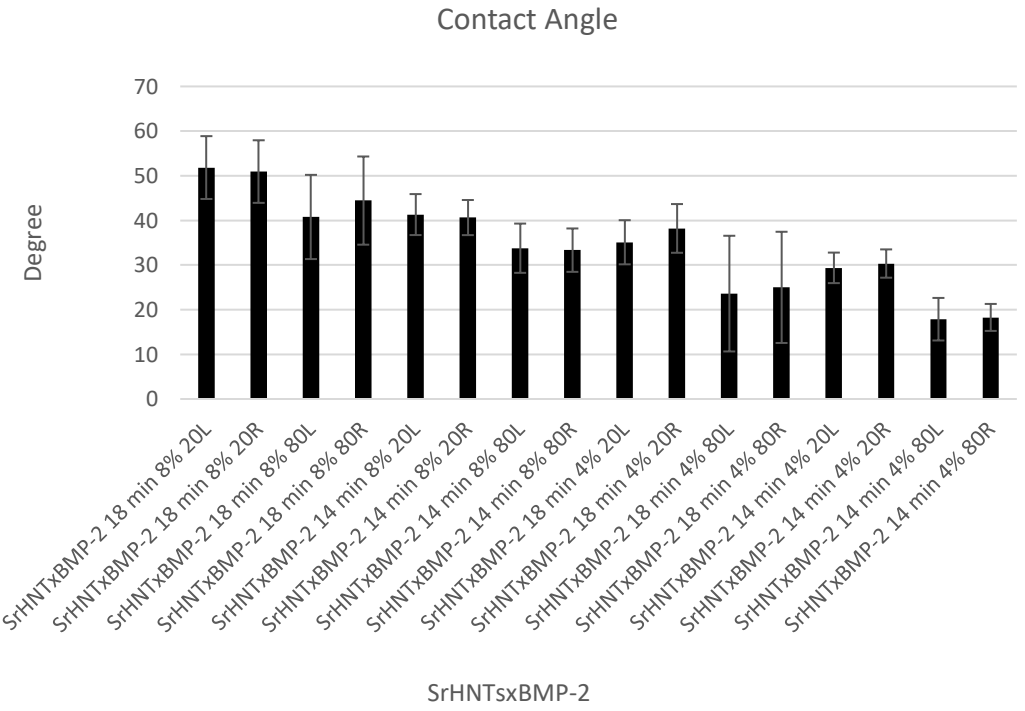

Figure 4-8: SrHNTxBMP-2 contact angle results. (Error bars are standard deviations, n=3)

In the HNTs and BMP-2 groups (**Figure 4-9**), 8% COMA hydrogels had a larger contact angle than the 4% COMA hydrogels, except for the 4% 18 min COMA hydrogel at 20 seconds, which indicated 8% COMA hydrogels were generally more hydrophobic than 4% COMA hydrogels. Compared to the 8% and 4% groups, COMA hydrogels crosslinked for 14 min had smaller contact angles than COMA hydrogels crosslinked for 18 min, which indicated COMA hydrogels that crosslinked for 14 min were more

hydrophilic than 18 min samples. All samples' contact angle decreased as time after drop placement increased.

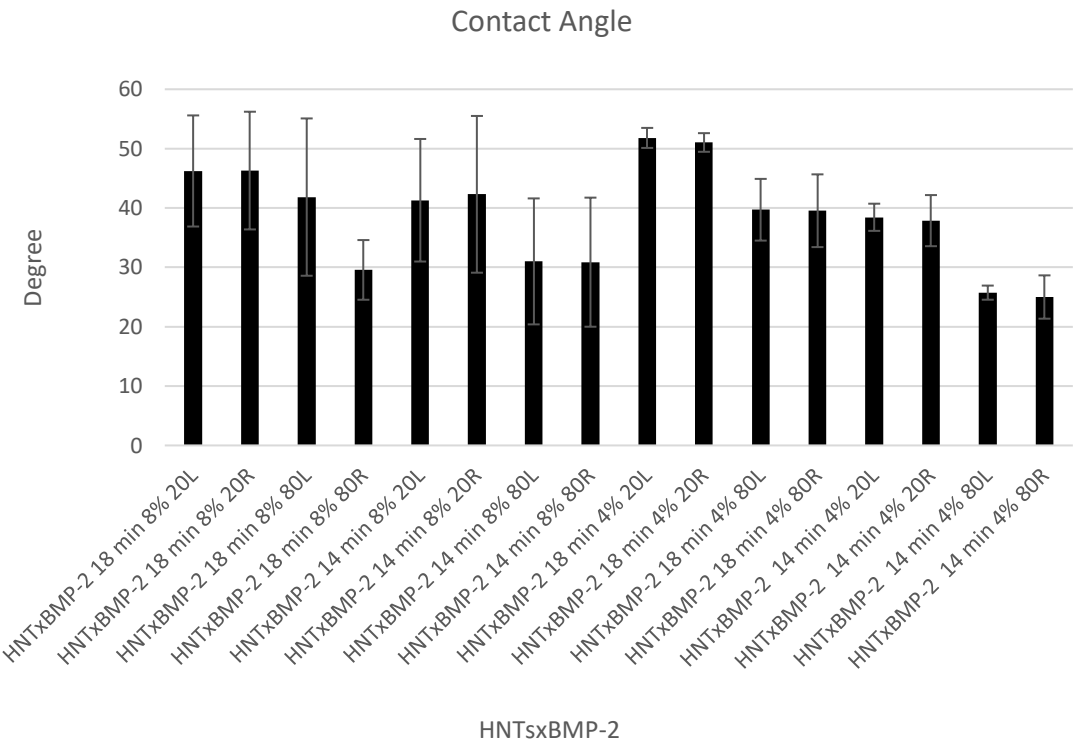

Figure 4-9: HNTxBMP-2 contact angle results. (Error bars are standard deviations, n=3)

In the SrHNTs groups (**Figure 4-10**), 8% COMA hydrogels had a larger contact angle than 4% COMA hydrogels, which indicated 8% COMA hydrogels were more hydrophobic than 4% COMA hydrogels. Within the 8% and 4% groups, COMA hydrogels that crosslinked for 14 min had smaller contact angel than COMA hydrogels that crosslinked for 18 min, which indicated COMA hydrogels that crosslinked for 14 min were more hydrophilic than 18 min samples. All samples' contact angle reduced as time went up.

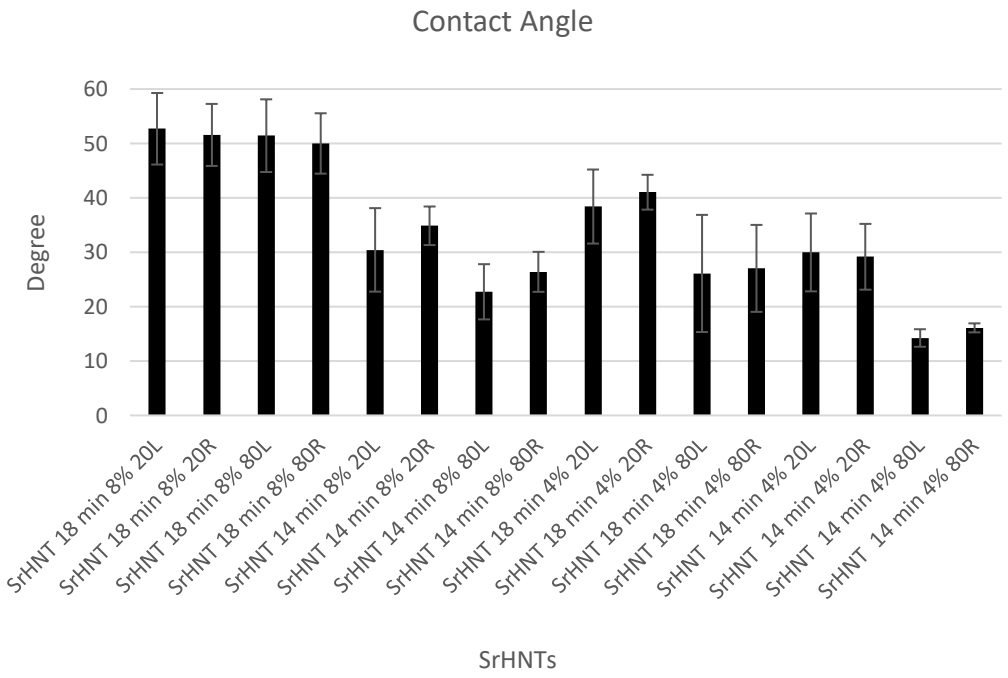

Figure 4-10: SrHNT contact angle results. (Error bars are standard deviations, n=3)

In the HNTs groups (**Figure 4-11**), 8% COMA hydrogels had a larger contact angle than 4% COMA hydrogels, which indicated 8% COMA hydrogels were more hydrophobic than 4% COMA hydrogels. Within the 8% and 4% groups, COMA hydrogels that crosslinked for 14 min had smaller contact angel than COMA hydrogels that crosslinked for 18 min, which indicated COMA hydrogels that crosslinked for 14 min were more hydrophilic than 18 min samples. All samples' contact angle reduced as time went up.

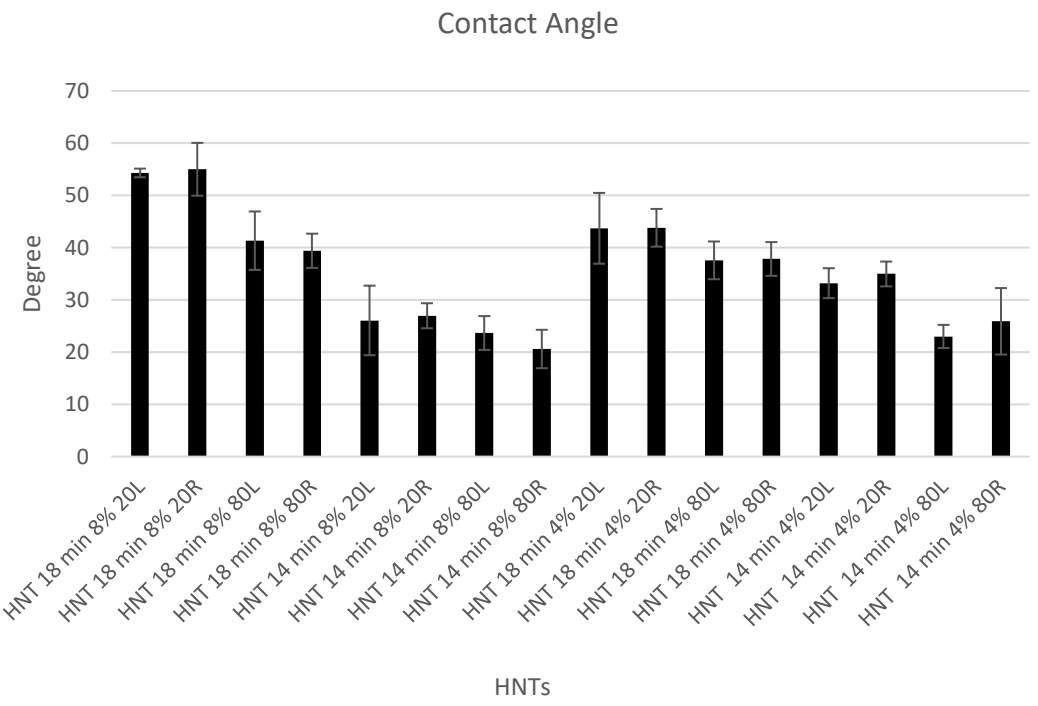

Figure 4-11: HNT contact angle results. (Error bars are standard deviations, n=3)

In the control groups (**Figure 4-12**), 8% COMA hydrogels had a larger contact angle than 4% COMA hydrogels, except the 8% 14 min COMA hydrogels. Within the 8% and 4% groups, COMA hydrogels that crosslinked for 14 min had smaller contact angel than COMA hydrogels that crosslinked for 18 min, which indicated COMA hydrogels that crosslinked for 14 min were more hydrophilic than 18 min samples. Within the 4% groups, no significant difference was found in contact angle between the samples that crosslinked for 14 min and 18 min. All samples' contact angles decreased with time.

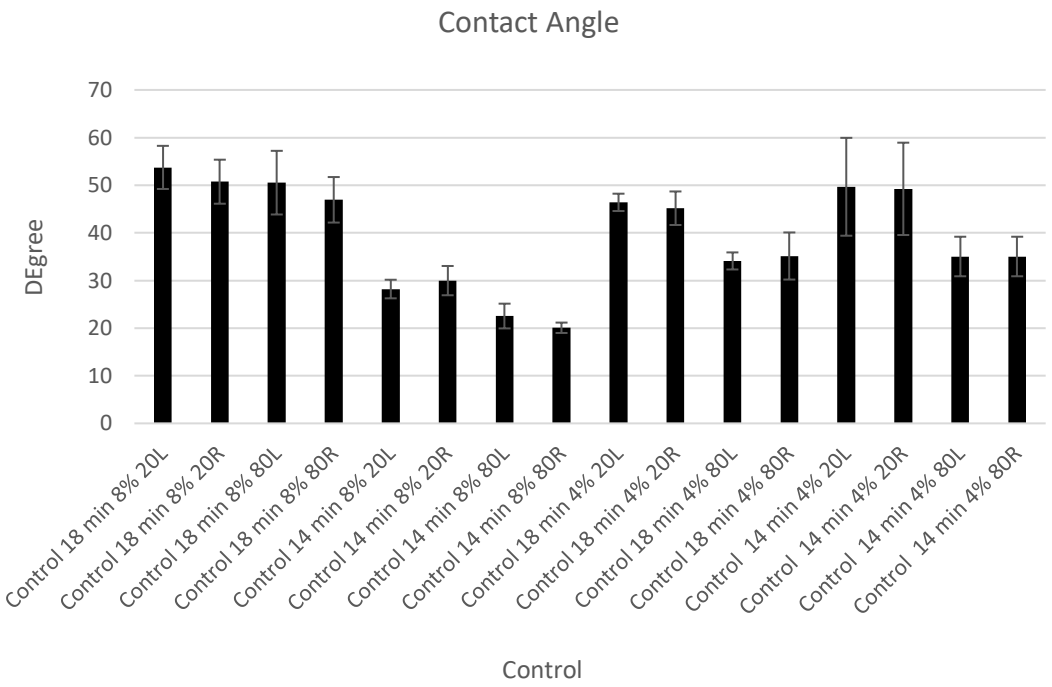

Figure 4-12: Control contact angle results. (Error bars are standard deviations, n=3)

Figure 4-13 shows contact angles for all the cases studied. The SrHNTs 4% 14 min COMA hydrogel had the smallest contact angle at 80 seconds. SrHNTs and BMP-2 4% 14 min COMA hydrogel had the second smallest contact angle at 80 seconds. Overall, the hydrogels with a proper percent of COMA gel and crosslinking time tended to have improved hydrophilic properties, indicating the potential to improve bone regeneration in vivo.

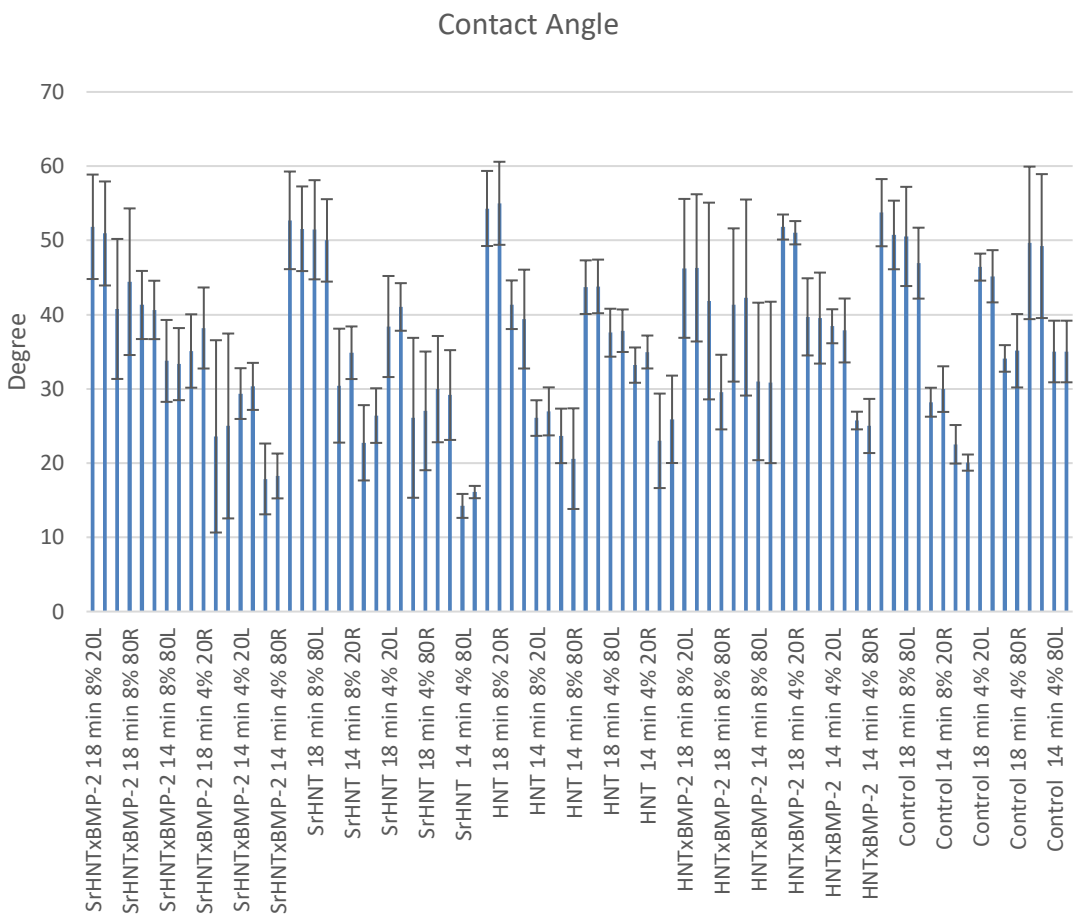

Figure 4-13: Contact angle results. (Error bars are standard deviations, n=3, $p<0.05$)

4.3.4 Cell Proliferation

The MTS results showed no differences among each group on day 7 (**Figure 4-14**) except for 8% 18 min crosslinking groups, which were significantly higher than the other groups on day 7. On day 14, the cells treated with HNTs/COMA 4% hydrogels presented a higher proliferation rate than the 8% groups, indicating that a specific concentration of COMA may benefit the proliferation of preosteoblasts at an early stage. On day 21, the group treated with SrHNTs, and HNTs COMA 8% 14 min hydrogel showed a lower proliferation rate than other groups with HNTs. On day 28, all samples showed a similar proliferation rate.

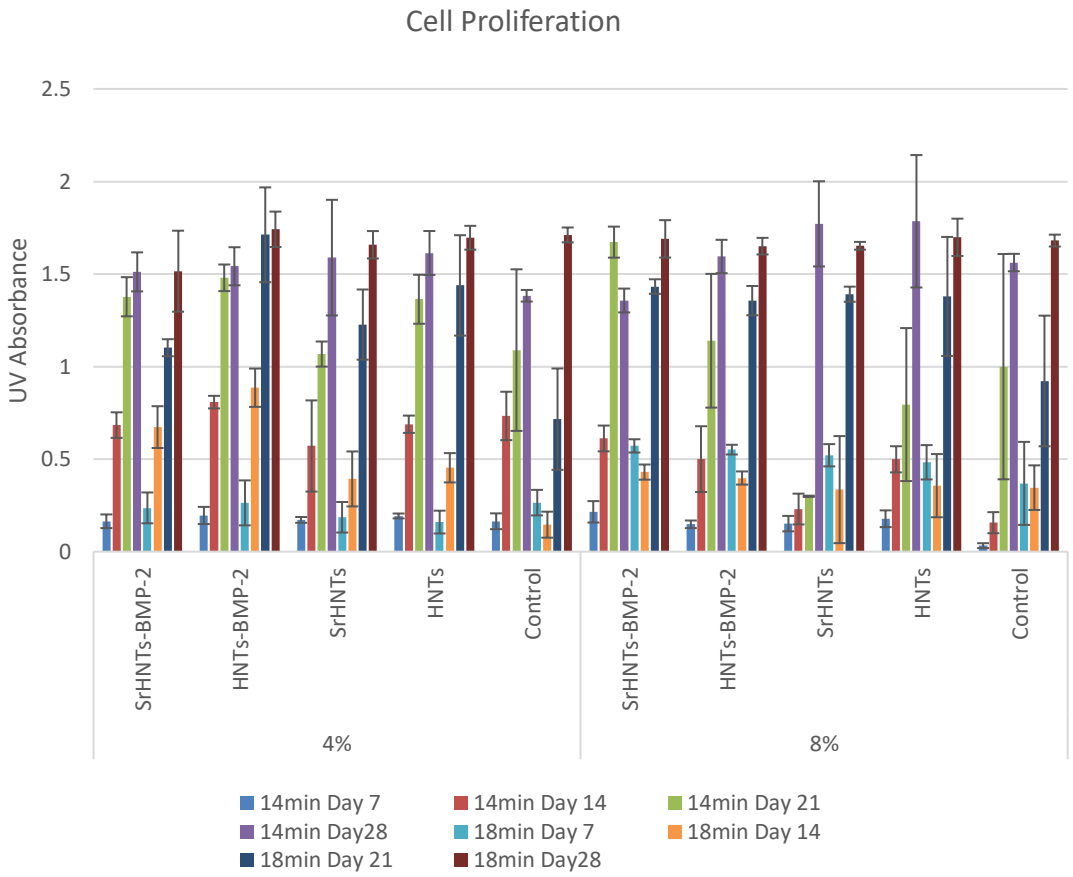

Figure 4-14: Cell proliferation results. (Error bars are standard deviations, n=3, P>0.05)

4.3.5 Cell Differentiation

Osteocalcin is another indicator of osteogenic differentiation since it is secreted only by osteoblasts. Osteocalcin was quantified on day 7, day 14, and day 21. The osteocalcin results showed no differences among each group on day 7 (**Figure 4-15**). On day 14, the cells treated with SrHNTs and BMP-2 COMA 18 min hydrogels and HNTs and BMP-2 COMA 4% 18 min hydrogel presented a higher differentiation rate than other groups. On day 21, the cells treated with SrHNTs, and BMP-2 COMA 4% 18 min hydrogels presented the highest differentiation rate compared to other groups. Therefore,

results demonstrated that SrHNTs and BMP-2 COMA 4% 18 min hydrogels enhanced preosteoblasts differentiation and osteogenesis in vitro.

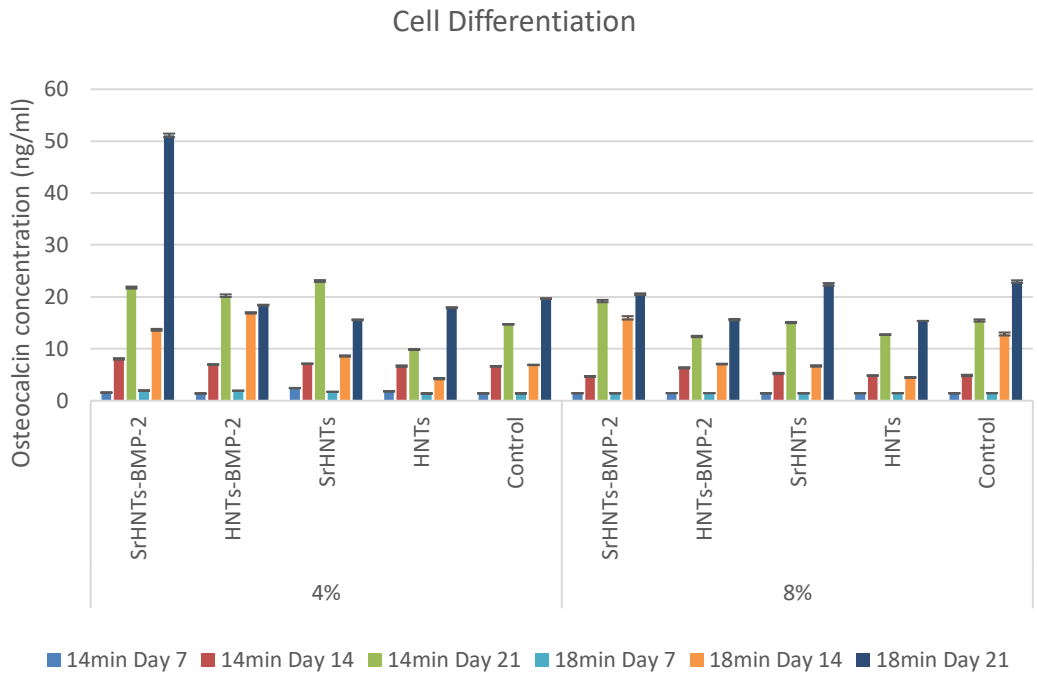

Figure 4-15: Cell differentiation results. (Error bars are standard deviations, n=3)

4.4 Conclusions

In the degradation study, the 4% COMA group degraded faster than the 8% group. In the 4% COMA group, samples crosslinked for 14 min degraded faster than samples crosslinked for 18 min. The contact angel results show that SrHNTs 4% 14 min COMA hydrogel had the smallest contact angel at 80 seconds. SrHNTs and BMP-2 4% 14 min COMA hydrogel had the second smallest contact angle at 80 seconds. All samples showed a similar proliferation rate. The differentiation results demonstrated that SrHNTs and BMP-2 COMA 4% 18 min-crosslinked hydrogels enhanced preosteoblasts differentiation and osteogenesis in vitro.

4.5 Discussion

The objective of this project is to determine the optimal combination of different concentrations of methacrylated collagen, HNTs/ SrHNTs, BMP-2 doped HNT/SrHNT, and cross-linking time for use in 3D bioprinting. From project #1 we found 5 ng/ml BMP-2 doped 50 µg/ml HNTs and 250 µg/ml HNTs have the highest and second-highest migration rate. Our lab's previous research found Sr helps bone repair. We added SrHNTs to see if the same amount of SrHNTs works better than the HNTs in the COMA gel composite system.

The objective of the degradation study was to determine whether the concentration or crosslinking time of COMA gel affected its degradation. The degradation test gives us a general idea of how long our material could last in an animal body. Our research found degradation time increased if COMA gel concentration increased. Our research also found when COMA gel crosslinking time increased, degradation time increased. Besides UV light crosslinking, we also can add genipin which is a naturally occurring cross-linking agent that has significantly low toxicity to increase crosslinking levels. This is another way to increase degradation time. However, this does not mean the longer the degradation time, the better. Its duration depends on how quickly the patient's wound is repaired. Above all, we can choose the most suitable cross-linking method according to our specific needs.

The SEM results showed us the surface characterization of our COMA gel. The samples' temperature went up before UV crosslink, after crosslinking the COMA gel had a white color. They had more collagen fibers forming than the gel kept at a low temperature. The samples kept at a low temperature after crosslinking had clear color.

Biomaterials for implantation in bones should evoke favorable cellular responses in terms of cell attachment, adhesion, proliferation, and differentiation. In particular, the initial phase of cell/material interactions and the quality of this stage will influence the cell's capacity to proliferate and differentiate. Generally, when the contact angle decreased, the cell adhesion increased. In this study, type I collagen was used due to its excellent properties that facilitate cell attachment as well as enhance surface bioactivity. In the contact angle test, we found most of our samples had a small contact angle after 80s. It is difficult to measure the contact angle over a longer period.

Since the proliferation test results showed no significant difference, the ingredients we added did not inhibit cell proliferation. However, the differentiation test screen out SrHNTs+BMP-2 composited with 4% 18min COMA gel had the highest differentiation rate. This indicated SrHNTs+BMP-2 composited with 4% 18min COMA gel repair bone defects faster than the rest of the samples.

CHAPTER 5

3D BONE CELL CULTURE - ASSESSMENT OF COMA-HNT HYDROGEL COMPOSITE'S ANTI-INFECTIVE/ OSTEOGENIC IN VITRO POTENTIAL

5.1 Introduction

In project #2, we screen out the optimal nanocomposite system for bone repair and regeneration. However, hydrogels do not have a strong mechanical property. Repairing bone damage requires the use of materials with high mechanical strength to print the scaffold. Then we use our nanocomposite materials to modify the surface of the scaffold to make cell-affinity of the scaffold better. Meanwhile, the scaffold material must also be degradable. Since bone repair takes several months, when choosing a scaffold material, the material cannot degrade too fast or too slowly.

On the other hand, bone-related infections have become a significant concern. Gentamicin is an antimicrobial that wildly used. Minocycline is an antimicrobial that majority used in dental infections. Our objective in project #3 is to determine the 3D bioprinted scaffolds' effectiveness in inhibiting bacterial growth as well as its tissue regenerative properties.

5.2 Materials and Methods

5.2.1 Material

Polycaprolactone (PCL) filament (eSUN, Shenzhen, China)

5.2.2 3D Printing

The above materials were 3D printed into the desired structure by a GEEETECH A10M 3D printer at 185°C. The scaffolds were designed to be 12×12×4 mm with a pore size of 1.7 mm. The diameter of the inside lattice girders is 0.9 mm (**Figure 5-1)**.

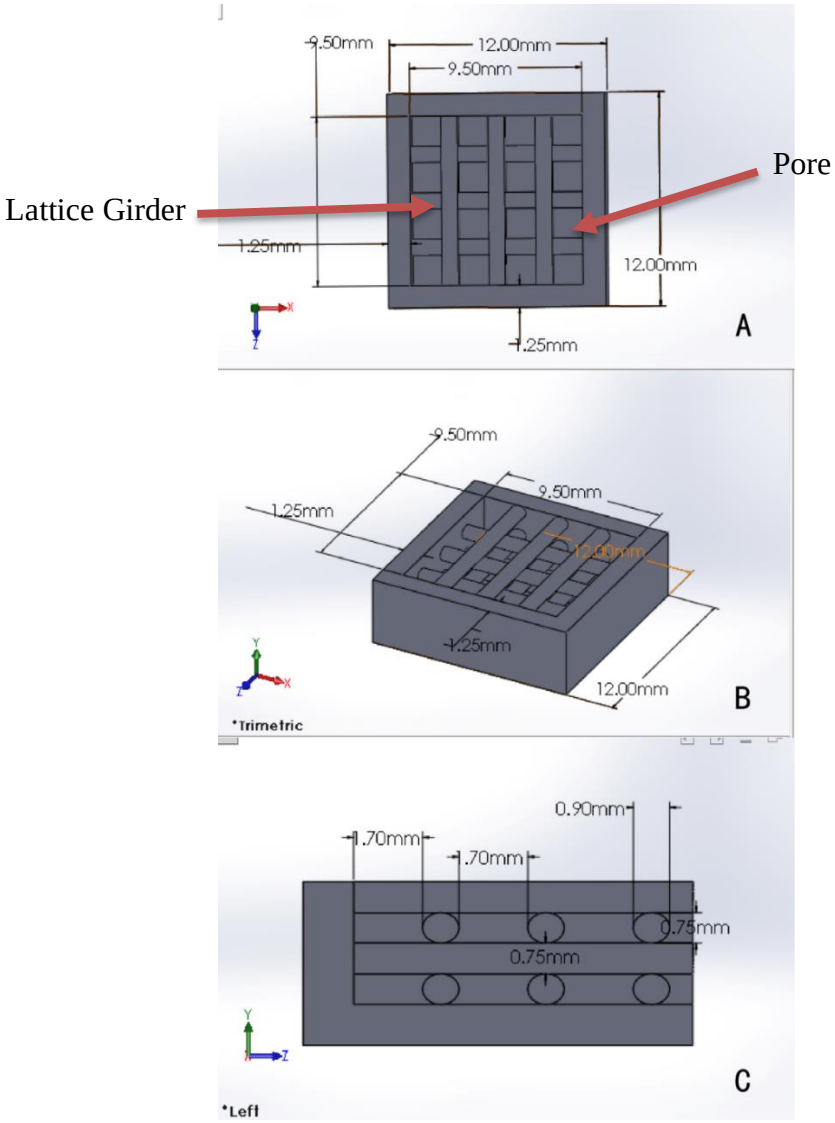

Figure 5-1: 3D printing design. (A) Top view. (B) Trimetric view. (C) Left cut view.

5.2.3 Coating COMA Gel

The 3D printed scaffolds were sterilized in 75% ethanol for 24 hours, washed with 0.01 M PBS, soaked into pre-made 4 mg/ml (marked as 4%) COMA gel (gentamicin+SrHNTs+BMP-2, minocycline+SrHNTs+BMP-2, SrHNTs+BMP-2) and crosslinking under UV light for 18 min.

5.2.4 Morphology and Surface Characterization

The morphology of 3D printed scaffolds was observed under a laser confocal microscope. An SEM/EDS was used to observed and analyze the surface of the samples. EDXRF was used to quantify the amount of Sr in the SrHNTs sample.

5.2.5 Porosity

The porosity of 3D printed scaffolds was calculated via liquid displacement. Three 3D scaffolds were immersed in 5.0 ml (V1) of DI water, then vortexed and sonicated to force the liquid into the pores of the scaffolds. The total volume of scaffolds and DI water was measured (V2). After the water was removed, the scaffolds and the remaining volume of DI water were measured (V3). **Equation 5-1** was used to calculate the final porosity of the scaffold.

$$\text{Porosity} = \frac{\text{V1} - \text{V3}}{\text{V2} - \text{V3}} \qquad \textbf{Equation 5-1}$$

5.2.6 Compressive Test

A CellScale Unit was used to measure the elastic modulus under compression. 3D printed samples were compressed with a 200 N load cell. The stress and strain profiles were measured. The compression modulus was calculated from **Equation 5-2**

$$E = \frac{\sigma}{\varepsilon}, \qquad \textbf{Equation 5-2}$$

where E is the compression modulus, σ is the applied compressive stress, and ε is the strain (compressed length/original length). At least 3 tests were performed for each sample.

5.2.7 Cell Culture

Pre-osteoblast (MC3T3-E1) cells were seeded into a 3D printed scaffold to analyze cell differentiation. MC-3T3 E1 (ATCC) were cultured in an alpha modification of Eagle's medium (α-MEM, Hyclone) with 10% fetal bovine serum (FBS) and 1% Pen/Strep antibiotic (Life Technologies). Cells were cultured in a humidified incubator at 37 °C and 5% CO2 level.

5.2.8 Mineralization-Alizarin Red Staining

Matrix mineralization was assessed by Alizarin Red S (ARS) staining. The cells on the scaffolds were fixed with 99% ethanol for 15 minutes at room temperature, then stained with 2% ARS for 30 minutes. The samples were washed with DI water 4 times and digital images of stained scaffolds were acquired under a brightfield microscope. Cells cultured in the regular 2D condition were used as controls.

To quantify mineralization, 10% acetic acid (Fisher Scientific) was added to the stained samples under agitation for 30 min, allowing the ARS to leech into the acetic acid. The ARS-containing acetic acid was collected and neutralized with 10% ammonium hydroxide (Sigma-Aldrich) until the pH was 4.1− 4.5. The optical density was read with a Thermo Scientific spectrophotometer at 405 nm.

5.2.9 Picrosirius Red Staining

Picrosirius Red is a specific collagen fiber stain that can detect thin fibers. The medium was removed from the cell culture plates and washed with DPBS, then fixed in

99% ethanol. These cells were stained with Picrosirius Red to quantify the amount of collagen secreted. Picrosirius stain was added to each well and removed after an hour of incubation at room temperature. The cells were rinsed with 0.5% acetic acid solution twice and absolute alcohol twice. Digital images of stained scaffolds were acquired under a brightfield microscope. Cells cultured in regular 2D conditions were used as controls.

5.2.10 Bacteria Inhibition Study

Escherichia coli (ATCC 35218) and Staphylococcus aureus (ATCC BAA-1026) were cultured in Luria-Bertani (LB) broth liquid medium. The absorbance of the bacterial concentration at 630 nm is 0.08-0.1, which corresponds to 1 to 2×10^8 CFU/ml. The inoculum from the LB broth was plated onto Mueller-Hilton agar plates under sterile conditions. Control and experimental samples were placed on inoculated plates and were incubated at 37 °C for 18 hours. After incubation, the plates were measured for inhibition zones and compared with gentamicin (10 µg) and minocycline (30 µg) antimicrobial susceptibility disks.

5.2.11 Statistical Analysis

One-way ANOVA or Student T-test was used for statistical analysis. Data were expressed as mean ± standard error. A p-value less than 0.05 was considered statistically significant.

5.3 Results

5.3.1 Morphology of 3D Printed Scaffold and Surface Characteristics

SEM images are shown in **Figure 5-2**. The PCL scaffold with no coating has the smoothest exterior. Gentamicin+SrHNTs+BMP-2 COMA gel-coated PCL and minocycline +SrHNTs+BMP-2 COMA gel-coated PCL samples have some pores that the

gel did not enter. All the gel coatings are relatively smooth, except for the SrHNTs+BMP-2 case, which exhibits air bubbles. These SEM images indicated the gel coatings are uneven on each scaffold.

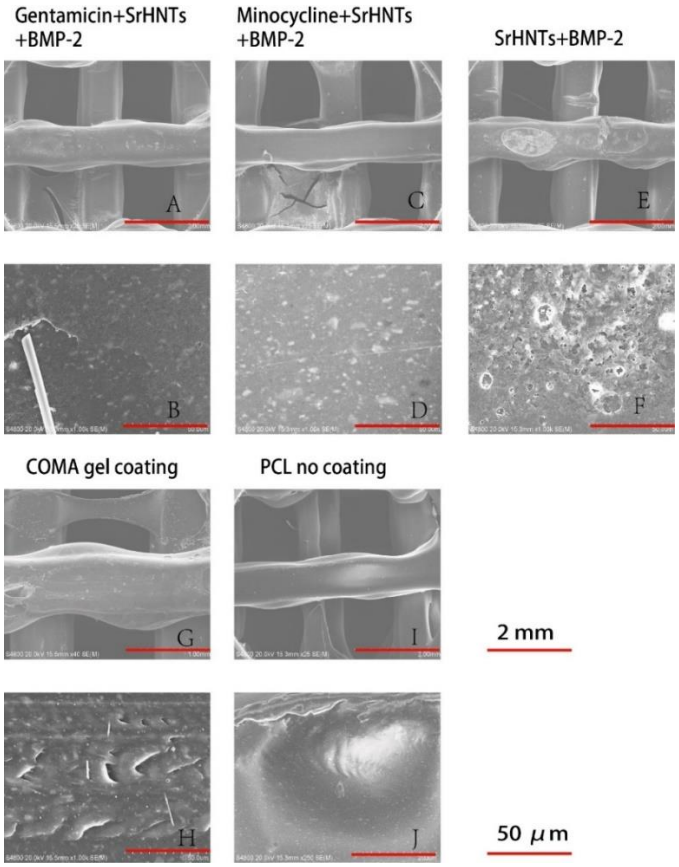

Figure 5-2: The SEM images for 3D printed scaffolds. (A) Gentamicin+SrHNTs+BMP-2 COMA gel-coated PCL sample at 25× magnification. (B) Gentamicin+SrHNTs+BMP-2 COMA gel-coated PCL sample at 1000× magnifications. (C) Minocycline+SrHNTs+BMP-2 COMA gel coated PCL sample at 25 × magnifications. (D) Minocycline+SrHNTs+BMP-2 COMA gel coated PCL sample at 1000 × magnifications. (E) SrHNTs+BMP-2 COMA gel-coated PCL sample at 25× magnifications. (F) SrHNTs+BMP-2 COMA gel coated PCL sample at 1000× magnifications. (G) COMA gel coated PCL sample at 25× magnifications. (H) COMA gel coated PCL sample at 1000 × magnifications. (I) PCL sample at 25 × magnifications. (J) PCL sample at 1000 × magnifications.

All the filaments were printed into pre-designed structures with a pore size of 1200 μm×1200 μm and a layer height of 400 μm. However, the limitations of the 3D

printer altered the resolution slightly. Therefore, the precise pore size was determined by a laser confocal microscope (**Figure 5-3**). Based on the measurement of 16 pores from 1 3D printed scaffold, the average pore size is 1343±231 μm in vertical distance and 1343±231 μm in horizontal distance with a porosity of 63.4±5.7%.

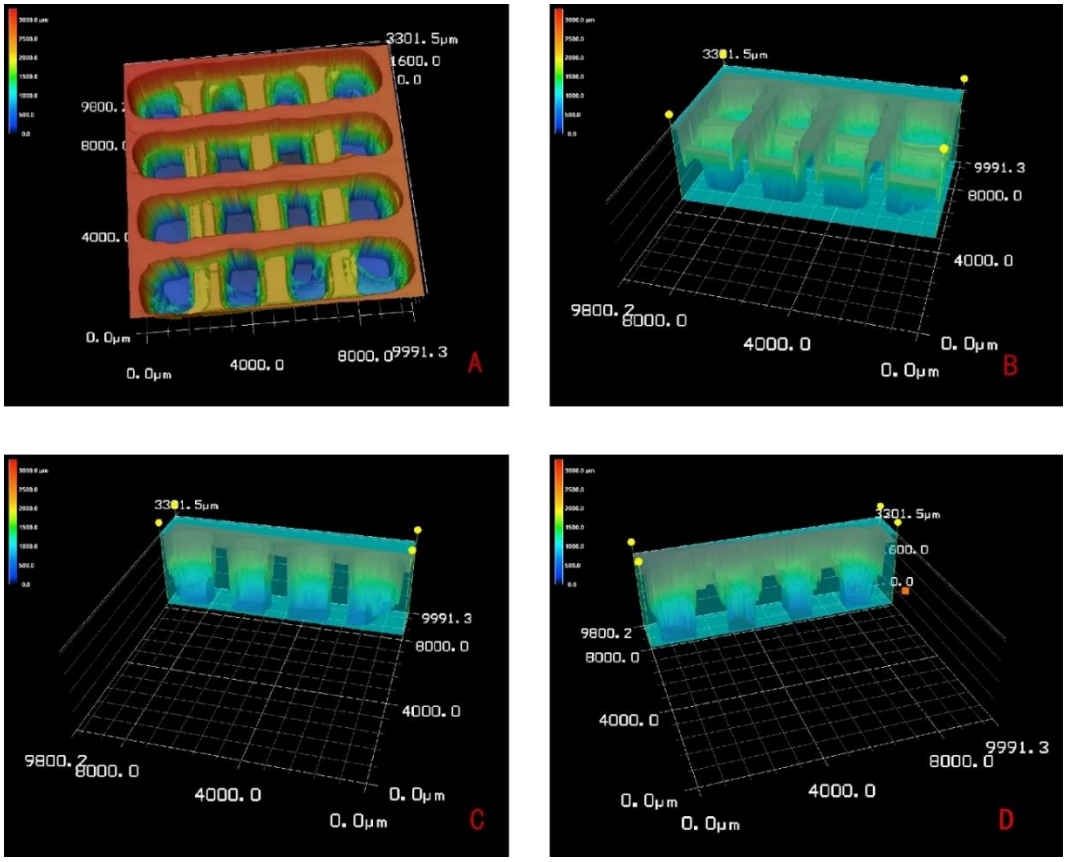

Figure 5-3: (A) Laser confocal image of 3D printed disc. (B) Vertical section of selected area, the layer thickness was measured (734.5±7.8 μm, n=16). (C) Vertical section of selected area, the vertical distance of each pore was measured (1343.25±231 μm, n=16). (D) Horizontal section of selected area, the horizontal distance of each pore was measured (1088.5±215 μm, n=16).

To confirm the existence of SrHNTs and quantify the amount of Sr, energy-dispersive X-ray spectroscopy (EDS) was used. The EDS results of the

gentamicin+SrHNTs+BMP-2 COMA gel-coated PCL sample (**Figure 5-4**) showed 62.47% C, 28.29% O, 4.81% Ca, 3.28% S, 1.14% Au, and no Sr.

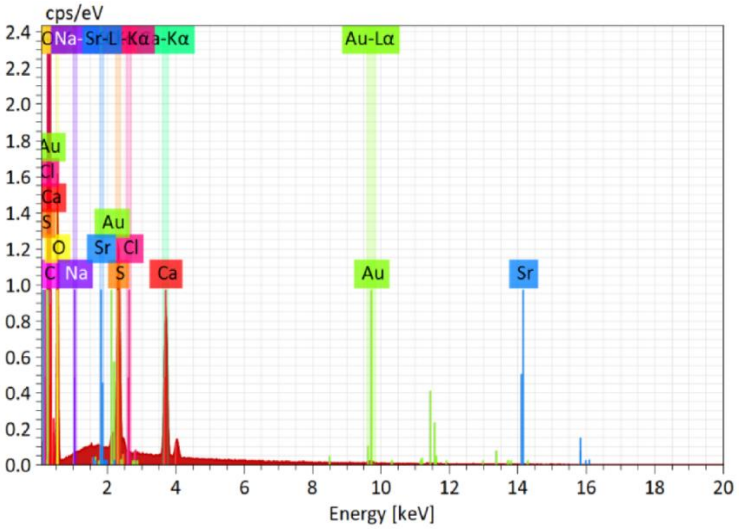

Map

Element	At. No.	Netto	Mass [%]	Mass Norm. [%]	Atom [%]	abs. error [%] (1 sigma)	rel. error [%] (1 sigma)
Carbon	6	109082	62.47	62.47	72.26	7.03	11.25
Oxygen	8	26372	28.29	28.29	24.57	3.55	12.55
Sodium	11	0	0.00	0.00	0.00	0.00	4.43
Sulfur	16	32047	3.28	3.28	1.42	0.14	4.41
Chlorine	17	0	0.00	0.00	0.00	0.00	1.34
Calcium	20	29289	4.81	4.81	1.67	0.17	3.51
Strontium	38	0	0.00	0.00	0.00	0.00	2.11
Gold	79	736	1.14	1.14	0.08	0.08	7.23
		Sum	**100.00**	**100.00**	**100.00**		

Figure 5-4: The EDS graph for each element distribution on a gentamicin+SrHNTs+ BMP-2 COMA gel-coated PCL sample.

The EDS results of minocycline+SrHNTs+BMP-2 COMA gel-coated PCL sample (**Figure 5-5**), when compared to gentamicin sample showed that C% increased from 62.47% to 63.72%, O%, Ca%, S%, and Au% all decreased from 28.29% to 27.5%, 4.81% to 4.55%, 3.28% to 3.23%, and 1.14% to 0.95%, respectively. This change may reflect the difference between gentamicin sulfate and minocycline. Only 0.02% Sr was detected.

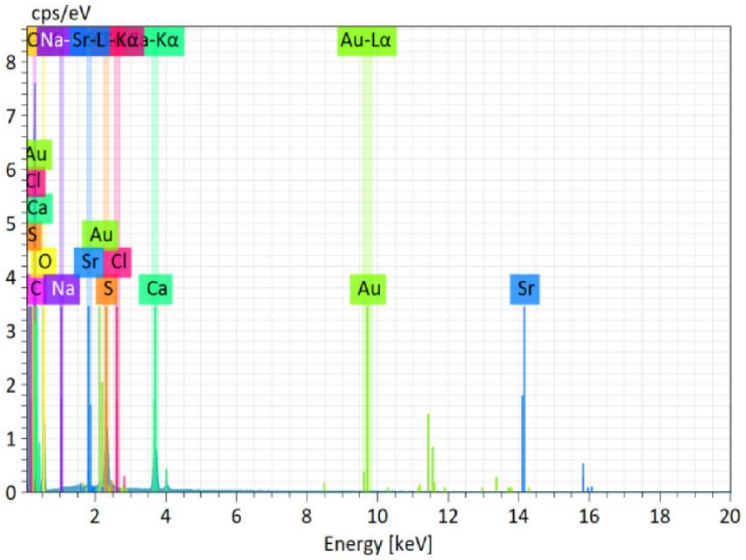

Map

Element	At. No.	Netto	Mass [%]	Mass Norm. [%]	Atom [%]	abs. error [%] (1 sigma)	rel. error [%] (1 sigma)
Carbon	6	115766	63.72	63.72	73.23	7.15	11.21
Oxygen	8	25986	27.50	27.50	23.73	3.46	12.57
Sodium	11	121	0.03	0.03	0.02	0.00	13.73
Sulfur	16	32516	3.23	3.23	1.39	0.14	4.42
Chlorine	17	0	0.00	0.00	0.00	0.00	1.34
Calcium	20	28677	4.55	4.55	1.57	0.16	3.55
Strontium	38	88	0.02	0.02	0.00	0.00	12.94
Gold	79	636	0.95	0.95	0.07	0.08	7.92
		Sum	**100.00**	**100.00**	**100.00**		

Figure 5-5: The EDS graph for each element distribution on minocycline+SrHNTs+ BMP-2 COMA gel-coated PCL sample.

The EDS results of SrHNTs+BMP-2 COMA gel coated PCL sample (**Figure 5-6**), compared to gentamicin sample, showed that C%, and O% increased from 62.47% to 63.57%, and from +28.29% to 29.38%, respectively. Ca%, S%, and Au% all decreased from 4.81% to 3.78%, 3.28% to 2.54%, and 1.14% to 0.69%, respectively. Only 0.01% Sr was detected.

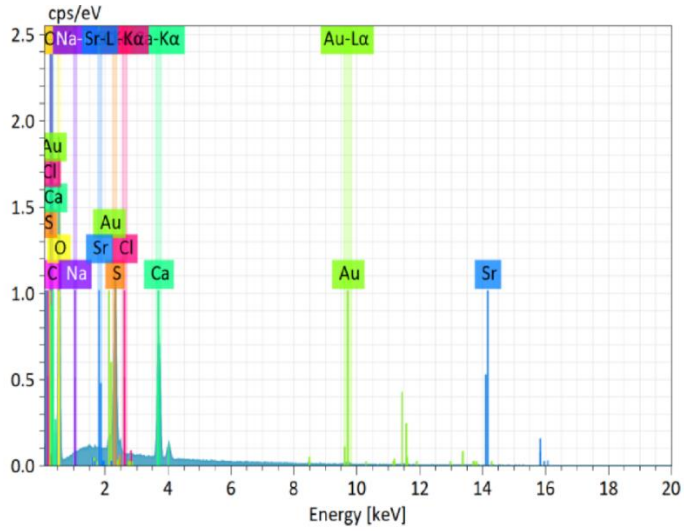

Map

Element	At. No.	Netto	Mass [%]	Mass Norm. [%]	Atom [%]	abs. error [%] (1 sigma)	rel. error [%] (1 sigma)
Carbon	6	134300	63.57	63.57	72.43	7.08	11.13
Oxygen	8	31265	29.38	29.38	25.13	3.63	12.35
Sodium	11	103	0.02	0.02	0.01	0.00	14.49
Sulfur	16	28561	2.54	2.54	1.09	0.12	4.64
Chlorine	17	0	0.00	0.00	0.00	0.00	1.34
Calcium	20	25504	3.78	3.78	1.29	0.14	3.67
Strontium	38	68	0.01	0.01	0.00	0.00	14.37
Gold	79	558	0.69	0.69	0.05	0.06	9.14
		Sum	**100.00**	**100.00**	**100.00**		

Figure 5-6: The EDS graph for each element distribution on SrHNTs+BMP-2 COMA gel-coated PCL sample.

The EDS results of SrHNTs+BMP-2 COMA gel coated PCL sample compared to minocycline sample showed that O% increased from 27.5% to 29.38%, C%, Ca%, S%, and Au% all decreased from 63.72% to 63.57%, 4.55% to 3.78%, 3.23% to 2.54%, and 0.95% to 0.69%, respectively. Only 0.02% Sr was detected.

The EDS results of CoMA gel-coated PCL sample (**Figure 5-7**) compared to SrHNTs sample showed that Ca%, S%, and Au% increased from 3.78% to 4.45%, 2.54% to 3.19%, and 0.69% to 0.87%, respectively. C%, and O% all decreased from 63.57% to 62.68%, and 29.38% to 27.97%, respectively. 0.03% Sr was detected even though there

was no Sr added to the sample. Therefore, the Sr that was detected is an error. The amount of Sr may be too low for the EDS to detect.

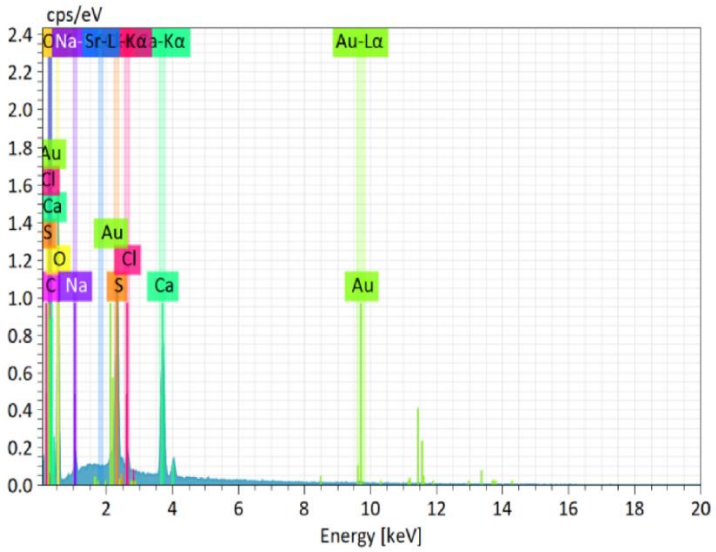

Map

Element	At. No.	Netto	Mass [%]	Mass Norm. [%]	Atom [%]	abs. error [%] (1 sigma)	rel. error [%] (1 sigma)
Carbon	6	49240	62.68	62.68	72.36	7.42	11.84
Oxygen	8	12155	27.97	27.97	24.25	3.84	13.72
Sodium	11	827	0.41	0.41	0.25	0.06	14.48
Sulfur	16	14139	3.19	3.19	1.38	0.14	4.52
Chlorine	17	1537	0.39	0.39	0.15	0.04	11.02
Calcium	20	12792	4.45	4.45	1.54	0.16	3.66
Strontium	38	69	0.03	0.03	0.00	0.00	14.28
Gold	79	279	0.87	0.87	0.06	0.09	10.02
		Sum	**100.00**	**100.00**	**100.00**		

Figure 5-7: The EDS graph for each element distribution on CoMA gel-coated PCL sample.

The EDS results of PCL sample compared to CoMA sample (**Figure 5-8**) showed that C%, and O% increased from 62.68% to 65.48%, and 27.97% to 30.29%, respectively. Ca%, S%, and Au% all decreased from 4.45% to 2.32%, 3.19% to 1.88%, 0.87% to 0%, respectively. These changes may be caused by the difference between the CoMA coating and PCL, as well as the lack of a gold coating on the PCL sample. No Sr was detected.

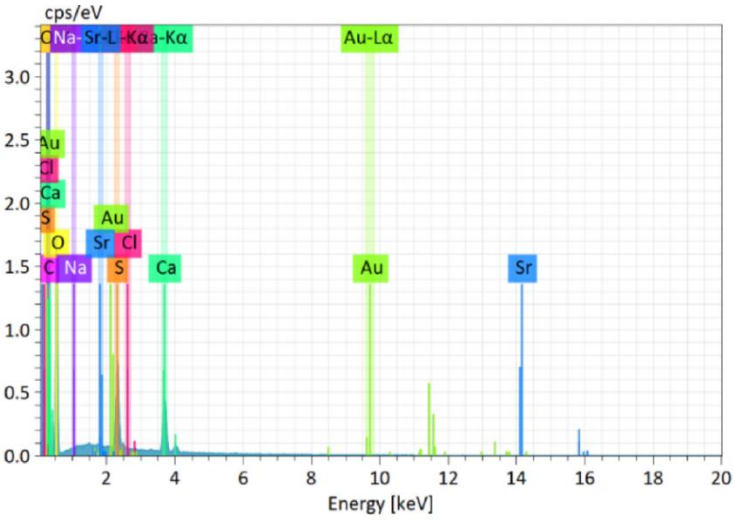

Map

Element	At. No.	Netto	Mass [%]	Mass Norm. [%]	Atom [%]	abs. error [%] (1 sigma)	rel. error [%] (1 sigma)
Carbon	6	130628	65.48	65.48	73.05	7.30	11.14
Oxygen	8	28148	30.29	30.29	25.37	3.78	12.47
Sodium	11	91	0.02	0.02	0.01	0.00	15.09
Sulfur	16	19143	1.88	1.88	0.79	0.09	5.03
Chlorine	17	27	0.00	0.00	0.00	0.00	20.73
Calcium	20	14758	2.32	2.32	0.78	0.10	4.15
Strontium	38	0	0.00	0.00	0.00	0.00	2.11
Gold	79	0	0.00	0.00	0.00	0.00	0.85
		Sum	**100.00**	**100.00**	**100.00**		

Figure 5-8: The EDS graph for each element distribution on the PCL sample.

To further quantify the amount of Sr loaded into and onto the HNTs, EDXRF was performed. Under no vacuum condition **(Figure 5-9**), two Sr radiation signals were detected. These were caused by the Sr electrons transitioning into different energy levels. However, one of the radiation signals was too weak to be detected, the Sr signal resulted in two peaks. Si and Al signals were not present because the no vacuum condition caused these signals to be absorbed by the air.

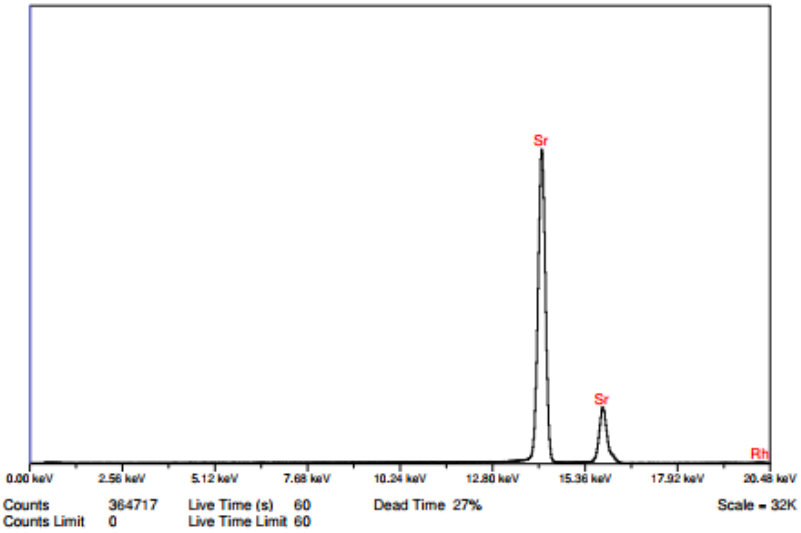

Figure 5-9: Energy Dispersive X-ray Fluorescence (EDXRF) graph for SrHNTs (no vacuum) element distribution.

Under a vacuum condition (**Figure 5-10**), three strong Sr signals were detected. However, one of them was in the same position as the Si signal and covered by the Si signal. Al and Si signals are also shown in the figure.

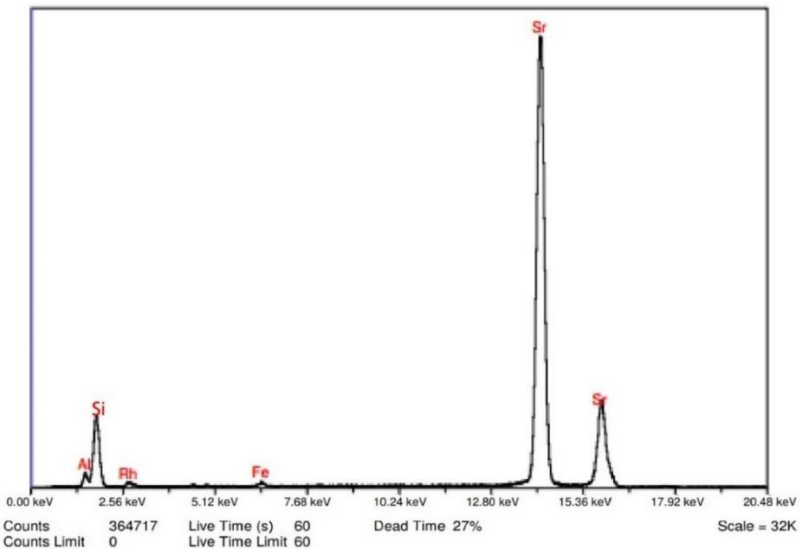

Figure 5-10: EDXRF graph for the SrHNTs element distribution.

In **Figure 5-11**, three of the Sr signals are displayed. Signals from C and O were not displayed because these elements use a different spectroscopic crystal from Sr.

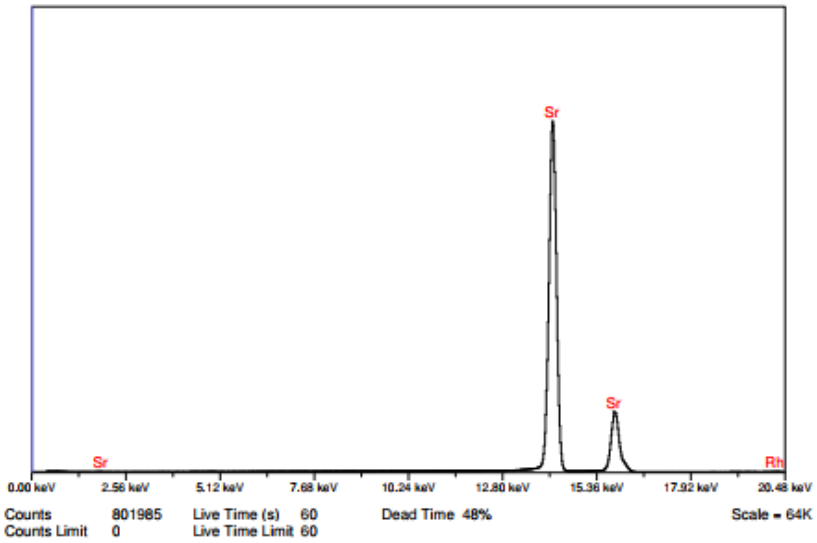

Figure 5-11: EDXRF graph for SrCO3 element distribution.

The pure HNTs have strong signals for Al and Si, and barely any signal for Sr. SrHNTs tested without vacuum have two weak signals (**Figure 5-12**) compared to SrHNTs and $SrCO_3$. Since the amount of SrHNTs and $SrCO_3$ were the same, the SrHNTs signal strength is approximately 45%. The amount of Sr loading into or onto HNTs is approximately 40-45%.

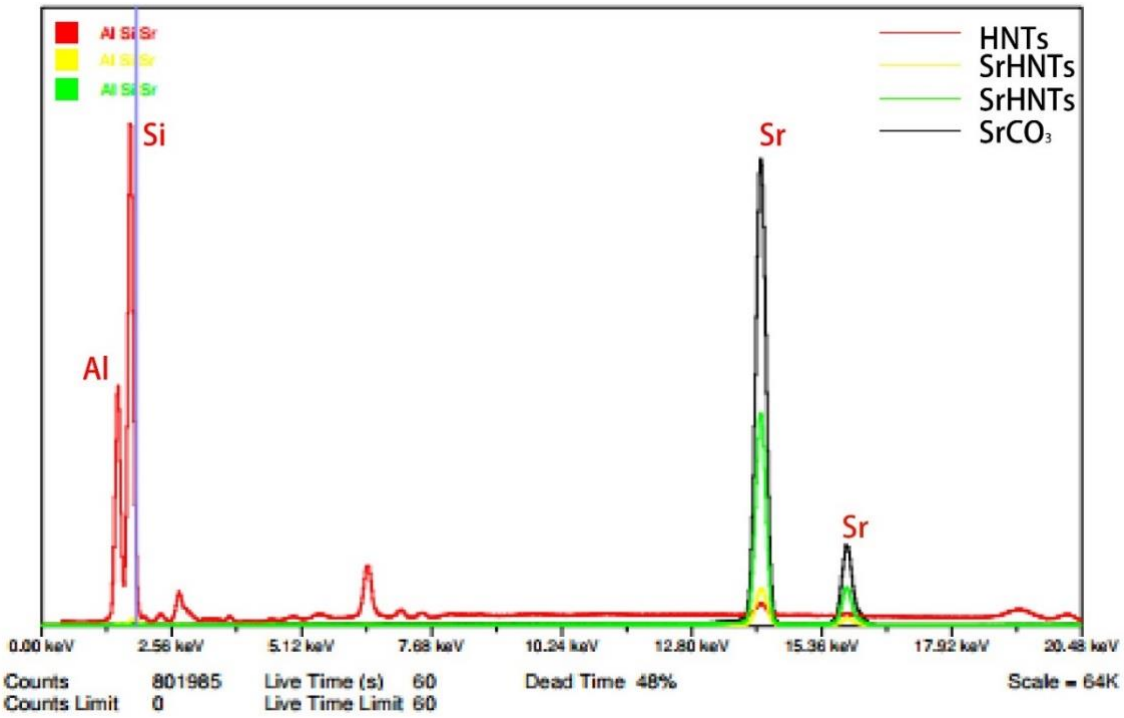

Figure 5-12: EDXRF graph for each element distribution. The red line represents the element distribution result for the HNTs sample. The yellow line represents the element distribution result for Sr-coated HNTs sample that was tested outside a vacuum. The green line represents the element distribution results for the Sr-coated HNTs sample that were tested under vacuum. The black line represents the element distribution result for the $SrCO_3$ sample.

5.3.2 Compressive Strength

To test the mechanical properties of the 3D scaffold, the PCL samples were compared to PLA (**Figure 5-13**). The instrument is limited to a maximum force of 200 N for the failure test, and at that force, none of the scaffolds failed. Since the compressive strength varies between 100 and 200 MPa for cortical bone and between 2 and 20 MPa for cancellous bone, our PCL samples demonstrated that they were strong enough to be used as bone scaffolds. ANOVA analysis showed a significant difference among the four groups.

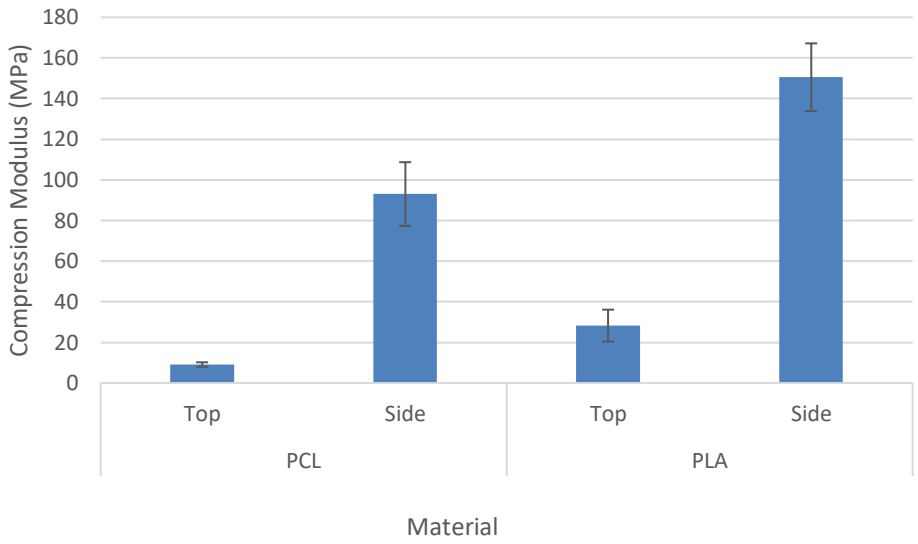

Figure 5-13: Compression modulus of PCL and PLA. Area: side: 48 mm2, Top: 144 mm2. (Error bars are standard deviations, n=4, $p<0.05$).

5.3.3 Bacteria Inhibition Study

The CoMA gel and SrHNTs+BMP-2 samples did not have any bacteria inhibition zone (**Figure 5-14**). The SrHNTs+BMP-2+Gentamicin and SrHNTs+BMP-2+Minocycline samples showed similar inhibition zones compared to gentamicin standard disks. However, the inhibition zone of SrHNTs+BMP-2+Gentamicin and SrHNTs+BMP-2+Minocycline samples are smaller than minocycline.

The SrHNTs+BMP-2+Gentamicin and SrHNTs+BMP-2+Minocycline samples have a larger inhibition zone in *Staph.a* plate than *E. coli* plates. However, the size difference of the inhibition zone of SrHNTs+BMP-2+Minocycline in *E. coli* and *Staph.a* plates is smaller than SrHNTs+BMP-2+Gentamicin samples. Compared to gentamicin disks, the minocycline disks have a larger inhibition zone in *E. coli* plates than *S.au* plates.

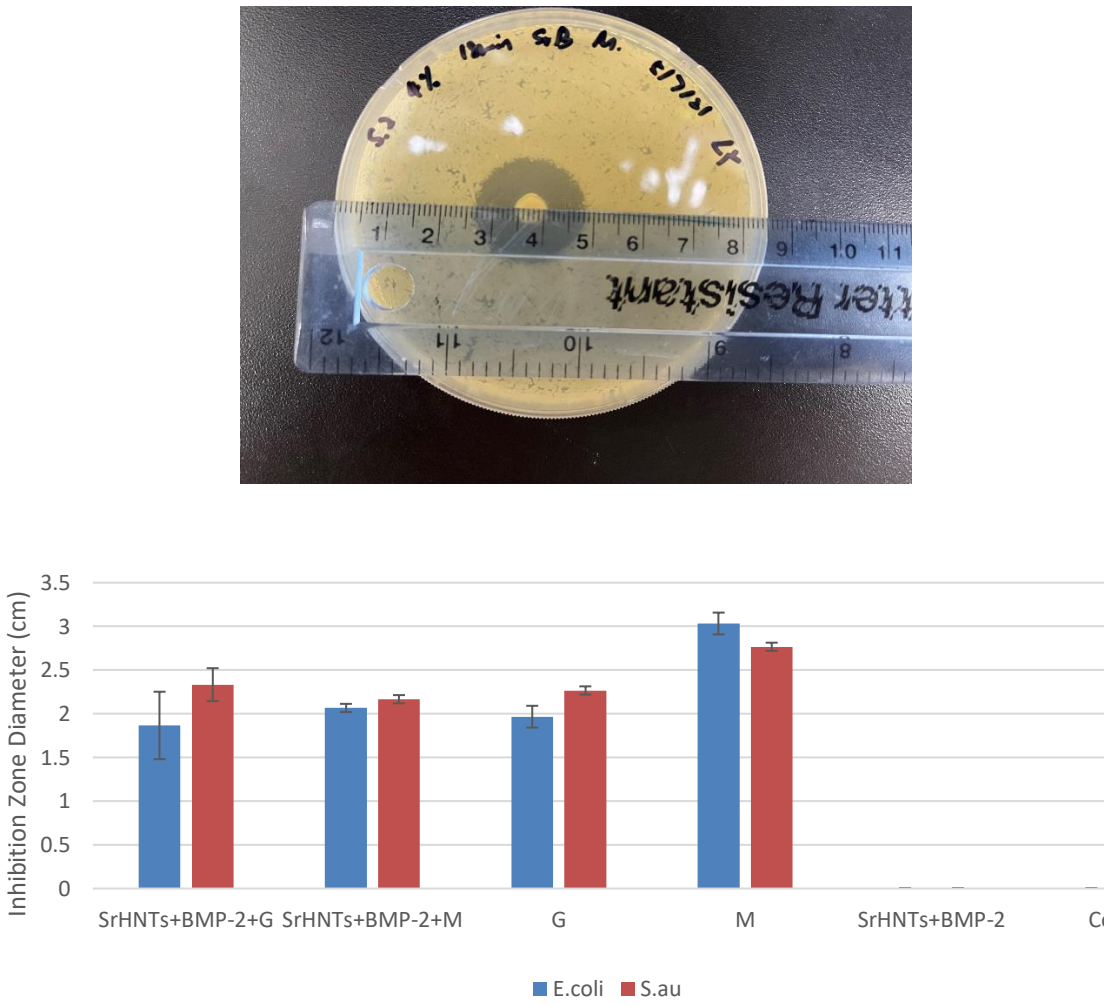

Figure 5-14: Top: Measurement of bacteria inhibition zone. Bottom: Bacteria inhibition zone. (Error bars are standard deviations, n=3, $p<0.05$).

5.3.4 Mineralization-Alizarin Red Staining

Cell mineralization, collagen synthesis, and protein secretion are three important indexes for an early stage of bone repair and regeneration. Thus, we studied the mineralization and collagen synthesis of the 3D printed scaffolds to determine the optimal design.

Calcium deposition can be identified by Alizarin Red stain. The Alizarin Red stain calcium complex chelates with calcium and presents red color under a microscope at a bright field. As shown in **Figure 5-15**, PCL samples exhibited minimal calcium

deposition, and the samples coated with COMA gel had more calcium deposition. Calcium deposition increased with incubation time. The gentamicin +SrHNTs+BMP-2 COMA gel-coated group, SrHNTs+BMP-2 COMA gel-coated group, and COMA gel-coated group had approximately the same amount of calcium deposition. To further confirm the amount of calcium deposition, the UV absorbance was measured.

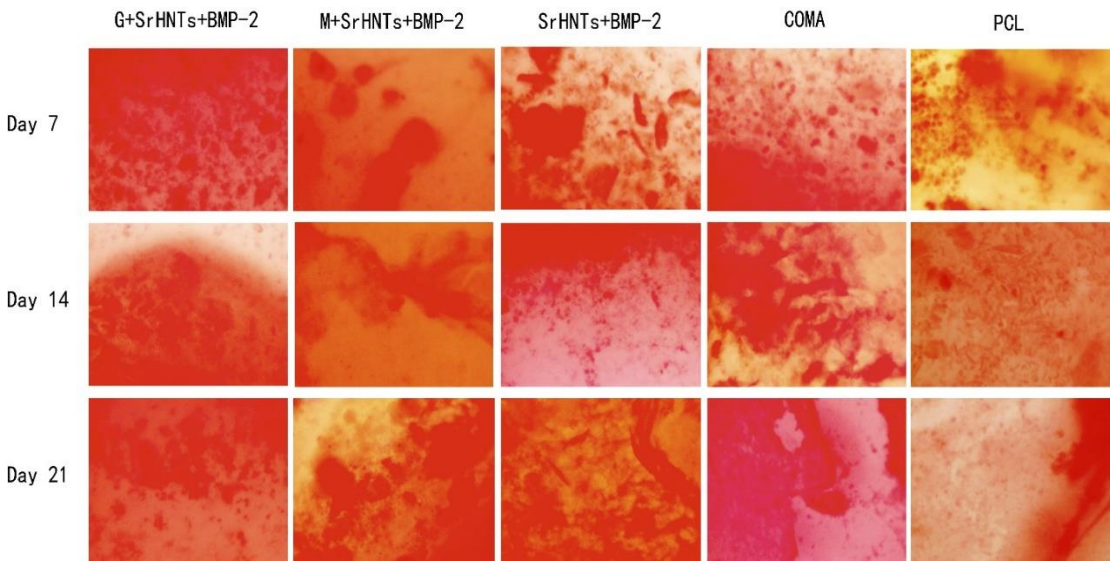

Figure 5-15: Alizarin Red Staining of cells after 7-, 14-, and 21-days incubation. Dark red represented calcium deposition.

The UV absorbance results (**Figure 5-16**) showed that the amount of calcium deposition in the scaffolds coated with COMA gel was significantly higher than in the PCL scaffolds. On day 21, the gentamicin+SrHNTs+BMP-2 (G+SrB) group had the highest amount of calcium deposition in the COMA gel-coated groups. The SrHNTs+BMP-2 (SrB) group had the second-highest amount of calcium deposition in the COMA gel-coated groups. Minocycline+ SrHNTs+BMP-2 (M+SrB) group had the lowest amount of calcium deposition in the COMA gel-coated groups.

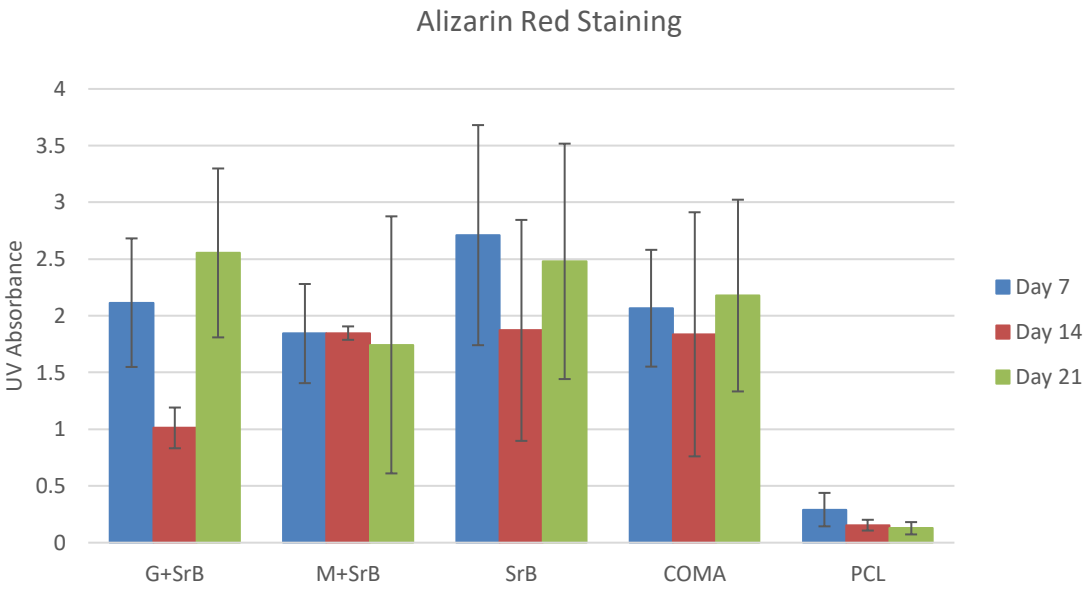

Figure 5-16: UV absorbance for Alizarin Red Staining of cells after 7-, 14-, and 21-days incubation. (Error bars are standard deviations, n=3, $p<0.05$).

5.3.5 Picrosirius Red Staining

Sirius Red dye is strongly acidic, and it easily binds to basic groups in collagen molecules. Under an ordinary optical microscope, collagen is dyed red, and muscle fibers and cytoplasm are dyed yellow. **Figure 5-17** shows images from the bottom layer of the 3D scaffolds, and **Figure 5-18** shows images from the top layer. Cells attached and grew on the gentamicin+SrHNTs+BMP-2 and Minocycline+ SrHNTs+BMP-2 scaffolds on day 7. Some collagen fibers were synthesized in between cells on the gentamicin+SrHNTs+BMP-2 and Minocycline+ SrHNTs+BMP-2 scaffolds on day 7. On day 7, SrHNTs+BMP-2 and COMA gel groups also had some cells grow, but not as clear as the gentamicin+SrHNTs+BMP-2 and Minocycline+ SrHNTs+BMP-2 groups. SrHNTs+BMP-2 scaffolds had more collagen fibers synthesized than COMA scaffolds. Few cells grew on the PCL scaffolds, and no obvious collagen fibers were synthesized. Cell proliferation and collagen fibers increased with incubation time. On day 21, all gel-

coated scaffolds had high cell density on the surface. Most collagen fibers were formed under the cells. However, PCL scaffolds still had minimal cell attachment and growth, with minimal collagen fiber formation on the surface. Minocycline+SrHNTs+BMP-2 groups had the lowest number of cells and collagen fibers.

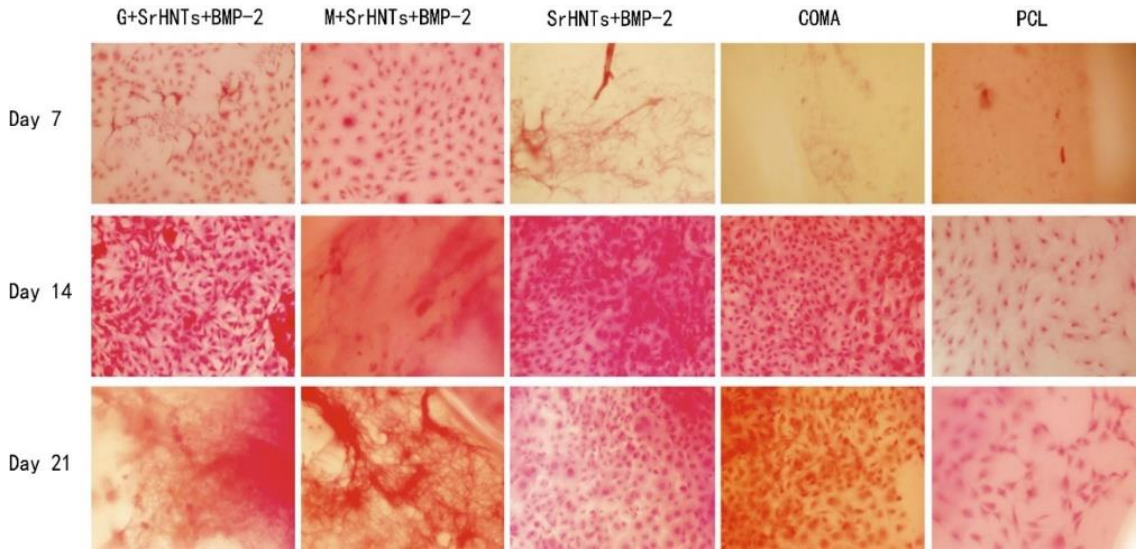

Figure 5-17: Picrosirius Red Stain for the bottom layer of 3D scaffolds.

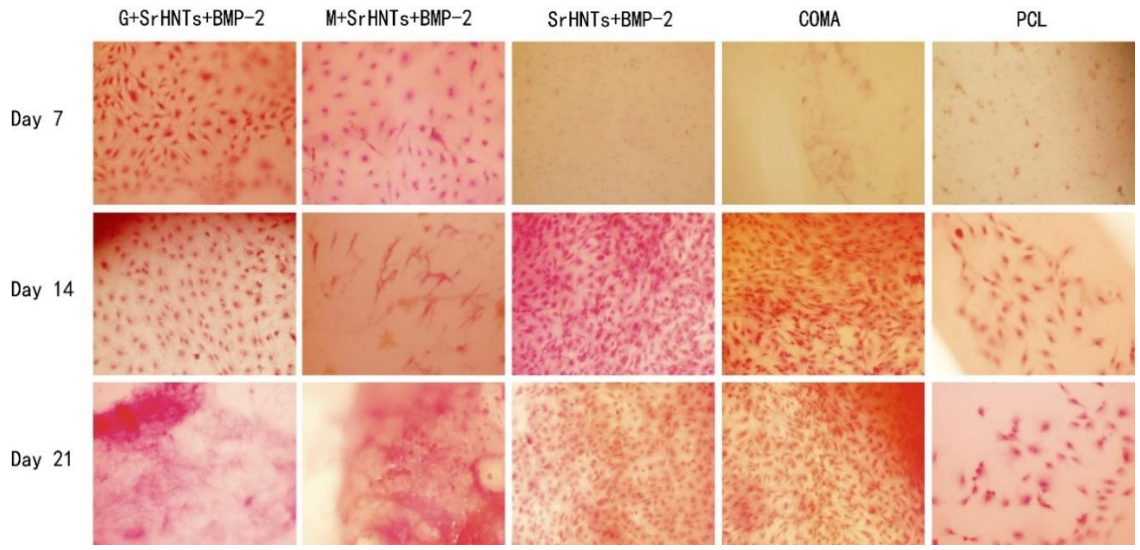

Figure 5-18: Picrosirius Red Stain for the top layer of 3D scaffolds.

5.4 Conclusions

The CoMA gel and SrHNTs+BMP-2 samples had no bacteria inhibition zone. The SrHNTs+BMP-2+Gentamicin and SrHNTs+BMP-2+Minocycline samples showed similar inhibition zones compared to gentamicin standard disks (10 μg). However, the inhibition zone of SrHNTs+BMP-2+Gentamicin and SrHNTs+BMP-2+Minocycline samples are smaller than minocycline standard disks (30 μg). The mineralization results showed that the amount of calcium deposition in the scaffolds coated with COMA gel is significantly higher than the PCL scaffolds. On day 21, the gentamicin+SrHNTs+BMP-2 (G+SrB) group had the highest amount of calcium deposition in the COMA gel-coated groups. The collagen synthesis study showed that all gel-coated scaffolds had substantial cell growth on the surface. Most collagen fibers were formed under the cells. However, PCL scaffolds still had few cells attached or growing on the surface. However, Minocycline+ SrHNTs+BMP-2 groups had the lowest number of cells and collagen fibers in COMA gel-coated groups. Few collagen fibers formed on the PCL scaffolds after 21 days of incubation.

5.5 Discussion

We designed large pores for our scaffolds so that the COMA gel can enter the scaffolds and cover their insides. The confocal image showed that there is a difference between the 3D printed bracket and our design, which is caused by a lack of precision in the 3D printer. At the same time, PCL does not tolerate high temperatures, and it will deform to a certain extent after cooling, which also affects the final printing result.

Base on the bacteria inhibition study, we found gentamicin and minocycline had a similar inhibition zone. This indicated two antibiotics have no significant difference in

antibacterial effects. However, the gentamicin sample showed superiority over the minocycline sample in terms of calcium deposition, cell growth, and collagen fiber synthesis.

CHAPTER 6

DISCUSSION

These three projects were undertaken to explore the potential application of halloysite nanotubes and BMP-2 in bone disease repair and bone regeneration medical devices. Critical in our design was to determine the osteoblast's migration rate in response to different concentrations of HNTs, BMP-2, and HNTs combine with BMP-2. Previous research has already demonstrated that the incorporation of HNTs can enhance bone regeneration [258-260]. In addition, BMP-2 is another agent that strongly promotes bone formation in vitro and in vivo [261,262]. A recent study by Huang et al. (2019) has provided support for this observation [263].

Several previous studies have used exogenous growth factors to recruit osteoblasts to the damaged site for a better therapeutic outcome [7,8,264]. As a result, the delivery of growth factors to the damaged site has become a widely used methodology that facilitates tissue repair by enhancing host cell recruitment, proliferation, and activation [265,266]. This approach has shown that faster recruitment of repair cells to the defect site can significantly reduce the time required for bone tissue repair and remodeling and can thus enhance bone reconstruction. However, clinicians currently use large amounts of BMP-2 (up to 40 mg) for bone repair [7,8,265]. From the amount of BMP-2 used, only 75 μg binds to 1 g of collagen [266]. Mature recombinant BMP is not soluble at neutral pH and thus the leftover BMP-2 tends to form large molecular weight

(MW) agglomerates, which in combination with bovine collagen can induce significant inflammation, swelling, and heterotopic ossification in other areas [266]. Therefore, this research is important because it provides a possible approach for designing a safe and cost-effective in situ method of bone repair. In this study, BMP-2 and HNTs showed a mutual promotion in the recruitment of osteoblasts. The additive of Sr especially significantly increased pre-osteoblasts differentiation and osteogenesis in vitro. As discussed in Chapter 5, SrHNTs+BMP-2 COMA nanocomposites PCL scaffolds showed not only superior mechanical properties but also a huge osteogenesis potential. In the presence of all groups of COMA nanocomposites, pre-osteoblasts synthesize the collagen fibers leading to the early formation of the collagen matrix and calcium deposition. On the one hand, the gentamicin coating did not significantly inhibit cell growth. On the other hand, minocycline coating showed a low-level inhibitory effect on the growth of pre-osteoblasts. By day 21, the gentamicin+SrHNTs+BMP-2 COMA-coated scaffolds showed significantly increased and incomparable cell proliferation capacity compared to the PCL group. Therefore, gentamicin+SrHNTs+BMP-2 COMA-coated scaffolds can not only prevent bacterial contamination but also promote bone regeneration at the same time.

Some research shows that a COMA-composed nanoparticles system improved not only its hydrogel's mechanical properties but also its bioactivity. Kajave et al. [267] created a bioactive ink composed of Bioglass 45S5 (BG) and methacrylated collagen (CMA) for 3D printed bone tissue. They showed a similar result to our study, BG incorporated CMA (BG-CMA) constructs maintained high cell viability of human mesenchymal stem cells. BG-CMA constructs showed a higher cell-mediated calcium

deposition compared to CMA alone. In addition, BG particles within the collagen network improved stability and reduced the swelling of collagen hydrogels. Similarly, Kim et al. [268] introduced a bioceramic-based cell-printing technique and a cell (MC3T3)-laden ceramic (α-tricalcium phosphate (α-TCP) type I collagen) structure. Their results showed that the scaffold had good cellular activities, including metabolic activity and mineralization. In another research, Kajave et al. [269] provided a viable strategy to yield mechanically superior, cell compatible, and printable CMA hydrogels that used a dual crosslinking mechanism. Dual crosslinking was performed by first photochemical crosslinking of CMA hydrogels, followed by chemical crosslinking with two different concentrations of genipin (i.e., 0.5 mM (low dual) or 1 mM (high dual)). In this way, they improved the photochemical crosslinking of CMA hydrogels' mechanical weakness, increased degradation time in vivo, and kept its high cell viability.

Similar systems such as gelatin methacrylate (GelMA) composed nanotube system also showed results like ours. Shin et al. added carbon nanotubes (CNTs) into GelMA hydrogels to enhance their stiffness without inhibiting 3D cellular growth [270]. Huang et al. [271] proposed a biomimetic GelMA/nano fish bone hybrid hydrogel to systematically investigate its potential for bone regeneration. The results showed that nano fish bone incorporation enhanced the mechanical performance of the hybrid hydrogel and improved bone regeneration. Ou et al. [272] fabricated a nanosilver/halloysite nanotubes/gelatin methacrylate (nAg/HNTs/GelMA) hybrid hydrogel and evaluated its osteoimmunomodulatory and antibacterial properties in vitro and in vivo. The results showed that nAg/HNTs/GelMA hydrogel not only had good biocompatibility with human periodontal ligament stem cells (hPDLSCs) and

macrophages but also enhanced the osteogenic differentiation. Moreover, compared with HNTs/GelMA hydrogel, the nAg/HNTs/GelMA hydrogel significantly showed a stronger antiinfection ability of Gram-positive and Gram-negative bacteria in vitro and in vivo. Above all, all these results support what our research found. Our result showed a significantly higher osteocalcin concentration level and more calcium deposition compared to the research mentioned above. Secondly, we added an antimicrobial effect against Gram-positive and Gram-negative bacteria to our scaffolds. Thirdly, we reduced the BMP-2 concentration level from mg/ml to ng/ml, a significant breakthrough. Meanwhile, our research has provided many discoveries and new choices in BTE materials. An example of this is the information we provided on the early formation of collagen matrix on a COMA nanocomposite scaffold.

Currently, a limitation for repairing large bone defects is the formation of blood vessels. If the 3D printed scaffold is too big, it could affect blood vessel formation. Recent research showed some large bone defect models of rabbits' mandibles (26 × 5 × 3 mm) exceeded the critical size which is reported as a basic length of about 15 mm [273,274] to achieve regeneration [275]. They designed a dual delivery of BMP-2 and basic fibroblast growth factor (bFGF) from a new nano-composite scaffold loaded with vascular stents [275]. This provides us with a new method to repair and regenerated large bone defects.

CHAPTER 7

CONCLUSIONS AND FUTURE WORK

7.1 Conclusions

In Project #1, we found that HNT groups have the highest migration rate when they have 250 μg/ml concentration. Of the BMP-2 groups, 5 ng/ml BMP-2 showed the most migrated cells. When HNTs are present in the medium, 5 ng/ml BMP-2 had the highest migration rate. Especially the group which has 5 ng/ml BMP-2 and 50 μg/ml HNTs. All these results indicate that the HNTs and HNTs doped with BMP-2 can become a new agent for use in bone regeneration.

In Project #2, In the degradation study, the 4% CoMA group degraded faster than the 8% group. In the 4% CoMA group, samples crosslinked for 14 min degraded faster than samples crosslinked for 18 min. The contact angel results show that SrHNTs 4% 14 min CoMA hydrogel had the smallest contact angel at 80 seconds. SrHNTs and BMP-2 4% 14 min CoMA hydrogel had the second smallest contact angle at 80 seconds. All samples showed a similar proliferation rate. The differentiation results demonstrated that SrHNTs and BMP-2 CoMA 4% 18 min-crosslinked hydrogels enhanced preosteoblasts differentiation and osteogenesis in vitro.

In Project #3, The CoMA gel and SrHNTs+BMP-2 samples had no bacteria inhibition zone. The SrHNTs+BMP-2+Gentamicin and SrHNTs+BMP-2+Minocycline samples showed similar inhibition zones compared to gentamicin standard disks (10 μg).

However, the inhibition zone of SrHNTs+BMP-2+Gentamicin and SrHNTs+BMP-2+Minocycline samples are smaller than minocycline standard disks (30 µg). The mineralization results showed that the amount of calcium deposition in the scaffolds coated with COMA gel is significantly higher than the PCL scaffolds. On day 21, gentamicin+SrHNTs+BMP-2 (G+SrB) group had the highest amount of calcium deposition in the COMA gel-coated groups. The collagen synthesis study showed that all gel-coated scaffolds had substantial cell growth on the surface. Most collagen fibers were formed under the cells. However, PCL scaffolds still had few cells attached or growing on the surface. However, Minocycline+ SrHNTs+BMP-2 groups had the lowest number of cells and collagen fibers in COMA gel-coated groups. Few collagen fibers formed on the PCL scaffolds after 21 days of incubation.

7.2 Future Work

Since we have confirmed the optimal combination of the COMA-coated scaffold, the next stage is to explore its application in biomedical engineering through animal testing. Animal testing will provide us with more information on how the scaffold works in vivo. If the scaffold works ideally, it will provide a meaningful treatment plan for bone tissue repair and regeneration. Meanwhile, this technology can be used not only for bone repair and regeneration but also for the repair and regeneration of other tissues. In addition, COMA hydrogel can also be combined with other materials, such as Polyurethane (PU), Polylactic (PLA), and silk protein, other structures, such as microspheres and films, and other biological factors, such as vascular endothelial growth factor (VEGF), hepatocyte growth factor (HGF), activin-A, epidermal growth factor

(EGF), and transforming growth factor β (TGF-β), to develop more personalized designs. This technology opens multiple directions for further exploration.

BIBLIOGRAPHY

1. Fernández Tresguerres, Isabel, et al. "Physiological bases of bone regeneration I: Histology and physiology of bone tissue." (2006).

2. Einhorn, Thomas A. "The cell and molecular biology of fracture healing." *Clinical Orthopaedics and Related Research*® 355 (1998): S7-S21.

3. Barry, Frank P. "Biology and clinical applications of mesenchymal stem cells." *Birth Defects Research Part C: Embryo Today: Reviews* 69.3 (2003): 250-256.

4. Hofer, Heidi R., and Rocky S. Tuan. "Secreted trophic factors of mesenchymal stem cells support neurovascular and musculoskeletal therapies." *Stem Cell Research & Therapy* 7.1 (2016): 1-14.

5. Chen, Fa-Ming, et al. "Homing of endogenous stem/progenitor cells for in situ tissue regeneration promises, strategies, and translational perspectives." *Biomaterials* 32.12 (2011): 3189-3209.

6. Hughes, Francis J., Jane E. Aubin, and Johan NM Heersche. "Differential chemotactic responses of different populations of fetal rat calvaria cells to platelet-derived growth factor and transforming growth factor β." *Bone and mineral* 19.1 (1992): 63-74.

7. Takata, Takashi, Mutsumi Miyauchi, and Hom‐Lay Wang. "Migration of osteoblastic cells on various guided bone regeneration membranes." *Clinical oral implants research* 12.4 (2001): 332-338.

8. Lind, M. A. R. T. I. N., et al. "Chemotaxis of human osteoblasts: Effects of osteotropic growth factors." *Apmis* 103.1‐6 (1995): 140-146.

9. Lee, Dong Hee, et al. "Chemotactic migration of human mesenchymal stem cells and MC3T3-E1 osteoblast-like cells induced by COS-7 cell line expressing rhBMP-7." *Tissue engineering* 12.6 (2006): 1577-1586.

10. Mehrotra, Meenal, et al. "Differential regulation of platelet‐derived growth factor stimulated migration and proliferation in osteoblastic cells." *Journal of cellular biochemistry* 93.4 (2004): 741-752.

11. Tang, Yi, et al. "TGF-β1–induced migration of bone mesenchymal stem cells couples bone resorption with formation." *Nature medicine* 15.7 (2009): 757-765.

12. Lind, Martin, E. F. Eriksen, and C. Bünger. "Bone morphogenetic protein-2 but not bone morphogenetic protein-4 and-6 stimulates chemotactic migration of human osteoblasts, human marrow osteoblasts, and U2-OS cells." *Bone* 18.1 (1996): 53-57.

13. Poynton, Ashley R., and Joseph M. Lane. "Safety profile for the clinical use of bone morphogenetic proteins in the spine." *Spine* 27.16S (2002): S40-S48.

14. Lieberman, Jay R., Aaron Daluiski, and Thomas A. Einhorn. "The role of growth factors in the repair of bone: biology and clinical applications." *JBJS* 84.6 (2002): 1032-1044.

15. Dharmaraj, Bhagya Mathi, et al. "Multifunctional halloysite nanotube based composite coatings on titanium as metal implant for orthopedic applications." *Composites Part C: Open Access* 3 (2020): 100077.

16. Li, Ye, et al. "Bone defect animal models for testing efficacy of bone substitute biomaterials." *Journal of orthopaedic translation* 3.3 (2015): 95-104

17. Lvov, Yuri M., Melgardt M. DeVilliers, and Rawil F. Fakhrullin. "The application of halloysite tubule nanoclay in drug delivery." *Expert opinion on drug delivery* 13.7 (2016): 977-986.

18. Fizir, Meriem, et al. "Halloysite nanotubes in analytical sciences and in drug delivery: A review." *Microchimica Acta* 185.8 (2018): 1-33Steele, D. Gentry, and Claud A. Bramblett. *The anatomy and biology of the human skeleton*. Texas A&M University Press, 1988.

19. Cavendish, Marshall. "Mammal anatomy: an illustrated guide." *New York: Marshall Cavendish Corporation* (2010).

20. Markings, Bone. "The skeletal system." (1995).

21. Clarke, Bart. "Normal bone anatomy and physiology." *Clinical journal of the American Society of Nephrology* 3.Supplement 3 (2008): S131-S139.

22. https://www.visiblebody.com/learn/skeleton/types-of-bones

23. Buckwalter, J. A., et al. "Bone biology." *J Bone Joint Surg Am* 77.8 (1995): 1256-1275.

24. Buenzli, Pascal R., and Natalie A. Sims. "Quantifying the osteocyte network in the human skeleton." *Bone* 75 (2015): 144-150.

25. Tate, Melissa L. Knothe, et al. "The osteocyte." *The international journal of biochemistry & cell biology* 36.1 (2004): 1-8.

26. Burchardt, H., and W. F. Enneking. "Transplantation of bone." *Surgical Clinics of North America* 58.2 (1978): 403-427.

27. DePalma, A. F., et al. "Anterior interbody fusion for severe cervical disc degeneration." (1972).

28. Kalfas, Iain H. "Principles of bone healing." Neurosurgical focus 10.4 (2001): 1-4.

29. Marsell, Richard, and Thomas A. Einhorn. "The biology of fracture healing." Injury 42.6 (2011): 551-555.

30. O'Connor, Francis G., ed. ACSM's sports medicine: a comprehensive review. Lippincott Williams & Wilkins, 2012.

31. Perez, Jose R., et al. "Tissue engineering and cell-based therapies for fractures and bone defects." *Frontiers in bioengineering and biotechnology* 6 (2018): 105.

32. Annamalai, Ramkumar T., et al. "Injectable osteogenic microtissues containing mesenchymal stromal cells conformally fill and repair critical-size defects." *Biomaterials* 208 (2019): 32-44.

33. Zhang, Xiaojin, et al. "Cell-free 3D scaffold with two-stage delivery of miRNA-26a to regenerate critical-sized bone defects." *Nature communications* 7.1 (2016): 1-15.

34. Schemitsch, Emil H. "Size matters: defining critical in bone defect size!." *Journal of orthopaedic trauma* 31 (2017): S20-S22.

35. Lee, Jee-Wook, et al. "Long-term clinical study and multiscale analysis of in vivo biodegradation mechanism of Mg alloy." *Proceedings of the National Academy of Sciences* 113.3 (2016): 716-721.

36. Bhumiratana, Sarindr, et al. "Tissue-engineered autologous grafts for facial bone reconstruction." *Science translational medicine* 8.343 (2016): 343ra83-343ra83.

37. Koons, Gerry L., Mani Diba, and Antonios G. Mikos. "Materials design for bone-tissue engineering." *Nature Reviews Materials* 5.8 (2020): 584-603.

38. Norris, Christopher J., et al. "Self‐healing fibre reinforced composites via a bioinspired vasculature." *Advanced Functional Materials* 21.19 (2011): 3624-3633.

39. Bittner, Sean M., et al. "Three-dimensional printing of multilayered tissue engineering scaffolds." *Materials Today* 21.8 (2018): 861-874.

40. Shi, Liyang, et al. "Self‐healing silk fibroin‐based hydrogel for bone regeneration: Dynamic metal‐ligand self‐assembly approach." *Advanced Functional Materials* 27.37 (2017): 1700591.

41. Liu, Hua, et al. "Composite scaffolds of nano-hydroxyapatite and silk fibroin enhance mesenchymal stem cell-based bone regeneration via the interleukin 1 alpha autocrine/paracrine signaling loop." *Biomaterials* 49 (2015): 103-112.

42. Partlow, Benjamin P., et al. "Highly tunable elastomeric silk biomaterials." *Advanced functional materials* 24.29 (2014): 4615-4624.

43. Marelli, Benedetto, et al. "Silk fibroin derived polypeptide-induced biomineralization of collagen." *Biomaterials* 33.1 (2012): 102-108.

44. Wang, Martha O., et al. "Evaluating 3D‐Printed biomaterials as scaffolds for vascularized bone tissue engineering." *Advanced Materials* 27.1 (2015): 138-144.

45. Kasper, F. Kurtis, et al. "Synthesis of poly (propylene fumarate)." *Nature protocols* 4.4 (2009): 518-525.

46. Wilson, James A., et al. "Magnesium catalyzed polymerization of end functionalized poly (propylene maleate) and poly (propylene fumarate) for 3D printing of bioactive scaffolds." *Journal of the American Chemical Society* 140.1 (2018): 277-284.

47. Lanao, Rosa P. Félix, et al. "Bone response to fast-degrading, injectable calcium phosphate cements containing PLGA microparticles." *Biomaterials* 32.34 (2011): 8839-8847.

48. Tatara, Alexander M., et al. "Biomaterials-aided mandibular reconstruction using in vivo bioreactors." *Proceedings of the National Academy of Sciences* 116.14 (2019): 6954-6963.

49. Lin, Dan, et al. "Rapid initiation of guided bone regeneration driven by spatiotemporal delivery of IL-8 and BMP-2 from hierarchical MBG-based scaffold." *Biomaterials* 196 (2019): 122-137.

50. Zdravkov, Borislav, et al. "Pore classification in the characterization of porous materials: A perspective." *Open Chemistry* 5.2 (2007): 385-395.

51. Li, Jinhua, et al. "Valence state manipulation of cerium oxide nanoparticles on a titanium surface for modulating cell fate and bone formation." *Advanced Science* 5.2 (2018): 1700678.

52. Yu, Hai‐Jun, et al. "Ductile biodegradable Mg‐based metallic glasses with excellent biocompatibility." *Advanced Functional Materials* 23.38 (2013): 4793-4800.

53. Shimizu, Masayuki, et al. "Carbon nanotubes induce bone calcification by bidirectional interaction with osteoblasts." *Advanced Materials* 24.16 (2012): 2176-2185.

54. Nardecchia, Stefania, et al. "Osteoconductive Performance of Carbon Nanotube Scaffolds Homogeneously Mineralized by Flow‐Through Electrodeposition." *Advanced Functional Materials* 22.21 (2012): 4411-4420.

55. Hu, Xiaoxia, et al. "A difunctional regeneration scaffold for knee repair based on aptamer‐directed cell recruitment." *Advanced Materials* 29.15 (2017): 1605235.

56. Yazdi, Mohsen Khodadadi, et al. "Hydrogel membranes: A review." *Materials Science and Engineering: C* 114 (2020): 111023.

57. Ruan, Jing, et al. "Enhanced physiochemical and mechanical performance of chitosan‐grafted graphene oxide for superior Osteoinductivity." *Advanced Functional Materials* 26.7 (2016): 1085-1097.

58. Nayak, Tapas R., et al. "Graphene for controlled and accelerated osteogenic differentiation of human mesenchymal stem cells." *ACS nano* 5.6 (2011): 4670-4678.

59. Lee, Wong Cheng, et al. "Origin of enhanced stem cell growth and differentiation on graphene and graphene oxide." *ACS nano* 5.9 (2011): 7334-7341.

60. Li, Keheng, et al. "Biomimetic ultralight, highly porous, shape‐adjustable, and biocompatible 3D graphene minerals via incorporation of self‐assembled peptide nanosheets." *Advanced Functional Materials* 28.29 (2018): 1801056.

61. Ma, Hongshi, et al. "A bifunctional biomaterial with photothermal effect for tumor therapy and bone regeneration." *Advanced Functional Materials* 26.8 (2016): 1197-1208.

62. Arnold, Anne M., et al. "Phosphate graphene as an intrinsically osteoinductive scaffold for stem cell-driven bone regeneration." *Proceedings of the National Academy of Sciences* 116.11 (2019): 4855-4860.

63. Jakus, Adam E., et al. "Hyperelastic “bone”: A highly versatile, growth factor–free, osteoregenerative, scalable, and surgically friendly biomaterial." *Science translational medicine* 8.358 (2016): 358ra127-358ra127.

64. Lei, Miao, et al. "Programmable electrofabrication of porous janus films with tunable janus balance for anisotropic cell guidance and tissue regeneration." *Advanced Functional Materials* 29.18 (2019): 1900065.

65. Diba, Mani, et al. "Composite Colloidal Gels Made of Bisphosphonate‐Functionalized Gelatin and Bioactive Glass Particles for Regeneration of Osteoporotic Bone Defects." *Advanced Functional Materials* 27.45 (2017): 1703438.

66. Du, Yingying, et al. "Selective laser sintering scaffold with hierarchical architecture and gradient composition for osteochondral repair in rabbits." *Biomaterials* 137 (2017): 37-48.

67. Moreau, David, et al. "Hydrogel films and coatings by swelling-induced gelation." *Proceedings of the National Academy of Sciences* 113.47 (2016): 13295-13300.

68. Lai, Yuxiao, et al. "Osteogenic magnesium incorporated into PLGA/TCP porous scaffold by 3D printing for repairing challenging bone defect." *Biomaterials* 197 (2019): 207-219.

69. Yun, Hyung-Mun, et al. "Magnetic nanocomposite scaffolds combined with static magnetic field in the stimulation of osteoblastic differentiation and bone formation." *Biomaterials* 85 (2016): 88-98.

70. Diba, Mani, et al. "Self‐healing biomaterials: from molecular concepts to clinical applications." *Advanced Materials Interfaces* 5.17 (2018): 1800118.

71. Mora-Raimundo, Patricia, et al. "Nanoparticles to knockdown osteoporosis-related gene and promote osteogenic marker expression for osteoporosis treatment." *ACS nano* 13.5 (2019): 5451-5464.

72. Müller, Werner EG, et al. "Transformation of amorphous polyphosphate nanoparticles into coacervate complexes: an approach for the encapsulation of mesenchymal stem cells." *Small* 14.27 (2018): 1801170.

73. Tolba, Emad, et al. "In situ polyphosphate nanoparticle formation in hybrid poly (vinyl alcohol)/karaya gum hydrogels: A porous scaffold inducing infiltration of mesenchymal stem cells." *Advanced Science* 6.2 (2019): 1801452.

74. Zinger, Assaf, et al. "Proteolytic nanoparticles replace a surgical blade by controllably remodeling the oral connective tissue." *ACS nano* 12.2 (2018): 1482-1490.

75. Kang, Min Sil, et al. "Nanocements produced from mesoporous bioactive glass nanoparticles." *Biomaterials* 162 (2018): 183-199.

76. Wang, Yuchen, et al. "Fracture-targeted delivery of β-catenin agonists via peptide-functionalized nanoparticles augments fracture healing." *ACS nano* 11.9 (2017): 9445-9458.

77. Geuli, Ori, et al. "Electrochemically driven hydroxyapatite nanoparticles coating of medical implants." *Advanced Functional Materials* 26.44 (2016): 8003-8010.

78. Zheng, Chuping, et al. "Functional selenium nanoparticles enhanced stem cell osteoblastic differentiation through BMP signaling pathways." *Advanced Functional Materials* 24.43 (2014): 6872-6883.

79. Yu, Xiaohua, et al. "Multilayered inorganic microparticles for tunable dual growth factor delivery." *Advanced functional materials* 24.20 (2014): 3082-3093.

80. Takizawa, Takashi, et al. "Titanium fiber plates for bone tissue repair." *Advanced Materials* 30.4 (2018): 1703608.

81. Sant, Shilpa, et al. "Self‐assembled hydrogel fiber bundles from oppositely charged polyelectrolytes mimic micro‐/nanoscale hierarchy of collagen." *Advanced functional materials* 27.36 (2017): 1606273.

82. Cheng, Gu, et al. "Controlled co-delivery of growth factors through layer-by-layer assembly of core–shell nanofibers for improving bone regeneration." *ACS nano* 13.6 (2019): 6372-6382.

83. Naskar, Deboki, et al. "Dual growth factor loaded nonmulberry silk fibroin/carbon nanofiber composite 3D scaffolds for in vitro and in vivo bone regeneration." *Biomaterials* 136 (2017): 67-85.

84. Newcomb, Christina J., et al. "Supramolecular nanofibers enhance growth factor signaling by increasing lipid raft mobility." *Nano letters* 16.5 (2016): 3042-3050.

85. Cadafalch Gazquez, Gerard, et al. "Flexible yttrium-stabilized zirconia nanofibers offer bioactive cues for osteogenic differentiation of human mesenchymal stromal cells." *Acs Nano* 10.6 (2016): 5789-5799.

86. Xue, Jiajia, et al. "Electrospun microfiber membranes embedded with drug-loaded clay nanotubes for sustained antimicrobial protection." *ACS nano* 9.2 (2015): 1600-1612.

87. Li, Long, et al. "Controlled dual delivery of BMP-2 and dexamethasone by nanoparticle-embedded electrospun nanofibers for the efficient repair of critical-sized rat calvarial defect." *Biomaterials* 37 (2015): 218-229.

88. Jo, Yun Kee, et al. "Diatom‐inspired silica nanostructure coatings with controllable microroughness using an engineered mussel protein glue to accelerate bone growth on titanium‐based implants." *Advanced Materials* 29.46 (2017): 1704906.

89. Cheng, Zhe A., et al. "Nanoscale coatings for ultralow dose BMP‐2‐driven regeneration of critical‐sized bone defects." *Advanced Science* 6.2 (2019): 1800361.

90. Min, Jouha, et al. "Designer dual therapy nanolayered implant coatings eradicate biofilms and accelerate bone tissue repair." *ACS nano* 10.4 (2016): 4441-4450.

91. Machillot, Paul, et al. "Automated Buildup of Biomimetic Films in Cell Culture Microplates for High‐Throughput Screening of Cellular Behaviors." *Advanced Materials* 30.27 (2018): 1801097.

92. Ha, Yuan, et al. "Phase‐Transited Lysozyme as a Universal Route to Bioactive Hydroxyapatite Crystalline Film." *Advanced Functional Materials* 28.4 (2018): 1704476.

93. Feng, Chun, et al. "3D printing of Lotus root‐like biomimetic materials for cell delivery and tissue regeneration." *Advanced Science* 4.12 (2017): 1700401.

94. Pobloth, Anne-Marie, et al. "Mechanobiologically optimized 3D titanium-mesh scaffolds enhance bone regeneration in critical segmental defects in sheep." *Science translational medicine* 10.423 (2018).

95. Cui, Haitao, et al. "Biologically inspired smart release system based on 3D bioprinted perfused scaffold for vascularized tissue regeneration." *Advanced science* 3.8 (2016): 1600058.

96. Luo, Zuyuan, et al. "Injectable 3D Porous Micro‐Scaffolds with a Bio‐Engine for Cell Transplantation and Tissue Regeneration." *Advanced Functional Materials* 28.41 (2018): 1804335.

97. Ying, Guo‐Liang, et al. "Aqueous two‐phase emulsion bioink‐enabled 3D bioprinting of porous hydrogels." *Advanced Materials* 30.50 (2018): 1805460.

98. Neffe, Axel T., et al. "One step creation of multifunctional 3D architectured hydrogels inducing bone regeneration." *Advanced Materials* 27.10 (2015): 1738-1744.

99. Jeon, Oju, Keewon Lee, and Eben Alsberg. "Spatial Micropatterning of Growth Factors in 3D Hydrogels for Location‐Specific Regulation of Cellular Behaviors." *Small* 14.25 (2018): 1800579.

100. Li, Lan, et al. "3D molecularly functionalized cell‐free biomimetic scaffolds for osteochondral regeneration." *Advanced Functional Materials* 29.6 (2019): 1807356.

101. Yan, Yufei, et al. "Vascularized 3D printed scaffolds for promoting bone regeneration." *Biomaterials* 190 (2019): 97-110.

102. Chen, Lei, et al. "3D printing of a lithium-calcium-silicate crystal bioscaffold with dual bioactivities for osteochondral interface reconstruction." *Biomaterials* 196 (2019): 138-150.

103. Yang, Bowen, et al. "2D‐black‐phosphorus‐reinforced 3D‐printed scaffolds: a stepwise countermeasure for osteosarcoma." *Advanced Materials* 30.10 (2018): 1705611.

104. Zhai, Xinyun, et al. "3D‐bioprinted osteoblast‐laden nanocomposite hydrogel constructs with induced microenvironments promote cell viability, differentiation, and osteogenesis both in vitro and in vivo." *Advanced Science* 5.3 (2018): 1700550.

105. Jordahl, Jacob H., et al. "3D jet writing: Functional microtissues based on tessellated scaffold architectures." *Advanced Materials* 30.14 (2018): 1707196.

106. Gao, Fei, et al. "Direct 3D printing of high strength biohybrid gradient hydrogel scaffolds for efficient repair of osteochondral defect." *Advanced Functional Materials* 28.13 (2018): 1706644.

107. Chisca, Stefan, et al. "Artificial 3D hierarchical and isotropic porous polymeric materials." *Science advances* 4.5 (2018): eaat0713.

108. Zhang, Wenjie, et al. "3D-printed scaffolds with synergistic effect of hollow-pipe structure and bioactive ions for vascularized bone regeneration." *Biomaterials* 135 (2017): 85-95.

109. Deng, Cuijun, et al. "Retracted: 3D Printing of Bilineage Constructive Biomaterials for Bone and Cartilage Regeneration." *Advanced Functional Materials* 27.36 (2017): 1703117.

110. Pati, Falguni, et al. "Ornamenting 3D printed scaffolds with cell-laid extracellular matrix for bone tissue regeneration." *Biomaterials* 37 (2015): 230-241.

111. Jiang, Tao, et al. "Electrospinning of polymer nanofibers for tissue regeneration." *Progress in polymer Science* 46 (2015): 1-24.

112. Xie, Mingjun, et al. "Electro‐Assisted Bioprinting of Low‐Concentration GelMA Microdroplets." *Small* 15.4 (2019): 1804216.

113. Brown, Toby D., Paul D. Dalton, and Dietmar W. Hutmacher. "Direct writing by way of melt electrospinning." *Advanced Materials* 23.47 (2011): 5651-5657.

114. Workman, Victoria L., et al. "Controlled generation of microspheres incorporating extracellular matrix fibrils for three‐dimensional cell culture." *Advanced functional materials* 24.18 (2014): 2648-2657.

115. de Jonge, Lise T., et al. "Electrosprayed enzyme coatings as bioinspired alternatives to bioceramic coatings for orthopedic and oral implants." *Advanced functional materials* 19.5 (2009): 755-762.

116. Hoffman, Allan S. "Hydrogels for biomedical applications." Advanced drug delivery reviews 64 (2012): 18-23.

117. Ahmed, Enas M. "Hydrogel: Preparation, characterization, and applications: A review." Journal of advanced research 6.2 (2015): 105-121.

118. Chung, Hyun Jung, and Tae Gwan Park. "Self-assembled and nanostructured hydrogels for drug delivery and tissue engineering." Nano Today 4.5 (2009): 429-437.

119. Slaughter, Brandon V., et al. "Hydrogels in regenerative medicine." Advanced materials 21.32-33 (2009): 3307-3329.

120. Zhu, Junmin, and Roger E. Marchant. "Design properties of hydrogel tissue-engineering scaffolds." Expert review of medical devices 8.5 (2011): 607-626.

121. Drury, Jeanie L., and David J. Mooney. "Hydrogels for tissue engineering: scaffold design variables and applications." Biomaterials 24.24 (2003): 4337-4351.

122. Nagam, SANTHI PRIYA, et al. "A comprehensive review on hydrogels." Int. J. Curr. Pharm. Res 8.1 (2016).

123. Saxena, Amulya K. "Synthetic biodegradable hydrogel (PleuraSeal) sealant for sealing of lung tissue after thoracoscopic resection." The Journal of thoracic and cardiovascular surgery 139.2 (2010): 496-497.

124. Hamidi, Mehrdad, Amir Azadi, and Pedram Rafiei. "Hydrogel nanoparticles in drug delivery." Advanced drug delivery reviews 60.15 (2008): 1638-1649.

125. Zohuriaan-Mehr, M. J., et al. "Advances in non-hygienic applications of superabsorbent hydrogel materials." Journal of materials science 45.21 (2010): 5711-5735.

126. Chen, X., et al. "Enzymatic and chemoenzymatic approaches to synthesis of sugar-based polymer and hydrogels." Carbohydrate polymers 28.1 (1995): 15-21.

127. Kashyap, N. K. M. R. K. N., N. Kumar, and MNV Ravi Kumar. "Hydrogels for pharmaceutical and biomedical applications." Critical Reviews™ in Therapeutic Drug Carrier Systems 22.2 (2005).

128. Kaihara, Sachiko, Shuichi Matsumura, and John P. Fisher. "Synthesis and characterization of cyclic acetal based degradable hydrogels." European journal of pharmaceutics and biopharmaceutics 68.1 (2008): 67-73.

129. Stamatialis, Dimitrios F., et al. "Medical applications of membranes: drug delivery, artificial organs and tissue engineering." Journal of Membrane Science 308.1-2 (2008): 1-34.

130. Zhang, Ling, et al. "Preparation of collagen–chondroitin sulfate–hyaluronic acid hybrid hydrogel scaffolds and cell compatibility in vitro." Carbohydrate polymers 84.1 (2011): 118-125.

131. Lin, Chien-Chi, and Kristi S. Anseth. "PEG hydrogels for the controlled release of biomolecules in regenerative medicine." Pharmaceutical research 26.3 (2009): 631-643.

132. Plunkett, Kyle N., and Jeffrey S. Moore. "Patterned dual pH-responsive core− shell hydrogels with controllable swelling kinetics and volumes." Langmuir 20.16 (2004): 6535-6537.

133. Sikareepaisan, Panprung, Uracha Ruktanonchai, and Pitt Supaphol. "Preparation and characterization of asiaticoside-loaded alginate films and their potential for use as effectual wound dressings." Carbohydrate Polymers 83.4 (2011): 1457-1469.

134. Wang, Feng, et al. "Injectable, rapid gelling and highly flexible hydrogel composites as growth factor and cell carriers." Acta biomaterialia 6.6 (2010): 1978-1991.

135. Roy, Debashish, Jennifer N. Cambre, and Brent S. Sumerlin. "Future perspectives and recent advances in stimuli-responsive materials." Progress in Polymer Science 35.1-2 (2010): 278-301.

136. Oshida, Y., and Y. Guven. "Biocompatible coatings for metallic biomaterials." *Surface Coating and Modification of Metallic Biomaterials*. Woodhead Publishing, 2015. 287-343.

137. Sergi, Rachele, Devis Bellucci, and Valeria Cannillo. "A comprehensive review of bioactive glass coatings: State of the art, challenges and future perspectives." *Coatings* 10.8 (2020): 757.

138. Kazimierczak, Paulina, and Agata Przekora. "Osteoconductive and osteoinductive surface modifications of biomaterials for bone regeneration: A concise review." *Coatings* 10.10 (2020): 971.

139. Nouri, A., and Cuie Wen. "Introduction to surface coating and modification for metallic biomaterials." *Surface Coating and Modification of Metallic Biomaterials* (2015): 3-60.

140. Surmenev, Roman A., Maria A. Surmeneva, and Anna A. Ivanova. "Significance of calcium phosphate coatings for the enhancement of new bone osteogenesis–a review." *Acta biomaterialia* 10.2 (2014): 557-579.

141. Dehghanghadikolaei, Amir, and Behzad Fotovvati. "Coating techniques for functional enhancement of metal implants for bone replacement: a review." *Materials* 12.11 (2019): 1795.

142. Mumith, Aadil, et al. "The effect of strontium and silicon substituted hydroxyapatite electrochemical coatings on bone ingrowth and osseointegration of selective laser sintered porous metal implants." *PloS one* 15.1 (2020): e0227232.

143. Mokabber, T., et al. "Antimicrobial electrodeposited silver-containing calcium phosphate coatings." *ACS applied materials & interfaces* 12.5 (2020): 5531-5541.

144. Huang, Zhenfei, et al. "A Magnetic Iron Oxide/Polydopamine Coating Can Improve Osteogenesis of 3D‐Printed Porous Titanium Scaffolds with a Static Magnetic Field by Upregulating the TGFβ‐Smads Pathway." *Advanced healthcare materials* 9.14 (2020): 2000318.

145. Fan, Bo, et al. "Electroactive barium titanate coated titanium scaffold improves osteogenesis and osseointegration with low-intensity pulsed ultrasound for large segmental bone defects." *Bioactive Materials* 5.4 (2020): 1087-1101.

146. Zhang, Yan, et al. "Aligned porous barium titanate/hydroxyapatite composites with high piezoelectric coefficients for bone tissue engineering." *Materials Science and Engineering: C* 39 (2014): 143-149.

147. Ehterami, Arian, et al. "Fabrication and characterization of highly porous barium titanate based scaffold coated by Gel/HA nanocomposite with high piezoelectric coefficient for bone tissue engineering applications." *Journal of the mechanical behavior of biomedical materials* 79 (2018): 195-202.

148. Scarisoreanu, N. D., et al. "Lead-free piezoelectric (Ba, Ca)(Zr, Ti) O3 thin films for biocompatible and flexible devices." *ACS applied materials & interfaces* 9.1 (2017): 266-278.

149. Zlotnik, Sebastian, et al. "Functionalized-ferroelectric-coating-driven enhanced biomineralization and protein-conformation on metallic implants." *Journal of Materials Chemistry B* 7.13 (2019): 2177-2189.

150. Przekora, Agata. "Current trends in fabrication of biomaterials for bone and cartilage regeneration: Materials modifications and biophysical stimulations." *International journal of molecular sciences* 20.2 (2019): 435.

151. Bacakova, Lucie, et al. "Applications of zeolites in biotechnology and medicine–a review." *Biomaterials science* 6.5 (2018): 974-989.

152. Chen, Junyu, et al. "Osteogenic activity and antibacterial effect of porous titanium modified with metal‐organic framework films." *Journal of Biomedical Materials Research Part A* 105.3 (2017): 834-846.

153. Zhang, Xinran, et al. "Amorphous carbon modification on implant surface: a general strategy to enhance osteogenic differentiation for diverse biomaterials via FAK/ERK1/2 signaling pathways." *Journal of Materials Chemistry B* 7.15 (2019): 2518-2533.

154. Rifai, Aaqil, et al. "Polycrystalline diamond coating of additively manufactured titanium for biomedical applications." *ACS applied materials & interfaces* 10.10 (2018): 8474-8484.

155. Tien, Han-Wen, et al. "Long term in vivo functional stability and encapsulation reliability of using ultra-nanocrystalline diamond as an insulating coating layer for implantable microchips." *Journal of Materials Chemistry B* 5.20 (2017): 3706-3717.

156. Patel, Kapil D., et al. "Coating biopolymer nanofibers with carbon nanotubes accelerates tissue healing and bone regeneration through orchestrated cell-and tissue-regulatory responses." *Acta biomaterialia* 108 (2020): 97-110.

157. Li, Xia, et al. "Boron nitride nanotube‐enhanced osteogenic differentiation of mesenchymal stem cells." *Journal of Biomedical Materials Research Part B: Applied Biomaterials* 104.2 (2016): 323-329.

158. Bougas, Kostas, et al. "Laminin coating promotes calcium phosphate precipitation on titanium discs in vitro." *Journal of oral & maxillofacial research* 2.4 (2011).

159. Bougas, Kostas, et al. "Novel implant coating agent promotes gene expression of osteogenic markers in rats during early osseointegration." *International journal of biomaterials* 2012 (2012).

160. Rabe, Rebecca, et al. "Dairy-inspired coatings for bone implants from whey protein isolate-derived self-assembled fibrils." *International journal of molecular sciences* 21.15 (2020): 5544.

161. Zhao, Mingyan, Reema Anouz, and Thomas Groth. "Effect of microenvironment on adhesion and differentiation of murine C3H10T1/2 cells cultured on multilayers containing collagen I and glycosaminoglycans." *Journal of Tissue Engineering* 11 (2020): 2041731420940560.

162. Liu, Congcong, et al. "Enhanced osteoinductivity and corrosion resistance of dopamine/gelatin/rhBMP-2–coated β-TCP/Mg-Zn orthopedic implants: An in vitro and in vivo study." *Plos one* 15.1 (2020): e0228247.

163. Abdal-hay, Abdalla, Montasser Dewidar, and Jae Kyoo Lim. "Biocorrosion behavior and cell viability of adhesive polymer coated magnesium based alloys for medical implants." *Applied Surface Science* 261 (2012): 536-546.

164. Diekjürgen, Dorina, and David W. Grainger. "Polysaccharide matrices used in 3D in vitro cell culture systems." *Biomaterials* 141 (2017): 96-115.

165. Yu, Le, et al. "Effect of three‐dimensional porosity gradients of biomimetic coatings on their bonding strength and cell behavior." *Journal of Biomedical Materials Research Part A* 109.5 (2021): 615-626.

166. Bose, Susmita, Mangal Roy, and Amit Bandyopadhyay. "Recent advances in bone tissue engineering scaffolds." *Trends in biotechnology* 30.10 (2012): 546-554.

167. Rouwkema, Jeroen, Nicolas C. Rivron, and Clemens A. van Blitterswijk. "Vascularization in tissue engineering." *Trends in biotechnology* 26.8 (2008): 434-441.

168. Murphy, Ciara M., Matthew G. Haugh, and Fergal J. O'brien. "The effect of mean pore size on cell attachment, proliferation and migration in collagen–glycosaminoglycan scaffolds for bone tissue engineering." *Biomaterials* 31.3 (2010): 461-466.

169. Woodard, Joseph R., et al. "The mechanical properties and osteoconductivity of hydroxyapatite bone scaffolds with multi-scale porosity." *Biomaterials* 28.1 (2007): 45-54.

170. Olszta, Matthew J., et al. "Bone structure and formation: A new perspective." *Materials Science and Engineering: R: Reports* 58.3-5 (2007): 77-116.

171. Williams, David F. "On the mechanisms of biocompatibility." *Biomaterials* 29.20 (2008): 2941-2953.

172. Hofmann, Ulrich, Kurd Endell, and Diederich Wilm. "Röntgenographische und kolloidchemische Untersuchungen über Ton." *Angewandte Chemie* 47.30 (1934): 539-547.

173. Churchman, G. J., and R. M. Carr. "Stability fields of hydration states of an halloysite." *American Mineralogist: Journal of Earth and Planetary Materials* 57.5-6 (1972): 914-923.

174. Churchman, G. J., and R. M. Carr. "The definition and nomenclature of halloysites." *Clays and Clay Minerals* 23.5 (1975): 382-388.

175. Alexander, L. T., et al. "Relationship of the clay minerals halloysite and endellite." *American Mineralogist: Journal of Earth and Planetary Materials* 28.1 (1943): 1-18.

176. Rawtani, Deepak, and Y. K. Agrawal. "Multifarious applications of halloysite nanotubes: a review." *Rev. Adv. Mater. Sci* 30.3 (2012): 282-295.

177. Hong, H-L., and J-X. Mi. "Characteristics of halloysite associated with rectorite from Hubei, China." *Mineralogical Magazine* 70.3 (2006): 257-264.

178. Perruchot, A., et al. "L'halloysite karstique: comparaison des gisements types de Wallonie (Belgique) et du Périgord (France)." *Clay Minerals* 32.2 (1997): 271-287.

179. Theo Kloprogge, J., and Ray L. Frost. "Raman microprobe spectroscopy of hydrated halloysite from a Neogene cryptokarst from Southern Belgium." *Journal of Raman spectroscopy* 30.12 (1999): 1079-1085.

180. Churchman, G. Jock, and Benny KG Theng. "Clay research in Australia and New Zealand." (2002): 153-156.

181. Du, Mingliang, Baochun Guo, and Demin Jia. "Newly emerging applications of halloysite nanotubes: a review." *Polymer International* 59.5 (2010): 574-582.

182. Lvov, Yuri M., et al. "Halloysite clay nanotubes for controlled release of protective agents." *ACS nano* 2.5 (2008): 814-820.

183. Tharmavaram, Maithri, Gaurav Pandey, and Deepak Rawtani. "Surface modified halloysite nanotubes: a flexible interface for biological, environmental and catalytic applications." *Advances in colloid and interface science* 261 (2018): 82-101.

184. http://phantomplastics.com/functional-fillers/halloysite/

185. Kunze, G. W., and W. F. Bradley. "Occurrence of a tabular halloysite in a Texas soil." *Clays and Clay Minerals* 12.1 (1963): 523-527.

186. Mousavi, Seyyed Mojtaba, et al. *Development of clay nanoparticles toward bio and medical applications*. IntechOpen, 2018.

187. Dixon, J. B., and T. R. McKee. "Internal and external morphology of tubular and spheroidal halloysite particles." *Clays and Clay Minerals* 22.1 (1974): 127-137.

188. Wada, Shin-Ichiro, and Chitoshi Mizota. "Iron-rich halloysite (10A) with crumpled lamellar morphology from Hokkaido, Japan." *Clays & Clay Minerals* 30.4 (1982): 315-317.

189. Churchman, G. J., and B. K. G. Theng. "Interactions of halloysites with amides: mineralogical factors affecting complex formation." *Clay Minerals* 19.2 (1984): 161-175.

190. Noro, H. "Hexagonal platy halloysite in an altered tuff bed, Komaki city, Aichi prefecture, Central Japan." *Clay Minerals* 21.3 (1986): 401-415.

191. Singer, Arieh, et al. "Halloysite characteristics and formation in the northern Golan Heights." *Geoderma* 123.3-4 (2004): 279-295.

192. Sudo, Toshio. "Particle shape of a certain clay of hydrated halloysite, as revealed by the electron microscope." *Mineralogical Journal* 1.1 (1953): 66-68_1.

193. Birrell, Kenneth Stewart, Morice Fieldes, and K. I. Williamson. "Unusual forms of halloysite." (1955): 122-124.

194. Parham, Walter E. "Formation of halloysite from feldspar: low temperature, artificial weathering versus natural weathering." *Clays and Clay Minerals* 17.1 (1969): 13-22.

195. Askenasy, P. E., J. B. Dixon, and T. R. McKee. "Spheroidal halloysite in a Guatemalan soil." *Soil Science Society of America Journal* 37.5 (1973): 799-803.

196. Yotsumoto, H. *Electron micrographs of clay minerals*. Elsevier, 2011.

197. auSadao Shoji, Masahiko Saigusa, and Tatsuto Kato. "Origin and nature of halloysite in Ando soils from Towada tephra, Japan." *Geoderma* 20.2 (1978): 115-129.

198. Tazaki, Kazue. "Micromorphology of halloysite produced by weathering of plagioclase in volcanic ash." *Developments in Sedimentology*. Vol. 27. Elsevier, 1979. 415-422.

199. Tomura, Shinji, et al. "Spherical kaolinite: synthesis and mineralogical properties." *Clays and Clay Minerals* 31.6 (1983): 413-421.

200. Ward, C., and F. Ivor Roberts. "Occurrence of spherical halloysite in bituminous coals of the Sydney Basin, Australia." *Clays and Clay Minerals* 38.5 (1990): 501-506.

201. Bates, Thomas F., Fred A. Hildebrand, and Ada Swineford. "Morphology and structure of endellite and halloysite." *American Mineralogist: Journal of Earth and Planetary Materials* 35.7-8 (1950): 463-484.

202. Honjo, Goro, Norihisa Kitamura, and Kazuhiro Mihama. "A study of clay minerals by means of single-crystal electron diffraction diagrams—the structure of tubular kaolin." *Clay Minerals Bulletin* 2.12 (1954): 133-141.

203. Kohyama, Norihiko, Kurio Fukushima, and Akira Fukami. "Observation of the hydrated form of tubular halloysite by an electron microscope equipped with an environmental cell." *Clays and Clay Minerals* 26.1 (1978): 25-40.

204. Nagasawa, Keinosuke, and Harufumi Noro. "Mineralogical properties of halloysites of weathering origin." *Chemical Geology* 60.1-4 (1987): 145-149.

205. Robertson, Ian DM, and R. Eggleton. "Weathering of granitic muscovite to kaolinite and halloysite and of plagioclase-derived kaolinite to halloysite." *Clays and clay minerals* 39.2 (1991): 113-126.

206. Churchman, G. J., et al. "Characteristics of fine pores in some halloysites." *Clay Minerals* 30.2 (1995): 89-98.

207. Adamo, P., P. Violante, and M. J. Wilson. "Tubular and spheroidal halloysite in pyroclastic deposits in the area of the Roccamonfina volcano (Southern Italy)." *Geoderma* 99.3-4 (2001): 295-316.

208. Karnik, Sonali, Kanesha Hines, and David K. Mills. "Nanoenhanced hydrogel system with sustained release capabilities." *Journal of Biomedical Materials Research Part A* 103.7 (2015): 2416-2426.

209. Patel, Shraddha, et al. "Sustained release of antibacterial agents from doped halloysite nanotubes." *Bioengineering* 3.1 (2016): 1.

210. Vergaro, Viviana, et al. "Cytocompatibility and uptake of halloysite clay nanotubes." *Biomacromolecules* 11.3 (2010): 820-826.

211. Fakhrullina, Gölnur I., et al. "Toxicity of halloysite clay nanotubes in vivo: a Caenorhabditis elegans study." *Environmental Science: Nano* 2.1 (2015): 54-59.

212. Kryuchkova, Marina, et al. "Evaluation of toxicity of nanoclays and graphene oxide in vivo: a Paramecium caudatum study." *Environmental Science: Nano* 3.2 (2016): 442-452.

213. Tohidi, Sh, A. Ghaee, and J. Barzin. "Preparation and characterization of poly (lactic‐co‐glycolic acid)/chitosan electrospun membrane containing amoxicillin‐loaded halloysite nanoclay." *Polymers for Advanced Technologies* 27.8 (2016): 1020-1028.

214. Tan, Daoyong, et al. "Natural halloysite nanotubes as mesoporous carriers for the loading of ibuprofen." *Microporous and Mesoporous Materials* 179 (2013): 89-98.

215. Li, Hui, et al. "Functionalization of halloysite nanotubes by enlargement and hydrophobicity for sustained release of analgesic." *Colloids and Surfaces A: Physicochemical and Engineering Aspects* 487 (2015): 154-161.

216. Ganguly, Sayan, et al. "Synthesis of polydopamine-coated halloysite nanotube-based hydrogel for controlled release of a calcium channel blocker." *RSC advances* 6.107 (2016): 105350-105362.

217. Shi, Yin-Feng, et al. "Functionalized halloysite nanotube-based carrier for intracellular delivery of antisense oligonucleotides." *Nanoscale research letters* 6.1 (2011): 1-7.

218. Santos, Ana C., et al. "Halloysite clay nanotubes for life sciences applications: From drug encapsulation to bioscaffold." *Advances in colloid and interface science* 257 (2018): 58-70.

219. Wei, Wenbo, et al. "Clay nanotube/poly (methyl methacrylate) bone cement composites with sustained antibiotic release." *Macromolecular materials and engineering* 297.7 (2012): 645-653.

220. Bottino, Marco C., et al. "Nanotube-modified dentin adhesive—Physicochemical and dentin bonding characterizations." *Dental Materials* 29.11 (2013): 1158-1165.

221. Tian, Ming, et al. "Fabrication and evaluation of Bis-GMA/TEGDMA dental resins/composites containing nano fibrillar silicate." *Dental materials* 24.2 (2008): 235-243.

222. Feitosa, Sabrina A., et al. "Synthesis and characterization of novel halloysite-incorporated adhesive resins." *Journal of dentistry* 43.11 (2015): 1316-1322.

223. Barot, Tejas, Deepak Rawtani, and Pratik Kulkarni. "Development of chlorhexidine loaded halloysite nanotube based experimental resin composite with enhanced physico-mechanical and biological properties for dental applications." *Journal of Composites Science* 4.2 (2020): 81.

224. Drury, Jeanie L., and David J. Mooney. "Hydrogels for tissue engineering: scaffold design variables and applications." *Biomaterials* 24.24 (2003): 4337-4351.

225. Liu, Mingxian, et al. "In vitro evaluation of alginate/halloysite nanotube composite scaffolds for tissue engineering." *Materials Science and Engineering: C* 49 (2015): 700-712.

226. Liu, Mingxian, et al. "Chitosan–halloysite nanotubes nanocomposite scaffolds for tissue engineering." *Journal of Materials Chemistry B* 1.15 (2013): 2078-2089.

227. Nielsen, S. Pors. "The biological role of strontium." *Bone* 35.3 (2004): 583-588.

228. https://m.chemicalbook.com/ProductChemicalPropertiesCB2350213.htm

229. Cabrera, Walter E., et al. "Strontium and bone." *Journal of Bone and Mineral Research* 14.5 (1999): 661-668.

230. Kołodziejska, Barbara, Natalia Stępień, and Joanna Kolmas. "The Influence of Strontium on Bone Tissue Metabolism and Its Application in Osteoporosis Treatment." *International Journal of Molecular Sciences* 22.12 (2021): 6564.

231. Florencio-Silva, Rinaldo, et al. "Biology of bone tissue: structure, function, and factors that influence bone cells." *BioMed research international* 2015 (2015).

232. Caverzasio, Joseph. "Strontium ranelate promotes osteoblastic cell replication through at least two different mechanisms." *Bone* 42.6 (2008): 1131-1136.

233. Martín-del-Campo, Marcela, et al. "Bone regeneration induced by strontium folate loaded biohybrid scaffolds." *Molecules* 24.9 (2019): 1660.

234. Ammann, Patrick, et al. "Strontium ranelate improves bone resistance by increasing bone mass and improving architecture in intact female rats." *Journal of bone and mineral research* 19.12 (2004): 2012-2020.

235. Blaschko, Sarah D., et al. "Strontium substitution for calcium in lithogenesis." *The Journal of urology* 189.2 (2013): 735-739.

236. Shahnazari, M., et al. "Strontium administration in young chickens improves bone volume and architecture but does not enhance bone structural and material strength." *Calcified tissue international* 80.3 (2007): 160-166.

237. Dawson, Earl B., et al. "Relationship of metal metabolism to vascular disease mortality rates in Texas." *The American journal of clinical nutrition* 31.7 (1978): 1188-1197.

238. Zhang, Songou, et al. "Recent developments in strontium-based biocomposites for bone regeneration." *Journal of Artificial Organs* (2020): 1-12.

239. Wang, Guifang, et al. "Effects of Sr-HT-Gahnite on osteogenesis and angiogenesis by adipose derived stem cells for critical-sized calvarial defect repair." *Scientific reports* 7.1 (2017): 1-11.

240. Shie, Ming-You, Shinn-Jyh Ding, and Hsien-Chang Chang. "The role of silicon in osteoblast-like cell proliferation and apoptosis." *Acta biomaterialia* 7.6 (2011): 2604-2614.

241. Xu, Zhengjiang, et al. "Strong mineralization ability of strontium zinc silicate: Formation of a continuous biomorphic mineralized layer with enhanced osteogenic activity." *Colloids and Surfaces B: Biointerfaces* 176 (2019): 420-430.

242. Ehret, Camille, et al. "Strontium-doped hydroxyapatite polysaccharide materials effect on ectopic bone formation." *PLoS One* 12.9 (2017): e0184663.

243. Dziadek, Michal, Ewa Stodolak-Zych, and Katarzyna Cholewa-Kowalska. "Biodegradable ceramic-polymer composites for biomedical applications: A review." *Materials Science and Engineering: C* 71 (2017): 1175-1191.

244. Chen, Yahong, et al. "Developing a strontium-releasing graphene oxide-/collagen-based organic–inorganic nanobiocomposite for large bone defect regeneration via MAPK signaling pathway." *ACS applied materials & interfaces* 11.17 (2019): 15986-15997.

245. Cheng, Delin, et al. "Strontium incorporation improves the bone-forming ability of scaffolds derived from porcine bone." *Colloids and Surfaces B: Biointerfaces* 162 (2018): 279-287.

246. Boraei, Seyyed Behnam Abdollahi, et al. "Effect of SrR delivery in the biomarkers of bone regeneration during the in vitro degradation of HNT/GN coatings prepared by EPD." *Colloids and Surfaces B: Biointerfaces* 190 (2020): 110944.

247. Abdollahi Boraei, Seyyed Behnam, et al. "Enhanced osteogenesis of gelatin-halloysite nanocomposite scaffold mediated by loading strontium ranelate." *International Journal of Polymeric Materials and Polymeric Biomaterials* 70.6 (2021): 392-402.

248. Fernández Tresguerres, Isabel, et al. "Physiological bases of bone regeneration I: Histology and physiology of bone tissue." (2006).

249. Einhorn, Thomas A. "The cell and molecular biology of fracture healing." *Clinical Orthopaedics and Related Research*® 355 (1998): S7-S21.

250. Chen, Fa-Ming, et al. "Homing of endogenous stem/progenitor cells for in situ tissue regeneration: promises, strategies, and translational perspectives." *Biomaterials* 32.12 (2011): 3189-3209.

251. Hughes, Francis J., Jane E. Aubin, and Johan NM Heersche. "Differential chemotactic responses of different populations of fetal rat calvaria cells to platelet-derived growth factor and transforming growth factor β." *Bone and mineral* 19.1 (1992): 63-74.

252. Lind, M. A. R. T. I. N., et al. "Chemotaxis of human osteoblasts: Effects of osteotropic growth factors." *Apmis* 103.1-6 (1995): 140-146.

253. Mehrotra, Meenal, et al. "Differential regulation of platelet-derived growth factor stimulated migration and proliferation in osteoblastic cells." *Journal of cellular biochemistry* 93.4 (2004): 741-752.

254. Tang, Yi, et al. "TGF-β1–induced migration of bone mesenchymal stem cells couples bone resorption with formation." *Nature medicine* 15.7 (2009): 757-765.

255. Lind, Martin, E. F. Eriksen, and C. Bünger. "Bone morphogenetic protein-2 but not bone morphogenetic protein-4 and-6 stimulates chemotactic migration of human osteoblasts, human marrow osteoblasts, and U2-OS cells." *Bone* 18.1 (1996): 53-57.

256. Lieberman, Jay R., Aaron Daluiski, and Thomas A. Einhorn. "The role of growth factors in the repair of bone: biology and clinical applications." *JBJS* 84.6 (2002): 1032-1044.

257. Sims, Natalie A., and Jonathan H. Gooi. "Bone remodeling: Multiple cellular interactions required for coupling of bone formation and resorption." *Seminars in cell & developmental biology*. Vol. 19. No. 5. Academic Press, 2008.

258. Ou, Qianmin, et al. "Nanosilver-incorporated halloysite nanotubes/gelatin methacrylate hybrid hydrogel with osteoimmunomodulatory and antibacterial activity for bone regeneration." *Chemical Engineering Journal* 382 (2020): 123019.

259. Lin, Hang, et al. "Efficient in vivo bone formation by BMP-2 engineered human mesenchymal stem cells encapsulated in a projection stereolithographically fabricated hydrogel scaffold." *Stem cell research & therapy* 10.1 (2019): 1-13.

260. Kim, Sungjun, Sangmin Lee, and Kyobum Kim. "Bone tissue engineering strategies in co-delivery of bone morphogenetic protein-2 and biochemical signaling factors." *Cutting-Edge Enabling Technologies for Regenerative Medicine* (2018): 233-244.

261. Santos, Antônio Aparecido dos, et al. "The role of bone morphogenetic protein on bone tissue repair." *Acta Ortopédica Brasileira* 13 (2005): 194-195.

262. Chen, Fa-Ming, et al. "Homing of endogenous stem/progenitor cells for in situ tissue regeneration: promises, strategies, and translational perspectives." *Biomaterials* 32.12 (2011): 3189-3209.

263. Hughes, Francis J., Jane E. Aubin, and Johan NM Heersche. "Differential chemotactic responses of different populations of fetal rat calvaria cells to platelet-derived growth factor and transforming growth factor β." *Bone and mineral* 19.1 (1992): 63-74.

264. Fu, Rongwei, et al. "Effectiveness and harms of recombinant human bone morphogenetic protein-2 in spine fusion: a systematic review and meta-analysis." *Annals of internal medicine* 158.12 (2013): 890-902.

265. Simmonds, Mark C., et al. "Safety and effectiveness of recombinant human bone morphogenetic protein-2 for spinal fusion: a meta-analysis of individual-participant data." *Annals of internal medicine* 158.12 (2013): 877-889.

266. Vukicevic, Slobodan, et al. "The clinical use of bone morphogenetic proteins revisited: a novel biocompatible carrier device OSTEOGROW for bone healing." *International orthopaedics* 38.3 (2014): 635-647.

267. Kajave, Nilabh S., et al. "Bioglass incorporated methacrylated collagen bioactive ink for 3D printing of bone tissue." *Biomedical Materials* 16.3 (2021): 035003.

268. Kim, Won Jin, Hui-Suk Yun, and Geun Hyung Kim. "An innovative cell-laden α-TCP/collagen scaffold fabricated using a two-step printing process for potential application in regenerating hard tissues." *Scientific reports* 7.1 (2017): 1-12.

269. Kajave, Nilabh S., et al. "Dual crosslinking strategy to generate mechanically viable cell-laden printable constructs using methacrylated collagen bioinks." *Materials Science and Engineering: C* 107 (2020): 110290.

270. Shin, Su Ryon, et al. "Carbon nanotube reinforced hybrid microgels as scaffold materials for cell encapsulation." *ACS nano* 6.1 (2012): 362-372.

271. Huang, Liping, et al. "Biomimetic gelatin methacrylate/nano fish bone hybrid hydrogel for bone regeneration via osteoimmunomodulation." *ACS Biomaterials Science & Engineering* 6.6 (2020): 3270-3274.

272. Ou, Qianmin, et al. "Nanosilver-incorporated halloysite nanotubes/gelatin methacrylate hybrid hydrogel with osteoimmunomodulatory and antibacterial activity for bone regeneration." *Chemical Engineering Journal* 382 (2020): 123019.

273. Zhang, J. C., et al. "The repair of critical-size defects with porous hydroxyapatite/polyamide nanocomposite: an experimental study in rabbit mandibles." *International journal of oral and maxillofacial surgery* 39.5 (2010): 469-477.

274. Guo, Jun, et al. "Restoration of critical-size defects in the rabbit mandible using porous nanohydroxyapatite-polyamide scaffolds." *Tissue Engineering Part A* 18.11-12 (2012): 1239-1252.

275. Su, Jiansheng, et al. "Dual delivery of BMP-2 and bFGF from a new nano-composite scaffold, loaded with vascular stents for large-size mandibular defect regeneration." *International journal of molecular sciences* 14.6 (2013): 12714-12728.